

Microfluidic Investigations of CO₂ Mass Transport at Elevated Pressure and Salt Precipitation

by

Tsai Hsing Ho

A thesis submitted in partial fulfillment of the requirements for the degree of

Doctor of Philosophy

Department of Mechanical Engineering

University of Alberta

© Tsai Hsing Ho, 2021

Abstract

Carbon capture and sequestration (CCS) in geological reservoirs is one of the mitigation strategies to slow down the increasing atmospheric CO₂ concentration due to human activities. Effectively characterizing the transport phenomena between CO₂ and materials in reservoirs, including mass/heat transfer and phase change, is crucial but challenging for accurately evaluating potential storage sites and monitoring the injection operation. This doctoral study conducts microfluidic experiments to elucidate the transport behaviors of CO₂ and water at the injection pressure from 0.1 up to 9.5 MPa and the temperature between 22 and 35 °C, corresponding to a deep injection depth. To this end, we develop a high-pressure microfluidic platform and operating procedures for high-pressure experiments. Three primary projects are carried out addressing the important issues of carbon storage engineering.

Firstly (**Chapter 3**), we quantify the volumetric mass transfer coefficient (k_La) of CO₂ at three different states (i.e., gas, liquid, and supercritical phase) to elucidate the pressure effect on the mass transfer process, by measuring the size change of CO₂ micro-bubbles/droplets generated using a microfluidic T-junction. The results show a significantly enhanced mass transfer of supercritical CO₂ in water, while the injection pressure has a minor influence on the k_La measured from gas and liquid CO₂. k_La shows a positive correlation with the continuous phase's Reynolds number, implying the importance of bubble/droplet speed on transporting CO₂.

Secondly (**Chapter 4**), we observe an intriguing multi-phase CO₂ flow and emulsions when operating at the pressure-temperature (P - T) condition close to the CO₂ gas-liquid

phase boundary. We propose a series of strategies to unravel this complex multi-phase dynamics and quantify the CO₂ mass transfer while changing its phase state. The resulting $k_L a$ decreases exponentially with time, which may be influenced by the shrinking specific area (a), CO₂ concentration gradient in the water slug, and the slowing down CO₂'s traveling speed.

Thirdly (**Chapter 5**), we investigate the effects of pore-structures and brine concentrations on salt precipitation, which is a potential threat to hinder CCS in deep saline aquifers, using 2-D planar porous microfluidics. Three distinct stages are observed: (I) initial, (II) rapid growth, and (III) final phases, in the progression of salt nucleation with different rates and size distributions upon brine drying. The location of large brine pools plays an essential role in determining the distribution and size of nucleating salt. The positive correlation between the brine-drying and salt-precipitation speeds may help evaluate salt's precipitation speed for different porosities.

Finally (**Chapter 6**), research outlook and future projects are given, particularly regarding microfluidic applications and studies of carbon capture and sequestration technology in saline aquifers at elevated pressure conditions.

Preface

The majority of this thesis is the original work completed by Tsai-Hsing Ho under Professor Peichun Amy Tsai's inspiration and supervision, including the literature review in **Chapter 1**, the methodology in **Chapter 2**, experiments and data analysis for **Chapter 3** to **Chapter 5**. Junyi Yang helps the image process and analyzes the data performed in **Chapter 3**. The idea and the analysis method presented in **Chapter 4** are inspired and co-supervised by Professor Dan Sameoto and Professor Peichun Amy Tsai.

Chapter 3 is based on the manuscript recently submitted to Lab on a chip: Tsai-Hsing Martin Ho, Junyi Yang, and Peichun Amy Tsai, "Microfluidic Mass Transfer of CO₂ at Different Phases", under revision, 2021.

Chapter 4 includes the manuscript recently submitted to Physics of Fluids: Tsai-Hsing Martin Ho, Dan Sameoto, and Peichun Amy Tsai, "Multiphase CO₂ Emulsions in Microfluidics: Formation, Phases, and Mass Transfer", 2021.

Chapter 5 is based on the journal paper by Tsai-Hsing Martin Ho and Peichun Amy Tsai, "Microfluidic Salt Precipitation: Implications for Geological CO₂ Storage." Lab on a Chip. 2020; 20(20): 3806-14.

Acknowledgements

During the 4+ years of my Ph.D. study, many people directly or indirectly helped and supported me through this challenging and life-changing journey.

First of all, I would like to express my highest respect and gratitude to my advisor Peichun Amy Tsai. Thank you for accepting and sponsoring me as a member of your lab to start my doctoral study. Under your supervision and inspiration, I have improved my critical thinking, problem-solving methods, communication skills, and experimental skills in the past four years. Also, thank you for your ideas, comments, suggestions on research and experimental techniques, and trust in my results. I will always miss the time when we ran and discussed experiments in the lab. Finally, I would like to thank you for your patience over the past years. For me, you are not just an excellent supervisor but also a professional and passionate mentor.

I would also like to thank my co-supervising professor, Dan Sameoto. Your course, Intro of Polymer Microfabrication, opens the door of microfluidics and microfabrication to me. All my knowledge relating to microfabrication started from this course. Furthermore, thank you for your valuable suggestions on my research.

I want to appreciate all members of nanoFAB and MECE mechanical shop at the University of Alberta. Your help and input greatly benefit the experimental setup. Among them, I would like to thank Aaron Hryciw, Stephanie Bozic, and Scott Munro for their instruction and advice on microfabrication.

Moreover, I want to thank all my colleagues with who I worked together in the Tsai Lab. Adrien Bussonniere, you are the coolest. I will not forget about our coffee break and your jumping drops in the office. Behnam Dastvareh, thank you for your encouragement and interest in my experiments. Sourayon Chanda and Ahmed Aldhaleai, thank you for buying coffee with me and patiently listen to my experiments on the way. Gregoire Bongrand, you are my best experiment and basketball partner. Masoud Bozorg, you enlighten me in ImageJ and Matlab. Junyi Yang, thank you for your collaboration. Yichi Zhang and Zhe Chen, thank you for your supportive friendship.

Last but never least, I would like to put my thankfulness to my family and friends. I feel lucky and grateful that my parents can understand and support me to fly across the Pacific Ocean to chase a dream. The weekend football party with Denny and Jack is an oasis in the desert for me, even though we win less but lose more. Who I am most grateful to is my wife, Yun-Ting. Thank you for walking with me through the tough time. You are my best friend, and no one understands me better than you do. It is you who let me know the importance of work and life balance. Without you, I may not have a good life. Without you, I may not complete this journey. Thank you!

Nomenclature

δ_f	Liquid film thickness	μm
\dot{M}_{CO_2}	CO ₂ mass change rate	kg/s
\dot{M}_{dis}	Dissolution rate of solute	kg/s
ϵ	Distance between the microfluidic chip and the flange	m
μ	Dynamic viscosity	Pa·s
ρ	Density	kg/m ³
σ_s	Stress at the corners of microchannel	MPa
σ_u	Ultimat tensile stress of silicon	MPa
τ_c	Contact time of fluid element on CO ₂ -water interface	s
θ_c	contact angle	
a	Specific area	1/m
A_b	Surface area of a bubble/droplet	m ²
c	Concentration of solute	mol/m ³
c^*	Equilibrium concentration of solute in a solvent	mol/m ³
c_0	Initial concentration of solute in a solvent	mol/m ³

C_e	Stress concentration coefficient	
C_p	Specific heat capacity	J/K
C_s	Safety factor	
Ca	Capillary number	
D	Diffusivity of solute in a solvent	m^2/s
d	Total deformation of microfluidic chip	μm
d_1	Deformation due to the fastening force	μm
d_2	Deformation due to the fluid injection	μm
d_{inj}	Diameter of injection ports	μm
d_c	Hydraulic diameter of microchannel	μm
dL_{max}^*	Dimensionless maximum size change of CO ₂ bubble/droplet	
E	Elastic modulus of the compression part	MPa
F	Fastening force	N
H	Height of microchannel	μm
h	Heat transfer coefficient for a developed thermal flow	W/(m ² K)
J	Moment of inertia of the compression part	m ⁴
J_{CO_2}	Mass flux of CO ₂	kgm ² /s
k_L	Mass transfer coefficient	m/s
$k_L a$	Volumetric mass transfer coefficient	1/s
L_b	Length of bubble/droplet	μm

L_{ch}	Length of microchannel	μm
l_c	Characteristic channel dimension	m
L_s	Length of liquid slug	μm
L_{uc}	Length of unit cell	μm
P	Operating pressure	MPa
P_{gauge}	Pressure read from the pressure gauge	MPa
P_{inj}	Injection pressure	MPa
P_{ISCO}	Pressure read from the high-pressure gas pump	MPa
P_{trans}	Pressure read from the pressure transducer	MPa
Q_L	Water injection rate	$\mu\text{l}/\text{min}$
Re	Reynolds number	
S	Solubility of solute in a solvent	mol/m^3
t	Time	s
T_i	Inlet temperature of the medium	K
T_o	Outlet of the medium	K
T_w	Temperature of channel sidewall	K
Th_{com}	Thickness of compression part	m
Th_g	Thickness of cover glass	m
Th_s	Thickness of silicon wafer	m
u_b	Mean bubble speed	m/s

V_{body}	Volume of center body of CO ₂ bubble/droplet	m ³
V_{cap}	Volume of cap part of CO ₂ bubble/droplet	m ³
V_L	Volume of solvent	m ³
V_T	Volume of CO ₂ bubble/droplet	m ³
W	Width of microchannel	μm
w_{chip}	Width of microfluidic chip	m
w_{inj}	Width of injection area	m
x	Displacement of a bubble/droplet	μm

Contents

Abstract	ii
Preface	iv
Acknowledgements	v
Nomenclature	vii
Contents	xi
List of Tables	xvi
List of Figures	xvii
1 Introduction	1
1.1 Microfluidics: Fundamentals and Applications	1
1.2 Microfluidic bubble/droplet generators	3
1.2.1 Designs of bubble/droplet generators	4
1.2.2 Flow patterns and break-up mechanisms	5
1.3 Mass transfer in microfluidic channels	7
1.4 Technology of carbon capture and sequestration (CCS)	8
1.4.1 Carbon storage in deep saline aquifers	9
1.4.2 Carbon storage in oceans	9
1.5 Microfluidic applications in CCS	10

1.5.1	The invasion and trapping mechanism of CO ₂	10
1.5.2	Salt precipitation during the CO ₂ injection	11
1.5.3	Measuring the mass transfer of CO ₂ in water	12
1.6	Review of high-pressure microfluidic platforms	12
1.6.1	General material for high pressure microfluidics	13
1.6.2	Interface methods for sustaining at high pressure	16
1.7	Thesis objectives and outline	17
2	Methodologies for High-Pressure Microfluidic Experiments	19
2.1	Microfluidic chips: designs and fabrication	19
2.1.1	Design the pattern on a photo-mask	19
2.1.2	Surface cleaning in a piranha bath	21
2.1.3	Surface coating processes	21
2.1.4	Curing and patterning	21
2.1.5	DRIE etching and characterization	22
2.1.6	Drill the connection ports	22
2.1.7	Glass bonding and dicing	22
2.2	High-Pressure and Temperature platform	23
2.3	Experimental setup	26
2.4	Operating procedures for high P/T microfluidic experiments	27
2.4.1	Preparation of the continuous liquid phase	27
2.4.2	Assembly of the high-pressure microfluidic platform	27
2.4.3	Calibration of the backpressure	28
2.4.4	Control and monitor the temperature of fluids	28
2.4.5	CO ₂ injection	29
2.5	Image analysis	29
3	Microfluidic Mass Transfer of CO₂ at Different Phases	31
3.1	Introduction	31

3.2	Material and methods	33
3.2.1	Experimental procedures	34
3.2.2	Image analysis	35
3.2.3	Determining the volumetric mass transfer coefficient	35
3.3	Results and discussion	38
3.3.1	CO ₂ bubble/droplet size change at different phases	38
3.3.2	Volumetric mass transfer coefficient under elevated pressure	41
3.3.3	CO ₂ mass transfer rate	44
3.4	Conclusions	48
4	Multiphase CO₂ Dispersions in Microfluidics: Formation, Phases, and Mass Transfer	49
4.1	Introduction	49
4.2	Material and methods	52
4.2.1	Experimental	52
4.2.2	Image analysis	52
4.2.3	Estimations of the total volume and surface area of a CO ₂ dispersion	54
4.3	Results and discussion	57
4.3.1	Multiphase CO ₂ flow and dispersions	57
4.3.2	Determination of the phase states of a multiphase CO ₂ dispersion . .	58
4.3.3	Formation of multiphase CO ₂ dispersions	62
4.3.4	Mass transfer of the multiphase CO ₂ dispersions	64
4.4	Conclusions	67
5	Microfluidic Salt Precipitation: Implications for Geological CO₂ Storage	69
5.1	Introduction	69
5.2	Materials and Methods	71
5.2.1	Microfluidics	71
5.2.2	Experimental Section	71

5.2.3	Image Analysis	73
5.3	Results and discussion	73
5.3.1	Brine Drying and Salt Precipitation	73
5.3.2	Pore-scale Salt Precipitation	78
5.3.3	Global Distribution of Salt Precipitation	80
5.3.4	Development of Extended Salt Precipitation	81
5.3.5	Effect of Porosity	83
5.4	Conclusions	85
6	Conclusions and Outlook	86
6.1	Conclusions	86
6.2	Outlook	87
6.2.1	Mass transfer of supercritical CO ₂ in the microchannel	87
6.2.2	Microfluidic salt precipitation by injecting supercritical CO ₂	88
	References	89
A	Additional data and analysis for "Microfluidic Mass Transfer of CO₂ at Different Phases"	113
A.1	EXPERIMENTAL DATA	114
A.2	MAXIMUM SIZE CHANGE	115
A.3	THERMODYNAMIC PROPERTIES	116
B	Detail analysis of phase change for "Multiphase CO₂ Emulsions in Microfluidics: Formation, Phases, and Mass Transfer"	118
C	Reproducibility data and image analysis for "Microfluidic Salt Precipitation: Implications for Geological CO₂ Storage"	121
C.1	PATTERNS of MICROFLUIDIC POROUS MEDIA	122
C.2	MICRO-FABRICATION PROCEDURES	123
C.2.1	PROCEDURE OF REPLICA MOLDING	123

C.3	DETAILS OF IMAGE ANALYSIS	124
C.3.1	POST-IMAGE PROCESSES	124
C.3.2	CALIBRATION	124
C.4	EXPERIMENTAL DATA	126

List of Tables

A.1	Thermodynamic properties of CO ₂ used in the calculations	116
A.2	Thermodynamic properties of water used in the calculations	116
A.3	The resultant dimensionless parameters for calculating the film thickness . .	117

List of Figures

2.1	Standard procedures of fabricating a microfluidic chip. The thickness of each layer is exaggerated for better visualization. The thickness of silicon chip is about 1.7 mm, and the deposition depth of hexamethyldisilazane (HMDS) and photo-resist should follow suggestions given in the operation protocols.	20
2.2	The schematic cross-section of a microfluidic chip. The thickness of cover glass Th_g is 1.2 mm, and Th_g equals 1.7 mm. For all of our design, the main channel has the width $W = 100 \mu\text{m}$ and height $H = 25 - 30 \mu\text{m}$.	21
2.3	The 3-D exploded view of high-pressure microfluidic platform designed in this study. Both the main body (1) and the compression plate (2) are made of aluminum, manufactured by the MECE shop in the University of Alberta. The tubing connector (5) has 1/8" NPT on one side and 1/16" Swagelok thread for inserting tubes. The M6 bolts (7) and nuts (8) are standard products from Thorlabs.	23
2.4	The force diagram for estimating the bending of a microfluidic chip at high-pressure conditions. Here, d represents the maximum displacement of chip pushed by the injected fluid, while the edge of a chip is assumed to be fixed on the main body.	24
2.5	Design of O-ring groove	25
2.6	The schematic setups for high-pressure microfluidic experiments	26

2.7	Snapshots of experiment data for demonstrating the image processing steps. (a) The raw sample image before processing. (b) The binarized image after enhancing the sharpness of interface and thresholding. (c) The image sequence shows the idea of tracing a moving object along the microchannel using functions in ImageJ.	30
3.1	(a) The snapshot of CO ₂ bubbles generated using a microfluidic T-junction, while subsequently moving in the channel. The water inlet has the same width as the main microchannel of a width of 100 μm, and the CO ₂ channel is 50 μm in width. The depth of microchannel is 30 μm. The (yellow) scale bar represents 300 μm. (b) The CO ₂ thermodynamic phase diagram near the critical point (yellow ●). Different symbols show our various experimental conditions for the CO ₂ injection pressure, P_{inj} , facilitating different CO ₂ phases of liquid (■), gas (●), and supercritical (▲). Image of the phase diagram is adapted from the National Institute of Standards and Technology (NIST) [207].	34
3.2	The schematic of theoretical conceptual model: (a) A unit cell. The length of a unit cell, L_{uc} , is the sum of L_b and L_s , where L_b and L_s represent the length of the CO ₂ bubble/drop and liquid plug, respectively. A bubble is surrounded by the thin liquid film of δ_f in thickness. It travels at the velocity of u_b in the channel with a hydraulic diameter d_c . (b) Higbie's penetration theory [19]: A fluid element from the bulk phase may contact the phase boundary at a finite time. During this period, the mass transfer is assumed only via molecular diffusion. The y-axis denotes the direction of mass transport, and the s-axis represents the streamline direction.	36

- 3.3 (a) Experimental snapshots of CO₂ bubbles or droplets in water in the microchannel for four different injection pressures, covering the CO₂ phase state from gas (○ and □) to liquid (◇) and supercritical state (△). As a reference of scale, the width of channel is 100 μm. CO₂ bubbles/droplets shown in (a) correspond to different locations: at initial position ($x = 0$), 4,000 μm (section 1), 9,000 μm (section 2), 15,000 μm (section 3), and 18,600 μm (section 4) away from the T-junction. Dimensionless length and length change of the CO₂ bubbles/droplets measured from the image sequences are shown in (b) and (c), respectively. In (c), the comparison of the measured CO₂ length change with the results of nonlinear regression fitting of the simplified form of Eqn. (3.6): $dL^* = \alpha(1 - \exp(-\beta x))$. The volumetric mass transfer coefficient, $k_L a$, is obtained by multiplying the fitting coefficient, $\beta = k_L a / j_L$, by the inlet water flux, j_L 40
- 3.4 The volumetric mass transfer coefficients, $k_L a$, during the rapid shrinkage stage (Section 1) against elevated injection pressures, P_{inj} . Our data span a wide range of P_{inj} , covering three different states, gas (●), liquid (■), and supercritical (▲) of CO₂. The shown points represent the average value of at least three independent experiments repeated for the same experimental conditions. Error bars denote the standard deviations. The black dashed line presents the mean value over all the presenting data, $\langle k_L a \rangle = 46.4 (s^{-1})$. Grey symbols are the maximum $k_L a$ available from previous microfluidic experimental results [113, 194, 195, 119, 120], which mostly focused on low range of P_{inj} and used a microchannel of a size greater than 100 μm. 42

- 3.5 The correlation of the measured volumetric mass transfer coefficient, $k_L a$, with (a) the capillary number and (b) the Reynolds number of the continuous liquid phase. (c) The comparison of experimental data from this study, $(k_L a)_{\text{exp}}$, and values estimated using the above empirical approximations, $(k_L a)_{\text{est}}$, previously proposed by Irandoust et al. (\cdot) [57], Bercic and Pintar (+) [112], and Vandu et al. (\times) [66]. Three different colors represent the experimental conditions in three phase states of CO_2 : green color denotes the gas state, and blue and red symbols represent the conditions using the liquid and the supercritical CO_2 , respectively. 45
- 4.1 (a) An experimental snapshot of dispersions, containing multiphase (gas/liquid) CO_2 surrounded by the continuous phase of water, generated with a microfluidic T-junction. The scale bar represents $200 \mu\text{m}$. (b) Plotted in the CO_2 phase diagram are the experimental pressure and temperature conditions (shown by \bullet) where the coexisting multiphase dispersions are observed. Experimentally, the pressure of CO_2 was gradually increased to $\approx 6.5 \text{ MPa}$ (\bullet) at room temperature, as the arrow indicates. The CO_2 saturation pressure at 23.5°C is 6.14 MPa , as the black dashed line shows the gas-liquid phase boundary of CO_2 . The phase diagram is plotted based on the database provided by the National Institute of Standards and Technology (NIST) [207]. 53

- 4.2 The schematic of an idealized microfluidic droplet, whose volume is comprised of a central section and two spherical caps on both ends. (a) Experimental snapshot of a CO₂ droplet. The black contour has a constant width, C ($\approx 8 \mu m$), for each droplet. (b) Schematic 3D model of CO₂ droplet volume. The red area is the curved CO₂-water interface, resulting in the shadow area shown in (a). (c) The top view of a droplet with a total length of $L_{\text{drop}} = 2L_{\text{cap}} + L_{\text{body}}$. L_{cap} is the length of the circular caps, and L_{body} denotes the central section of a CO₂ droplet, which is assumed to have a liquid film of a constant thickness, δ_f , between the drop and sidewall. R_1 represents the radius of spherical caps that contact the sidewall with a contact angle, θ_c . C is estimated as the width of the dark area surrounding a droplet shown in (a). Both θ_c and C are measured from experiments. (d) The schematic drawing for the droplet's side-view. A_s denotes the cross-sectional area of the fan region (OP1P2) highlighted in color green in (c). (e) The detailed dimensions of the gray area A_s in (d). (f) The drawing of the quarter cross-section of the center body through the B-B plane. 56
- 4.3 The snapshots of three different CO₂ flow patterns in our experiments: (a) the bubbly flow, (b) the intermittent flow, and (c) the annular flow. In the CO₂ channel, the inner part of CO₂ is highlighted in color light green. The yellow scale bar denotes $200 \mu m$. (d) Representative image sequences of gas-liquid coexisting CO₂ dispersions in water of the bubbly flow in (d1), the intermittent flow in (d2), and two annular flow cases in (d3)-(d4). (e) the total length, L_{drop} , of dispersions changes with time in the main channel after the microfluidic T-junction. Notably, we observed two different phase change modes in the CO₂ annular flow pattern. The first one is named Annular-1 (depicted by \blacklozenge), and the second one is called Annular-2 (depicted by \blacktriangle), respectively. 58

- 4.4 (a) The dimensionless volume of CO₂ dispersions changes with time, where V_T is estimated according to Eq.(4.1)-(4.7) and $V_{T,0}$ denotes the initial volume of a dispersion, i.e., $V_T(t = 0)$. The corresponding volume change of phase right and phase left inside the dispersion is presented in (b) and (c), respectively. Dispersions generated by the three distinct CO₂ flow patterns are shown, including the bubbly flow (●), the intermittent flow (■), and the two different CO₂ phase change behavior observed in the annular flow [annular-1 (◆) and annular-2 (▲)]. 60
- 4.5 Results of time-varying CO₂ mass change estimated according to the presumption 1 and 2. (a) and (b) compare the cumulative mass of a CO₂ dispersion, $M_T = M_{in} + M_{out}$ (kg), changes with time, where M_{in} and M_{out} represent the mass of the inner (dyed) and outer phase of the dispersion, respectively. (c) and (d) show the net mass change of CO₂ dispersions, where $\Delta M_T = M_T - M_T(t = 0)$ (kg). Here, the negative sign of ΔM_T implies the dissolution of CO₂ in the water. (e) and (f) demonstrate the CO₂ concentration change in water, estimated by dividing the absolute value of ΔM_T by the volume of adjacent water slug, V_{slug} (m³). The black dash line denotes the theoretical solubility of CO₂ in water at $P = 6.5$ MPa and $T = 23.5$ °C [247]. 63
- 4.6 (a) The semi-log plot of estimated volumetric mass transfer coefficient, $k_L a$, of CO₂ changes with time. The black dashed lines are fitting curves showing the linear relation of $\log_{10}(k_L a)$ to time t . (b) The correlations of the estimated $k_L a$ and the traveling speed of CO₂ dispersions, u_e . The black dashed line represents the linear function of $k_L a = \alpha u_e + \beta$. Here, u_e is defined by dividing the displacement from the origin by the traveling time. 67

5.1	<p>Snapshots of our microfluidic experiments: (a) The microfluidic chip is initially saturated with a dyed salt solution. The brine is displaced by air (injected from right to left) at a rate of 500 ($\mu\text{l}/\text{min}$) at room temperature and 1 atm. (b) Precipitated salt crystals (indicated by the yellow dashed lines) nucleated in a residual brine pool (shown by the mauve color). As gas was continuously injected, salt concentration gradually exceeded the saturation point because of water evaporation, leading to more salt precipitation.</p>	72
5.2	<p>Simultaneous dynamics of both brine drainage/drying (\blacktriangledown) and salt nucleation (\blacklozenge) in a well-defined microfluidic network of a constant depth, under a constant air injection (with 16.7% w/w initial salt concentration). (a) Representative experimental snapshots of salt precipitation during a brine drainage. The dimensionless time (t^*) represents a characteristic time with the definition of $t^* = (t - t_o)/(t_f - t_o)$, where t_o is the initial time of drainage, and t_f is the final time when the brine is dried completely ($t_o = 2760$ s and $t_f = 20,040$ s in this case). (b) The changes of residual brine (\blacktriangledown) and salt nucleation (\blacklozenge) volumes in time; here the dimensionless volume is normalized by the unit volume of the regular pore-structure (with a constant depth), i.e., in terms of the numbers of unit-pore. From (b), the development of salt nucleation reveals three distinct phases: (I) initial slow, (II) rapid growth, and (III) final stages characterized by different growth rates measured. Here, A_B represents data of residual brine area varying in time; A_C means the area of salt precipitation; A_P is a constant of a unit pore area we defined ($A_P = 2.51 \times 10^5 \mu\text{m}^2$ in this case; see Fig. C.1 for a detailed A_P).</p>	75

5.3	Morphologies and patterns of the salt nucleation at the different nucleation stages. Each row of image sequence reveals the development of salt nucleation with the initial residual brine area, subsequent salt precipitation patterns, and magnified salt morphologies under 5× and 20× magnifications at different nucleation stages: (a) initial stage, (b) rapid growth stage and (c) final stage, which are delineated by the different crystallization speeds measured in Fig. 5.2b.	79
5.4	The spatial and size distributions of salt precipitation for the case of $\phi = 0.52$. (a) A snapshot of salt distribution after the porous system was completely dry. The scale bar represents 2 mm. (b) Statistical analysis of the size distribution of salt precipitations nucleated at the different stages: I, II, III, shown by the bars of ■, ■, ■, respectively. This distribution diagram presents the numbers of salt-nucleation spots of particular sizes, in μm^2 (in the bottom axis) and by the numbers of unit pore size of $A_P = 2.51 \times 10^5 \mu m^2$ (in the top axis). . .	81
5.5	Development of local salt precipitation in the rapid growing regime (II). The representative image sequences are taken about 4 hours after air injection, with 10 minutes time lapse. Blue arrows indicate the flow direction of the brine, attracted by nucleated salt. Red arrows show the growing direction of salt aggregate, which attracts the fresh brine. The air flow goes from the right hand side. The scale bars represent 1 mm.	82

5.6 Correlations between the growth rate of salt nucleation and drying-rate of the residual brine in the (II) rapid growth phase of nucleation, for $\phi = 0.52$ and $\phi = 0.23$ in (a) and (b), respectively. Here, \dot{V}_{salt} and \dot{V}_{brine} represent the volumetric salt growing rate and brine drying rate, respectively; h ($= 25 \mu\text{m}$) is the uniform depth of the porous structures. (C) Data collapse of a new correlation of the data in (a) and (b) divided by the interspacing distance, s . The dashed lines represent best fitting results based on the (least-squares residual) linear fit for the corresponding variables in (a) – (c), respectively. As shown in SI Fig. S1, $s = 157.1 \mu\text{m}$ and $40 \mu\text{m}$ for $\phi = 0.52$ and $\phi = 0.23$, respectively. 84

A.1 The data demonstrate the dimensionless length change of CO₂ bubbles/droplets against the traveling distance for all of the experimental sets. Experiments for gas CO₂ are presented in (a)–(c), highlighted in the **green rectangle**. Size change in the liquid state is shown by (d)–(g), highlighted in the **blue polygon**. (h) and (i) are the cases working in the super-critical state, highlighted in the **red rectangle**. For CO₂ in gas and liquid states, three different sets of experiments were repeated (depicted by \circ , \diamond , and \triangle). For the super-critical CO₂, we ran five independent sets of experiments to confirm the reproducibility further (depicted by \circ , \diamond , \triangle , \square , and ∇). Solid symbols are the representative data shown in the paper. 114

A.2 (a) The dimensionless maximum bubble size change (dL_{max}^*) vs. CO₂ density; (b) dL_{max}^* vs. the mean bubble velocity (u_b); (c) dL_{max}^* versus the fraction of injection water. L_{s0} and L_{uc0} represent the initial length of the water slug and the unit cell, respectively. Here, the greater L_{s0}/L_{uc0} , the larger water volume is. 115

B.1	<p>The detailed calculations of a CO₂ emulsion based on the mean value from five emulsions in the case of the bubbly flow. (a) The volume fractions, $V_i(t)$, of the outer phase (V_{out}), the (dyed) inner phase (V_{in}), and the total volume ($V_T = V_{out} + V_{in}$) changing with time (t). (b) The mass of the outer phase, $M_{out} = \rho_{CO_2} V_{out}$, and the dyed, inner phase, $M_{in} = \rho_{CO_2} V_{in}$, changing with time based on Presumption 1 (assuming the inner phase is the liquid CO₂). The total mass of a CO₂ emulsion, $M_T = M_{out} + M_{in}$. (c) Results of M_{out}, M_{in}, and M_T calculated from Presumption 2 (assuming the outer phase is the liquid CO₂). (e) and (f) present the net mass change of an emulsion varying with time calculated according to presumption 1 and 2, respectively. ΔM represents the variation of mass from its initial value, $M(t_0)$. The data for the outer phase is denoted by \blacktriangleleft, while the dyed inner phase by \blacktriangleright; \bullet represents the sum properties. (d) The estimated CO₂ concentration, $C(t)$, changes with time according to presumption 1 (\bullet) and 2 (\bullet). The black dashed line denotes the theoretical CO₂ solubility in the water. (g) The estimated mass change of the dyed, inner phase resulted from the phase transition.</p>	120
C.1	<p>The patterns of microfluidic porous structures and the schematic of the unit pore area used, for two different porosity (ϕ) values: (a) $\phi = 0.52$; (b) $\phi = 0.23$. The scale bar here presents 4 mm.</p>	122
C.2	<p>(a) Process steps used for the micro-fabrication; (b) Replica molding steps using PDMS; (c) Photo of silicon template for the replica-molding method (before final cleaning); (d) A snapshot of the 2D porous PDMS microfluidics.</p>	123
C.3	<p>Post image process for extracting the signals of salt crystals and residual brine from the raw images (represented by the first row of the images) for (a) Salt nucleation and (b) Residual brine. (c) shows a calibration of the raw and the binary images.</p>	125
C.4	<p>The isolated salt nucleation (red area) and the undetected salt (spots cropped by yellow lines) after the threshold steps. The scale bar presents 4 mm. . .</p>	125

C.5 The data summary of brine evaporation (shown by \square , ∇ , and \times) and salt growing (indicated by \diamond , \triangle , and \star) rates varying with dimensionless time in this experimental study. The two columns show the two different porosity cases, and the initial salt concentration increases from the first row (16.6 wt%) to the third row (25.9 wt%). The representative data for Fig. 2 (b) in the paper is highlighted by the solid triangles (\blacktriangledown and \blacktriangle) for $\phi = 0.52$ and 16.6 wt% salt-concentration. 126

Chapter 1

Introduction

1.1 Microfluidics: Fundamentals and Applications

Microfluidics refers to the device integrating science and technology to control and manipulate fluids on a length scale smaller than hundreds of micrometers (few nanoliters of the fluid volume handled in general) [1, 2]. The development and utilization of microfluidic devices originated from chemical analysis [3] and miniaturized printing nozzles [4]. Thanks to the rapid development in micromachining and fabrication technologies in microelectromechanical systems (MEMS) [5], microfluidic applications soon extended to many other fields, including microsensors integrated with fluid controllers [6, 7], life and pharmaceutical sciences [8], material synthesis [9], chemical mixing [10] and separation [11], and fundamental researches on fluid mechanics in microscale [12, 13, 14].

A typical microfluidic flow falls in the laminar flow regime because of its low Reynolds number, defined as $Re = \rho u l_c / \mu$ [15]. Here, l_c and u refer to the microchannel's characteristic length and the working fluid's mean flow speed. ρ and μ are generally the density and viscosity of the working fluid, e.g., gas, aqueous solutions, organic solvents, and polymer solutions. Low- Re -number implies a more dominant viscous effect comparing to the inertia force [1, 4]. In addition, the influence of the gravitation effect becomes trivial at microscale. Surface forces such as pressure, interfacial tension, van der Waals interactions, and

electrical effects from surface charges, play essential roles in determining the behavior of fluids flowing in a microchannel because of its enormous ratio of surface area to volume [16]. Therefore, manipulating these interfacial forces expands the application and design scopes of microfluidics for various technological processes from both fundamental and engineering perspectives.

Microfluidics also offers useful platforms and toolboxes allowing for high-resolution investigations of the interfacial transport phenomena in well-defined micron-scale confinements. The transport phenomena across interfaces, including the transfer of momentum, mass, and heat, are important in many macro-scale systems because they determine the performance (efficiency) of the processes. The interfacial area between phases plays a key role by controlling the transport intensity in a fixed period. Microfluidic approaches can effectively create interfaces with high surface-to-volume ratio (SV) that extensively enhance the transfer process compared to most macro-systems [17]. Furthermore, the inherent small characteristic length in microfluidics significantly reduces the heat and mass transfer span. For example, fluid with an initial temperature of T_i is heated by heat convection when flowing in a circular channel of length L_{ch} , with a constant temperature T_w . The outlet temperature of the fluid, T_o , can be estimated by a classical convective heat transfer equation [18]:

$$\frac{T_w - T_o}{T_w - T_i} = \exp\left(-\frac{4hL_{ch}}{mC_P l_c}\right), \quad (1.1)$$

where h is the heat transfer coefficient, m is the mass of a unit volume of liquid, and C_P is the fluid's heat capacity. l_c represents the characteristic channel dimension. Eqn. (1.1) describes the decrease in temperature difference between T_o and T_w with a smaller l_c , implying the more rapid heat transfer in the microchannel.

Another example of transport phenomena in microfluidics concerns the 1-D mass diffusion process of a solute in a straight tube filled with solvent. The solute concentration is initially 0 at $t = 0$, and its solubility in the solvent is expressed as S . The time dependence of solute concentration change $C(t)$ can be expressed by the Fick's second law's solution [19]:

$$c(t) = S \operatorname{erfc}\left(\frac{l_c}{2\sqrt{Dt}}\right). \quad (1.2)$$

Here, D is the diffusion coefficient of solute in the solvent. l_c is the characteristic length of the channel. Eqn. (1.2) implies the diffusion time is proportional to the square of the characteristic length, $t \sim l_c^2$, telling that small dimensions can substantially reduce the equilibrium time for mass transfer.

Recently, in the light of global climate change and energy issues, microfluidics has attracted much attention in the field of energy and environmental engineering to seek more efficient methods that help inform the associated large-scale operations, such as fuel cell [20], conversion of bioenergy [21], recovery of oil (and gas) [17, 22], and the carbon storage and utilization [23, 24]. The inherently small injection area and volume in microfluidics allow a wide range of operating conditions (pressure and temperature conditions), making microfluidics well suited in energy and environment fields. This doctoral study is driven to exploit microfluidic technology in carbon storage engineering. The following sections will review the topics directly relating to this work, including the micro-channel configuration, flow regions, transport mechanisms, carbon storage technologies, and the design concept for high-pressure microfluidics.

1.2 Microfluidic bubble/droplet generators

Microfluidic bubble/droplet generators are convenient material science tools because they manage to produce highly uniform monodisperse bubbles/droplets massively, which typically act as templates with a well-defined geometry to synthesize substances for pharmaceutical, cosmetic, and food applications [25, 26, 27, 28]. These bubbles/droplets can also become platforms for fast-screening and characterization due to the inherent large surface area to volume ratio that facilitates fast mass and heat transfer and chemical reactions. Generally, bubbles/droplets are generated by utilizing the fluid instability when introducing two immiscible fluids to come together. The one has smaller surface energy with the channel sidewall breaks up to separated bubbles/droplets, called the dispersed phase. The other fluid that carries the dispersed fluid is named the continuous phase. Channel confinement and forces interactions, including the interfacial tension, the liquid viscosity, and the inertia force, play

dominant roles in creating different dispersion patterns in various designs of bubble/droplet generators [29, 30].

1.2.1 Designs of bubble/droplet generators

A. Cross-flow configuration

The cross-flow micro-bubble/droplet generator refers to the design that the channel of dispersed fluid intersects the continuous phase at the angle θ varying from $0^\circ < \theta < 180^\circ$ [31]. The T-junction configuration is the most common cross-flow design, in which the dispersed phase meets the continuous phase perpendicularly [32]. Many applications have frequently used T-junction geometry due to its simplicity in design and the capability of consistently producing monodispersed bubbles/droplets. Each individual has little size deviation according to the measured coefficient of variation (CV), giving a small value down to less than 2 %. Here, CV defines the ratio of the standard deviation to the average droplet radius [33]. After tuning the injection parameters properly, such as injection rate ratio, the production rate of T-junction can go up to 7.4 kHz reported by the experiment using air and water [34]. Besides, channel dimensions determine the minimum bubble/droplet size a cross-flow generator can achieve, usually larger than 10 μm in diameter [32].

B. Co-flow configuration

The bubble/droplet generator in co-flow configuration aligns the stream of dispersed fluid parallelly inside the continuous phase flow [31]. It can be made by inserting a tapered circular capillary tube into another rectangular microchannel or square capillary [35, 36, 37]. This type of design can produce micro-bubbles/droplets at high frequency up to tens of kHz [35]. The size of the bubble/droplet depends on the flow rate ratio and the diameter of the dispersed phase tube, which can create the finest feature down to the scale of 1 μm [38]. Besides, the flow regime (ratio of capillary number) determines the consistency of droplet size. It was reported that bubbles/droplets have little size variation as small CV as 3 % when both capillary numbers of the continuous phase (Ca_c) and the dispersed phase (Ca_d)

are low [35], while droplets tend to be polydispersed as Ca_d exceeds $O(10^{-2})$ [37].

C. Flow-focusing configuration

The flow-focusing device introduces the co-flowing dispersed and continuous phases passing through a contracting orifice. Two immiscible fluids are hydrodynamically focused and elongated in the orifice and eject bubbles/droplets after the break-up [31, 39, 40, 41]. This method can massively generate small bubbles/droplets down to hundreds of nanometers [42] with good reproducibility of $CV < 5\%$ [43], whereas it is challenging to avoid the channel wall of the orifice wetted by the dispersed phase [44]. In contrast to the conventional flow-focusing design using two parallel flows in the same direction, there is an alternative using capillary tubes to supply the dispersed and continuous phases in the opposite direction [30]. This device is similar to the co-flow configuration, which inserts two circular tapered capillaries into the bigger square one. Two tapered tips point against each other as the contraction orifice, where fluids meet and produce droplets. Notably, this method allows generating multiple emulsions in a designated order in one step [30, 45].

1.2.2 Flow patterns and break-up mechanisms

Although the micro-bubble/droplet generator's design and geometry are diverse, we can still categorize them into a few fundamental patterns according to similar hydrodynamic processes and underlying mechanisms. These flow patterns generally include squeezing [46], dripping [35], jetting [36], tip-streaming [47], and tip-multibreaking [48] according to the ratio of capillary number from the dispersed (Ca_d) and continuous phases (Ca_c). Distinct flow characteristics can associate with fluid instabilities due to the channel confinement and complex interactions of surface forces. The first three patterns were often observed in most fluidic devices, while the last two have not been reported using the cross-flow (T-junction) channel. Here, we focus on the break-up mechanisms for patterns that are available for T-junction devices for the easiness of design.

A. Squeezing

The squeezing break-up pattern happens at low capillary numbers, where both Ca_d and Ca_c are smaller than $O(10^{-2})$ [49, 50, 51]. In this range, surface tension is strong enough to keep the interfacial geometry from distorted by the viscous stress as the dispersed phase enters junctions. The dispersed fluid protrudes and gradually grows in the main channel. This protrusion, thus, restricts the continuous flow by blocking the entire main channel. Consequently, the pressure gradient builds up across the expanding dispersed fluid. The pressure from the continuous phase will finally overcome the surface tension and the pressure inside the dispersed, which "squeezes" the dispersed fluid into a bubble/droplet. The size of generated bubbles is typically larger than the channel width, leading to a plug-like shape instead of a sphere [52, 53, 54].

B. Dripping

The flow pattern will evolve from the squeezing to the dripping mode when the continuous phase's capillary number, Ca_c , increase to the order larger than 10^{-2} while Ca_d remains smaller than $O(10^{-2})$ [51]. In this range, the viscous force between the biphasic flow suppresses the surface tension that sustains the dispersed stream's integrity. Typically, the rupture happens right away as the dispersed fluid protrudes into the main channel due to the capillary instability (Rayleigh-Plateau) [14]. The formatted bubbles/droplets do not have enough time to grow bigger than channel dimensions. Therefore, the ruptured dispersed phase forms a stream of spheres in this flow region, which is explicitly different from the squeezing pattern.

C. Jetting

The jetting mode features an extended dispersed phase (jet) shoots into the continuous fluid. Bubbles/droplets are generated at the tip of the jet due to Rayleigh-Plateau instability [37]. This flow pattern occurs when the capillary number of the dispersed fluid is exceeding the threshold capillary number, $Ca_d > 0.01$ [48]. In the jetting flow region, Ca_c controls the

length and width of the shooting jet and the diameter of bubbles/droplets after the rupture. The central jet in a smaller Ca_c is shorter and wider because of the deceleration effect as a fast-moving fluid enters a medium with a slow bulk speed. As Ca_c increases, the continuous phase stretches the jet and makes it thinner and elongating further downstream due to the dominating viscous force [37].

1.3 Mass transfer in microfluidic channels

The plug-like flow pattern generated by the squeezing break-up mode at low capillary numbers, $Ca < O(10^{-2})$, is appreciated in many characterization applications because it offers a well-defined interfacial boundary, tunable volume fractions for both phases, high mass/heat transfer rate [55], and a controllable residual time [56]. This segmented flow is generally idealized by the classic Taylor bubble model, consisting of two spherical caps on both ends and a cylindrical center body. For a two-phase system without chemical reactions between fluids and fluid-sidewalls, the transport of a solute molecular from a Taylor bubble/droplet to the adjacent solvent slug includes: (1) the mass transfer via two caps of a bubble/droplet, (2) the mass transfer through the liquid film between a droplet and sidewalls, and (3) mixing of the liquid film with the liquid slug [57, 58, 59]. This mass transfer process of a plug flow is controlled by the cooperation of molecular diffusion and fluid advection. Solute molecules diffuse into the solvent as it contacts and stays on the interface in a limit of time, τ_c . The solute dissolved solvent units then mix with the bulk phase via the inherent recirculation motion inside the liquid slug [55, 60, 61, 62, 63, 64].

Nevertheless, it is challenging to differentiate the complex diffusive-convective interactions. Therefore, we introduce the mass transfer coefficient k_L (m/s) to help quantify the mass transfer rate (\dot{M}_{dis}) of the solute. k_L describes the mass transfer profile from c^* to c_0 across the fluid interface, which is influenced by combining diffusion and advection effects [19]:

$$\dot{M}_{dis} = k_L A_t (c^* - c_0), \quad (1.3)$$

where A_t (m^2) is the interfacial area between a bubble/droplet and the surrounding liquid.

c^* and c_0 (kg/m^3) represents the equilibrium and the initial concentration of solute in the solvent, respectively. For a fluid pair consisting of a Taylor bubble and a solvent slug (also known as a unit cell [57]), the concentration change of solute against time per fluid pair can be written as:

$$\frac{dc}{dt} = k_L \frac{A_t}{V_L} (c^* - c_0) = k_L a (c^* - c_0), \quad (1.4)$$

where a is the specific area defining the surface-to-volume ratio of a unit cell, and the prefactor $k_L a$ measures the efficiency of mass transfer from the solute into per unit volume of contacting solvent [19].

$k_L a$ in Eqn. (1.4) can be further broken down by considering the mass transfer contributed from the cap side and the liquid film through the center body [57, 65]:

$$k_L a = (k_L a)_{cap} + (k_L a)_{film}. \quad (1.5)$$

Here, the $(k_L a)_{film}$ term plays the dominant role in determining the overall mass transfer efficiency due to the following two reasons. On the one hand, the specific area of a droplet's center body (a_{film}) is often larger than that of caps (a_{cap}). A large a_{film} would greatly enhance the mass transfer if the liquid film remains active and well-mixed in the slug section [57, 65, 66, 67, 68]. On the other hand, the liquid film may easily get saturated with solute as passing through the long bubbles/droplets due to its thin thickness, which is normally smaller than the order of 10^{-6} m [69]. It thus becomes inactive and inhibits mass transfer [70]. Moreover, a slow-moving bubble/droplet reduces the mixing between the liquid film and the slug section because of the less intensive inner circulation [71]. The poor mixing also results in a fast saturation in the liquid film, which leads to a low mass transfer rate [72].

1.4 Technology of carbon capture and sequestration (CCS)

CCS refers to technologies that selectively remove (or capture) CO_2 from the flue gas released by industrial facilities, such as power plants, oil refineries, and cement and iron manufacture factories [73, 74]. Generally, captured CO_2 will transport to a suitable storage site after

compressed to high pressure (~ 100 bar) [75]. Storage options feature a stable geological structure that can keep CO_2 from re-emitting into the atmosphere for multiple hundreds or thousands of years [76]. They include the depleted oil and gas reservoirs, unmineable coal seams, saline aquifers, and deep ocean carbon sinks [77, 78, 79]. Among these potential sites, saline aquifers and oceans have the largest total storage capacity for CO_2 , up to the order of 10^4 Gt worldwide [80, 81]. It is, therefore, critical to get insights into these two carbon storage methods to balance ecological concerns and successful engineering deployment.

1.4.1 Carbon storage in deep saline aquifers

A deep saline aquifer is a sediment layer of relatively large pore size [82] that can store an enormous volume of CO_2 . The inherent high permeability is also appreciable from the engineering perspective because it considerably reduces the required injection pressure to deliver CO_2 compared to other formation layers with low permeability [83]. The injected CO_2 will transform to the liquid or supercritical state depending on the injection depth and replace the fluid in pore spaces (known as saline water or brine) [84]. Due to the low density of supercritical CO_2 comparing to the saline water, CO_2 gradually migrates upward, driven by the buoyant effect until being trapped by the caprock layer [85, 86]. The caprock is a low-permeability layer working as a seal that essentially confines CO_2 inside the aquifer layer and prevents leakage [87]. Consequently, CO_2 starts dissolving in the saline water and reacting with rocks and minerals in the formation, and hence CO_2 is anchored beneath the earth surface for a long time [88].

1.4.2 Carbon storage in oceans

The ocean sequestration of CO_2 refers directly to inject the compressed anthropogenic CO_2 into the ocean. The injected CO_2 will dissolve in the seawater when it rises like a bubble/droplet plume or sinks to the seabed, forming a CO_2 lake [80]. CO_2 density increases with a deeper injection depth, and it will become similar to the seawater's density at an injection depth of 3000 m. Above this depth, CO_2 gradually rises due to buoyant force.

Part of the injected CO₂ will return to the atmosphere after staying in the ocean for some time, while part of it dissolves in seawater [89, 90]. Alternatively, CO₂ tends to stay in a certain depth or sink to the seabed surface when the injection depth is deeper than 3000 m. In such conditions, the CO₂ hydrate forms if the concentration of dissolved CO₂ is high. The hydrate phase is a solid material that each CO₂ molecule sits in a cage-like structure of water molecules held together by hydrogen bonds [80]. The formation of hydrate helps CO₂ trapped in the seabed longer due to the higher density than seawater [91].

1.5 Microfluidic applications in CCS

Microfluidics is a helpful tool to measure and analyze the mass transfer of CO₂ for the carbon capture and sequestration technologies (CCS) due to the merits of good spatial and temporal resolution [17, 21, 23]. Besides, the capability of precisely controlling a small sample volume makes experiments more time and cost-effective and environmental-friendly [22]. The microfluidic works relating to the CCS applications have two primary groups: capture and storage [23]. The CO₂ capture studies emphasize the rapid and accurate screening for an efficient CO₂ separation from flue gas using solvents; Researches on the CO₂ storage aim to understand insights into CO₂-liquid-rock interactions in pore-scale by applying the direct visualization method to the microfluidic models that mimic rock formations. Current microfluidics studies on the CO₂ storage are engaging in three major topics: the invasion and trapping mechanism of CO₂, salt precipitation, and measuring the mass transfer of CO₂ in water. The following subsections will introduce the background and current development of each topic accordingly.

1.5.1 The invasion and trapping mechanism of CO₂

The displacement patterns of CO₂ invading into the pore-liquid (brine) is critical for achieving the optimum CO₂ storage volume after the injection [92]. In this early storage stage, the structural trapping is considered as the most time-effective mechanism to confine a large volume of CO₂ beneath the caprock [93, 94]. Therefore, the porosity of formation and the

saturation of residual liquid are two main factors affecting this trapping mechanism at the early stage [95].

Microfluidics allows us to directly visualize the propagation of injected CO₂ and present the results quantitatively, for example, the drainage rate, the saturation of residual brine, and the contact angle on the CO₂-brine-solid interface. A few microfluidic experiments have been reported the invasion patterns of CO₂ under different injection flow rates [96, 97, 98]. The distribution and saturation of residual brine under different injection pressure are also observed and measured. In general, injecting CO₂ in the liquid state shows a better drainage efficiency due to the higher viscosity and contact angle [99, 96, 97, 100, 98]. Other methods to increase the displacement efficiency of CO₂ are developed as well, including adding a surfactant to brine before injection [101] and injecting the CO₂-water foam [98].

1.5.2 Salt precipitation during the CO₂ injection

Salt precipitation could be a potential threat for the storage of CO₂ in deep saline aquifers according to the current core-flooding experiments and simulation results [102, 103]. The precipitated salt can reduce the permeability of formation by blocking the pore network. It, therefore, increases the required injection pressure of CO₂ and reduces the injectivity and capacity of the storage site [104].

Microfluidic approaches offer an excellent chance to understand the salt-brine interaction in the pore-scale further [21, 105, 106, 107, 108, 109]. Recent results have identified that salt precipitation is composed of two different crystal forms: bulk crystal and poly-crystalline aggregate [105]. The poly-crystalline aggregate can further develop itself via attracting fresh brine from the brine pools near around due to the hydrophilic nature of salt [106]. Salt prefers to deposit locally on the water-wet surface of fractures in the reservoir rather than oil-wet surfaces because the thin brine film bridges the brine sources and the evaporation front [109]. Additionally, it is found that the injection of gas CO₂ resulted in more extensive salt precipitation comparing to the liquid and supercritical CO₂ injections, which can attribute to the poor drainage efficiency of brine during the gas injection [108].

1.5.3 Measuring the mass transfer of CO₂ in water

Investigating the dissolution of CO₂ in water (or brine) is important for the CO₂ sequestration in the deep saline aquifer and oceans [110]. Parameters such as solubility and dissolution rate are crucial to evaluate the capacity and security of CO₂ storage in the operation site [111]. Many experiments in milli- and micro-scale have investigated parameters that may influence the mass transfer of CO₂ in water under atmospheric pressure conditions [57, 112, 66, 113, 114, 115, 116].

However, microfluidic studies that address the CO₂ dissolution behavior in water at reservoir conditions are still limited. Liu *et al.* observed that the solubility of supercritical CO₂ decreases as the increase of salinity by using the Raman spectroscopy approach [117]. Sell *et al.* presented that the liquid side diffusion coefficient is independent of the increased pressure from 1 to 5 MPa. The increased salt concentration significantly reduces the liquid diffusivity to 1/3 when the salinity increases from 1M to 5M [118]. Yao *et al.* reported the dissolution rate of a liquid CO₂ droplet is enhanced by increasing the injection pressure up to 3 MPa [72, 119]. Qin *et al.* investigated the influence of injection ratio of supercritical CO₂ and water on the mass transfer coefficient k_L at 8 MPa and 40 °C, showing that shorter CO₂ droplet results in a faster mass transfer [120].

1.6 Review of high-pressure microfluidic platforms

The development of the microfluidic devices withstanding the high-pressure and temperature conditions are originated from the needs for integrating the functionalities of conventional high P-T metal batches and continuous reactions into microfluidics [121]. High-pressure microfluidics expands the operating ranges considerably for several chemical applications, including the synthesis of nanoparticle [121, 23], solvent extractions [122, 123], catalytic hydrogenation [124, 125, 126], and esterification reactions [127]. Materials such as metal, glass, silicone, and polymers have been utilized in high-pressure microfluidic applications after applying a proper interfacing technique. The following subsections will discuss the

advantages and drawbacks of these materials. The primary interfacing method will be also introduced.

1.6.1 General material for high pressure microfluidics

A. Metal-based microdevices

Microdevices made of metal (generally stainless steel) are excellent options for high-temperature processes and handling toxic chemicals due to the good thermal and chemical resistance [128] as well as the existing interfacing connectors for current macro-applications. Two different variants were often used, the stainless steel tube and the microchannels engraved on the metal piece [129, 130, 131, 132, 133]. The stainless steel tubings provide cheap and straightforward approaches to achieve high-pressure experiments on small scales (milli and micro) and accurately manipulate experimental parameters such as temperature gradient and flow rate [131, 121, 133].

Micropatterns engraved metal devices are usually fabricated using conventional micromachining [134], electro-discharge machining (EDM) [135], and laser ablation [136]. These devices were reported operating in the temperature and pressure range up to 650 °C and 25 MPa for the gasification of organic molecules using supercritical water [129, 130]. Although the metal-based microdevices have advantages in the budget and relatively simple fabrication steps (no reliance on cleanroom apparatuses), this material is limited by the minimum feature size of several tens of micrometers ($> 50 \mu\text{m}$) due to the capability of micromachining tools [121]. Furthermore, this kind of device is difficult to realize the in-situ characterization and simultaneous visualization because of the challenge of offering optical access in the metal substrate.

B. Glass/glass microdevices

Glass-based microfluidics made of Pyrex glass (borofloat) [137] or the soda-lime glass [138] is another option for chemical and biological applications due to its cost efficiency, good chemical durability and biocompatibility, the capability for surface functionalization, and optical

transparency in a wide range of wavelengths [139, 140]. After carefully bonding two glass pieces and silica fibers at the temperature of 600 °C for several hours, glass microfluidics can sustain high-pressure conditions up to 69 MPa at room temperature [141]. It is noteworthy that the mechanical strength of glass decreases with the rising temperature [142], which limits the temperature range of most experiments using glass microdevices between 20 – 100 °C [124, 127, 143]

The diverse patterning techniques for glass microfluidics offer additional benefits to adapt to different laboratory requirements, including classical micromachining [144], dry plasma etching [145, 146, 147], and chemical wet etching [148, 137, 149]. The mechanical patterning method includes drilling with diamond bits, powder blasting, and laser machining. This method is more cost-effective than the dry and wet etching methods because of no cleanroom requirement [144]. However, the method is constrained by the machining capability of tools in patterns' size and the poor surface finish on the patterning area. Techniques of deep reactive ion etching (DRIE) using the inductively coupled plasma system (ICP) from sulfur hexafluoride (SF_6) [145, 146] or octafluorocyclobutane/fluoroform ($\text{C}_4\text{F}_8/\text{CF}_3$) [147] gases can generate high aspect ratio microstructures on the glass with smooth surface. This method somehow is labor, time, and cost consumed due to the low etching rate of about 0.5 $\mu\text{m}/\text{min}$ reported [150].

The chemical wet etching process provides a more straightforward and more cost-effective solution to pattern the glass microdevice than the dry etching technique [150]. Generally, this method creates patterns via dipping the glass substrate with a mask layer into the etching baths, such as concentrated hydrofluoric acid (HF) [149], the mixture of hydrofluoric acid and hydrochloric acid (HF/HCl) [150], or the aqueous solution of hydrofluoric acid and nitric acid (HF/ HNO_3 / H_2O) [151]. The main challenge for wet etching is to choose a proper mask layer material. The composition of the mask and its adhesion to the glass substrate are crucial to the quality of fabricated microstructures [151].

C. Silicon/glass microdevices

Silicon-based microfluidics generally composes silicon wafers and borofloat cover glass thermally bound together using the anodic bonding method [152]. This kind of device is advantageous to many applications through its inert nature to chemicals, high mechanical strength for accessing high-pressures [153], and the easy visualization from the glass side [154]. Unlike glass-based microfluidics has a limited operation temperature, silicon has an excellent thermal conductivity that makes it more feasible in a broader range of operating temperatures [155, 156]. Moreover, silicon-based microdevices can achieve integrating sensors into complex pattern designs by taking advantage of well-developed MEMS technologies [5]. Both wet and dry etching procedures allow fabricating high-aspect-ratio microchannels with controllable channel dimensions and sidewall profiles [157, 158], which makes it more appreciable due to the well-defined and reproducible boundary conditions.

Nevertheless, the brittle nature of both silicon and borofloat glass makes experiments at high-pressure conditions more challenging. A proper interfacing design that considers the leakage of working fluids and the maximum chip bending from cracking is crucial, which will discuss in more detail later.

D. Microdevices made of other materials

The fused-silica capillary-based microreactor has been experimentally proved to operate adequately at the injection pressure up to 60 MPa [159]. This pressure range is wide enough for operating experiments using supercritical fluids. They were utilized to investigate the pressure influence on the shifting of flow regimes from the immiscible co-flow system using supercritical CO₂ and water (18 MPa and 50 °C) [160] and to synthesize the Zinc oxide nanocrystals (ZnO NCs) under the condition of 25 MPa and 250 °C [161].

Polymer-based microfluidics such as PMMA is a convenient option for high-pressure applications due to its good chemical compatibility and non-porous solid nature [162]. It is also feasible for fast prototyping using laser ablation techniques to create miniaturized patterns down to 50 μm [163, 162]. Some experimental works have successfully utilized PMMA based

microfluidics for high-pressure purposes up to 5 MPa, which include investigating the influence of pressure and salinity on CO₂ diffusivity in brine [118], measuring the pressure effects on the two-phase slug flow [72], and quantifying the mass transfer rate [119]. Alternatively, some recent studies have reported the polymer-based microfluidics that can sustain the operating pressure up to 20 MPa using the ceramic-like polymer polyvinylsilazane (PVSZ) [164] and the UV-curable off-stoichiometry thioenes (OSTEs) [165]. Nevertheless, both materials' finest feature is between 200 – 500 μm , limited by the fabrication steps for fast prototyping. They will need more experimental works to explore their capacity further.

1.6.2 Interface methods for sustaining at high pressure

The most critical and challenging task for operating microfluidics at high pressures (or/and temperatures) is to interface microfluidics to external fluid handling systems, including syringe pumps, backpressure regulators, and sample collectors. There are two primary methods for connecting microfluidics: (1) permanent integrated connections and (2) replaceable modular connections [166].

The first integrated connection method refers to directly bond tubing and microfluidics using epoxy glue [167, 141, 168], metal solder [169, 170], and glass brazing [171, 172] or anodic bonding of Kovar tubes [173]. Although these approaches can withstand more than 30 MPa with unique interfacing design and treatment [171, 141, 170], they generally require additional delicate microfabrication steps to achieve the best connection strength. Besides, this direct connection method can be more cost- and time-consuming for the long term because interchanging microfluidics is not allowed.

The second method, replaceable modular connection, usually utilizes an external manifold to apply compression force on rubber O-rings [174] or elastic gaskets [175] to prevent leakage from microfluidic systems. This approach has been proved to sustain the injection pressure up to 45 MPa after using correct O-rings and groove designs [153], which have been commercially developed [176]. In addition, the modular connection provides a convenient way to interchange microfluidic chips. Most importantly, the external packaging components

can be manufactured by current machining techniques that make this interfacing method more flexible for different laboratory requirements. The major challenge of modular connections is to apply a uniform compression force onto the microfluidic chip and O-rings without too much bending. Thus, clamping locations and the contact area between the microfluidic chip and the external manifold play crucial roles in designing the replaceable modular connection.

1.7 Thesis objectives and outline

This thesis aims to provide insights into how CO₂ transport in the pore-scale under reservoir conditions using a high-pressure microfluidic method. This experimental work addresses critical transport phenomena for current carbon storage technologies, which offers essential data for macro-scale operations using lab-scale experiments. An introduction to microfluidics fundamentals, CCS background, current microfluidic applications, and the review of high-pressure microfluidic methods is given in this chapter.

Chapter 2 describes the methodology for our high-pressure microfluidic experiments. Processes include the design and microfabrication of the silicon-glass bonded fluidic chips, the external high-pressure microfluidic interface design, and the complete experiment procedures for the injection pressure up to 10 MPa.

The influence of different thermodynamic states on the microfluidic CO₂ mass transfer is experimentally investigated in **Chapter 3**. The CO₂ phase state covers from the gas to the supercritical state. Notably, the mass transfer data for supercritical CO₂ in the microchannel is still rare in the literature. Besides the pressure effects, the influence of other parameters such as the capillary number (Ca) and the Reynolds number (Re) are discussed.

In **Chapter 4**, we present intriguing and remarkable multiphase coexisting CO₂ emulsions, generated by a two-phase CO₂ flow merging with water at the microfluidic T-junction, as the operation condition is close to the gas-liquid phase boundary of CO₂ ($P_{inj} = 6.5$ and $T = 23.5$ °C). A strategy to differentiate the phase state of CO₂ inside an emulsion is developed. The emulsion's mass transfer is also quantified by calculating the dissolution rate

and estimating the volumetric mass transfer coefficient.

Chapter 5 addresses a specific engineering challenge for the carbon storage in deep saline aquifers: salt precipitation. We apply a well-defined 2-D porous network to visualize and analyze the dependence of salt growing rate and distribution on the brine-drying rate.

Chapter 6 summarizes the primary outcomes of the thesis work. Some suggestions and plans for future research regarding the mass transfer of supercritical CO₂ and potential applications for our high-pressure microfluidic platform are included.

Chapter 2

Methodologies for High-Pressure Microfluidic Experiments

2.1 Microfluidic chips: designs and fabrication

This study applies the standard photolithography procedure [177] followed by the deep reactive ion etching method (DRIE) [178] to create desired patterns onto silicon wafers. The patterned wafer can become the mold master for the replica molding process to fabricate repeating patterns, such as polydimethylsiloxane (PDMS) based microfluidics. It can also directly serve as silicon-based microfluidic after bonding with a cover glass. Fig. 2.1 illustrates the fabrication steps for making a microfluidic device's including the photo-mask design. The following subsections will describe the fabrication procedures in more detail.

2.1.1 Design the pattern on a photo-mask

To design a microfluidic chip in high-pressure applications, we have to consider the strength of silicon substrate after the etching process. The design criteria proposed by Marre *et al.* [153] suggests that the interspacing between two channels, z , should be at least equal to the channel width, W , as seen in Fig. 2.2. The applied stress at the corner of the microchannel, σ_s , has to be smaller than the ultimate tensile stress of silicon, σ_u , as shown

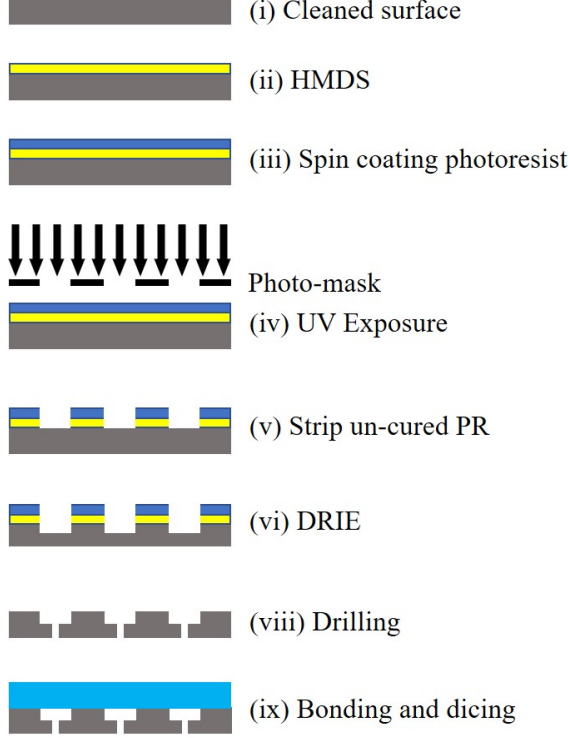


Figure 2.1. Standard procedures of fabricating a microfluidic chip. The thickness of each layer is exaggerated for better visualization. The thickness of silicon chip is about 1.7 mm, and the deposition depth of hexamethyldisilazane (HMDS) and photo-resist should follow suggestions given in the operation protocols.

in the following estimation:

$$\sigma_s = C_e C_s \frac{PW^2}{2(Th_s - H)^2} < \sigma_u, \quad (2.1)$$

where W and H represent the width and height of a channel, Th_s denotes the thickness of a silicon wafer, and P is the operating pressure. C_e is the coefficient associating with the stress concentration at the channel's corner, and C_s is the safety factor. Our design gives the maximum $\sigma_s = 11$ MPa as $P = 30$ MPa, assuming C_e and C_s equal to 10 [179]. This value is smaller than the ultimate tensile stress of silicon given in the literature, $\sigma_u = 1$ GPa at room temperature [180].

The fabrication of photo-mask in this study was helped by the Nanofab in the University of Alberta. They only accept the designing patterns in the file of GDS II format. We deployed and exported our designs by using an IC layout editor, KLayout, directly.

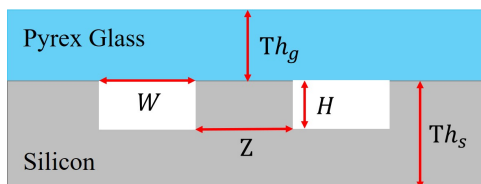


Figure 2.2. The schematic cross-section of a microfluidic chip. The thickness of cover glass Th_g is 1.2 mm, and Th_g equals 1.7 mm. For all of our design, the main channel has the width $W = 100 \mu\text{m}$ and height $H = 25 - 30 \mu\text{m}$.

2.1.2 Surface cleaning in a piranha bath

We can initiate the fabrication process for MFs after the photo-mask has been made. We use 4" prime grade round silicon wafers as substrates. Silicon wafers have to be dipped in a piranha solution first for 15 minutes to remove contaminants on the surface. Piranha solution is a mixture of sulfuric acid (H_2SO_4) and hydrogen peroxide (H_2O_2) in a volume ratio of 3:1, which is highly reactive to organic materials. It should be noted that we must pour the H_2O_2 liquid into the H_2SO_4 solution, and not the other way around. The mixing ratio of the two solutions should be larger than 2:1 for safety concerns.

2.1.3 Surface coating processes

After the piranha bath, wafers are coated with a hydrophobic layer by the hexamethyldisilazane (HMDS) vapor treatment to promote photoresist adhesion on the silicon wafer. Subsequently, a positive photoresist (HPR 504) is coated evenly on top of the HMDS layer by using a spin coating device at 2000 rpm for 40 seconds. We solidify the photoresist by soft baking the coated wafer on a hotplate at 115° for 90 seconds.

2.1.4 Curing and patterning

We install the coated wafer and the photo-mask into the mask aligner to generate photoresist patterns by exposing the UV light for 3 to 4 seconds. The photo-mask blocks out the UV light and hence keeps the underlying photoresist cured. The UV-exposed, degraded photoresist will dissolve in the photoresist stripper solvent (354 developer) after 90-second-long developing step.

2.1.5 DRIE etching and characterization

We apply the deep reactive ion etching method (DRIE) to create the final pattern on silicon wafers. The photoresist patterned wafers were placed in the inductively coupled plasma reactive-ion etching machine (ICP-RIE, Oxford Estrelas, DSE). A standard etching recipe (Bosch high rate standard) was chosen to form the pattern with an etching rate of about 1 μm per cycle. During this etching step, the photoresist layer protects the silicon surface from high energy-intensity plasma bombardment. The unprotected area will be etched to a designated depth. We calibrated the depth of patterns using a 2D surface topography profiler (Alpha-Step IQ) after each etching process to secure each wafer's consistency.

2.1.6 Drill the connection ports

In the Nanofab, we use the drill press (Servo Precision, 7140-M), with a drill of 1.4 mm in diameter, operated at the spin rate of 9000 rpm to create tubing ports on silicon wafers. It is challenging to create these holes without breaking them by drilling manually. We first bound the wafer with a borofloat glass on a hotplate using the Crystalbond adhesive (CrystalbondTM 509) for reinforcement. This process helps reduce bending on the wafer's surface as drilling holes. The Crystalbond melts at about 120 $^{\circ}\text{C}$ and is dissolvable in acetone.

2.1.7 Glass bonding and dicing

After the drilling step, wafers need to be baked in a barrel etching oven (Branson 3000 Barrel Etcher) for 20 to 30 minutes and washed in the piranha bath again for 10 minutes to remove the residual photoresist and surface contamination. The clean wafer will be bound with a borofloat glass of 1.2 mm in thickness in a glass bonder (SUSS) at 350 $^{\circ}\text{C}$ for at least 60 minutes (including bonding and cooling steps). The glass-bounded wafers will be tailored to a proper size for later experiments using the glass blade dicing saw (Disco 3240).

2.2 High-Pressure and Temperature platform

The high-pressure microfluidic platform designed in the study consists of five primary components, as shown in Fig. 2.3. The injection part acts as the main body of the platform, which contains a microfluidic chip and introduces working fluids into the chip from external sources, such as water and CO₂. The compression part covers the microfluidic chip on the injection part together with an aluminum block to form a rigid assembly that can sustain high-pressure environments after being fastened with four M6 bolts. The aluminum block is one of the crucial components that applies a uniform force onto the microfluidic chip. It prevents over-bending the brittle silicon-glass substrate when applying fastening forces on the four corners.

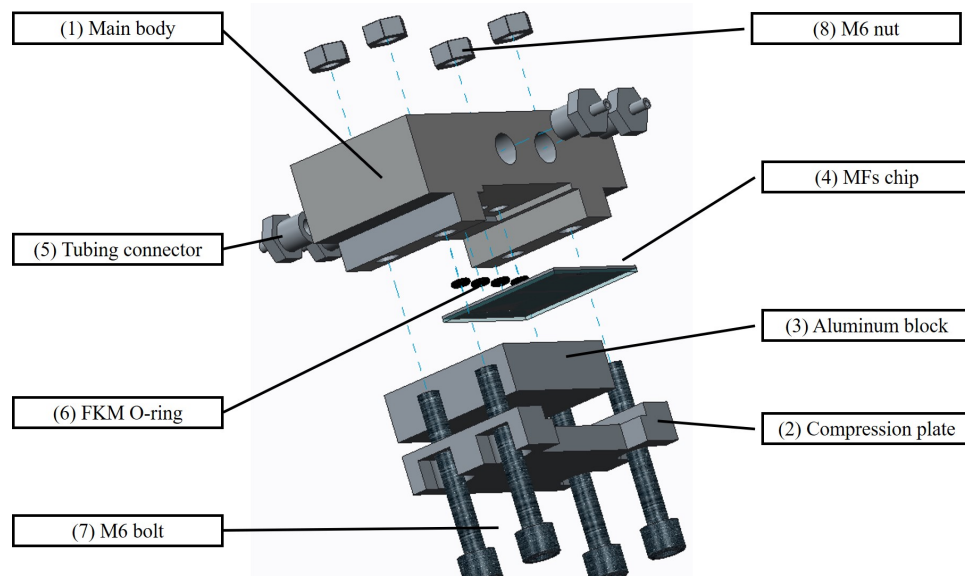


Figure 2.3. The 3-D exploded view of high-pressure microfluidic platform designed in this study. Both the main body (1) and the compression plate (2) are made of aluminum, manufactured by the MECE shop in the University of Alberta. The tubing connector (5) has 1/8" NPT on one side and 1/16" Swagelok thread for inserting tubes. The M6 bolts (7) and nuts (8) are standard products from Thorlabs.

We evaluate the performance of this platform design by estimating the maximum possible deformation of the microfluidic chip during the high-pressure experiment, d [169, 153]. The force diagram in detail for this analysis can be seen in Fig. 2.4. The total deformation of microfluidic chip can be estimated by:

$$d = d_1 + d_2, \quad (2.2)$$

where d_1 is the deformation due to force F applied by M6 bolts, and d_2 is the contribution coming from the fluid pressure that acts onto the microfluidic chip. d_1 and d_2 can be estimated via [169, 153]

$$d_1 = \frac{F\epsilon w_{\text{chip}}^2}{8EJ}, \quad (2.3)$$

$$d_2 = \frac{F}{384EJ} (w_{\text{inj}}^2 - 4w_{\text{chip}}w_{\text{inj}}^2 + 8w_{\text{chip}}^3). \quad (2.4)$$

Here, the force applied by M6 bolts, F , is equal to the load exerted by the injection pressure P . F is estimated by multiplying P with the total injection area. E denotes the elastic modulus of the compression part. $J = Th_{\text{com}}^3 d_{\text{inj}}/12$ is the moment of inertia of the compression part, where Th_{com} is the height of the compression part, and d_{inj} is the diameter of injection ports [153]. w_{chip} is the width of the microfluidic chip. w_{inj} is the width of the injection area. The ϵ denotes the distance between the flange and the microfluidic chip. Our design gives a total deformation d of $7.23 \mu\text{m}$ when the injection pressure was assumed to be 60 MPa, the theoretical maximum pressure we can achieve using the gas pump (ISCO 100DX).

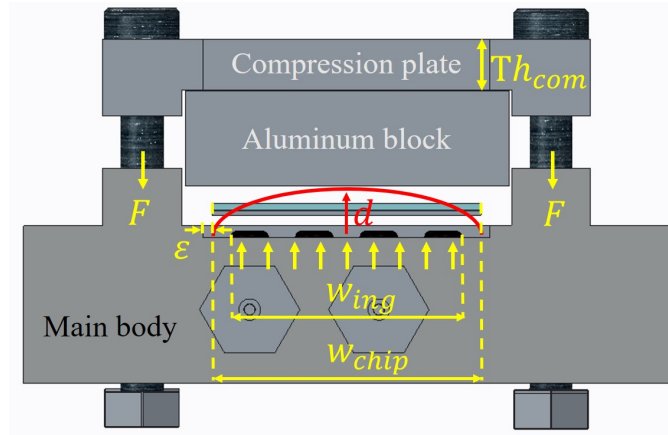


Figure 2.4. The force diagram for estimating the bending of a microfluidic chip at high-pressure conditions. Here, d represents the maximum displacement of chip pushed by the injected fluid, while the edge of a chip is assumed to be fixed on the main body.

Fig. 2.5 shows the design of the injection part's O-ring groove, which is the most crucial feature on a high-pressure microfluidic platform. As seen in the figure, our O-ring groove design has an outer diameter (OD) of 7.3 mm and an inner diameter (ID) of 2.9 mm with a height of 1.3 mm. It gives a squeeze ratio of 25.3 % after installing a standard fluorocarbon O-ring (VitonTM Duro 90A) with 2.9 ± 0.13 mm in ID and 6.45 ± 0.76 in OD . Our design can sustain under the injection pressure of 20 MPa for 16 hours without breaking and leakage after a series of sealing tests. The Viton fluorocarbon O-ring serves excellent performance for high-pressure CO₂ applications. This material has better resistance to the mechanical damage caused by rapid gas depressurization (RGD). When operating in high pressures, CO₂ molecules can penetrate and reside in the polymer (O-ring in our applications) much easier than in low-pressure conditions. RGD happens due to the expansion of penetrated CO₂ molecules during the pressure releasing process. It makes the O-ring swelling and fragile. The released CO₂ would also carry organic contamination dissolved from the O-ring and deposit in the microchannel.

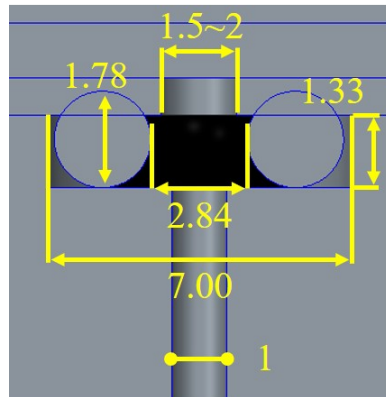


Figure 2.5. Design of O-ring groove

2.3 Experimental setup

The experimental setup for this research is shown schematically in Fig. 2.6. A cylinder tank (PRAX-AIR, 99.998% RES K) supplies CO₂ (a) directly to a high-pressure gas pump (ISCO, 100DX) (b), using the 1/4" stainless steel tube. This pump can regulate the gas pressure up to 69 MPa, covering the range for most high-pressure microfluidic applications [121]. The other working liquids (DI water and brine) are supplied by a high-pressure syringe pump (Chemyx, Fusion 6000) (c), which allows us to inject liquid at an adjustable flow rate and temperature. The maximum operating pressure of this pump depends on the size of the syringe. According to our tests, the maximum injection pressure is about 20 MPa using the 6 ml stainless steel syringe. Both of ISCO gas pump and Chemyx syringe pump connect to the high-pressure microfluidic platform (d) directly using the 1/16" stainless steel tube. The outlet of the microfluidic platform is connected with a backpressure regulator (TESCOM, 26-1700 series) and a pressure transducer (Omega, PX-309) coupling with a digital reader (Omega, Platinum) to control and monitor the backpressure simultaneously (e). The setup includes an inverted microscope (Zeiss, Material 7) (f) coupled with a high-speed grayscale camera (Phantom, VEO 710L) (g) for visualization and image recording. The operating temperature is regulated by a ceramic heating plate directly connected to a DC supplier with an adjustable output current and voltage (h). The chip temperature is monitored by a K-type thermocouple and a digital data logger (i).

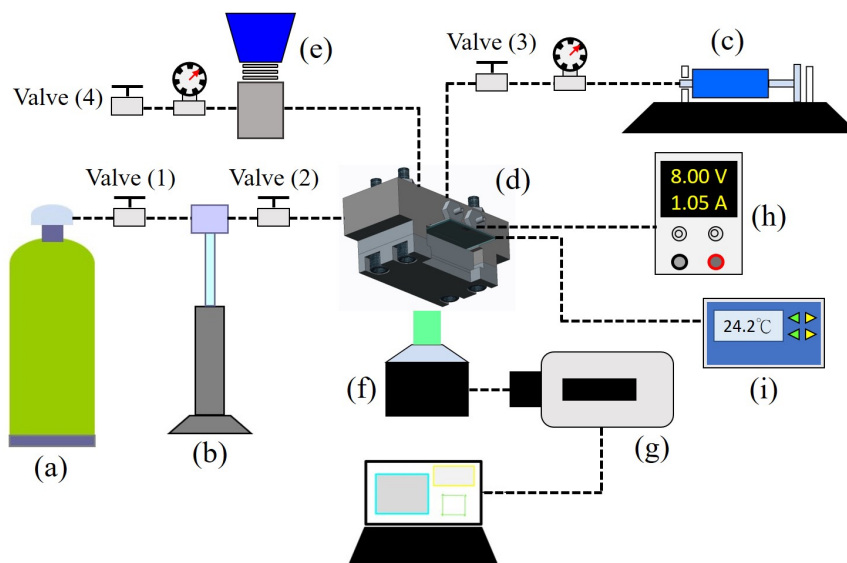


Figure 2.6. The schematic setups for high-pressure microfluidic experiments

2.4 Operating procedures for high P/T microfluidic experiments

2.4.1 Preparation of the continuous liquid phase

We first degas the ultra-clean water gathered from the water purification device (ELGA LabWater, PURELAB®) for at least 30 minutes to remove the dissolving gas in the water as much as possible. The degassed water is loaded into the 6 ml stainless steel syringe and installed on the high-pressure syringe pump. After the syringe is connected, we run the syringe pump to fill the tubing space in the injection section, as seen in Fig. 2.6 (c). To make sure there is no air in the tubing, we turn off the switch valve (3) until water starts dripping out of the tubing connector, which connects the syringe pump (c) and the microfluidic platform (d). We can then adjust the injection pressure of the continuous phase up to the designated pressure via injecting and withdrawing the continuous liquid. This step is essential in our high-pressure experiments for preventing the CO₂ backflow to the water injection section. As operating at high-pressure conditions, CO₂ will invade the syringe and mix with water if we kept a low initial pressure of continuous phase. It leads to an increase in the initial CO₂ concentration in the water, which is unfavorable because of the fundamental assumption of experiments: water is initially free from CO₂.

2.4.2 Assembly of the high-pressure microfluidic platform

The assembling of the high-pressure microfluidic platform includes the following steps. The number of the component is shown in Fig. 2.3.

1. Install four stainless steel connectors (Swagelok, 1/16" OD-1/8" NPT) on the main body using the 1/8" NPT end. A PTFE tape can be applied for performing better sealing and water resistance.
2. Place the FKM O-ring onto the O-ring groove of the main body and insert and microfluidic chip.
3. Put the aluminum block sitting on the microfluidic chip and cover the compression part on top of the aluminum block.
4. Clamp the whole assembly using four M6 bolts and nuts. We set a torque wrench with a fastening torque of about 10 lb-in and fasten the bolt and nut diagonally to apply the uniform

torque force.

5. Place assembly on the inverted microscope and connect with injection (continuous phase and CO₂) and the outlet sections using the 1/16" OD stainless steel tube.

2.4.3 Calibration of the backpressure

It is important to zero the backpressure before running experiments. After the high-pressure microfluidic platform is connected, the backpressure regulator must be fully open (turn counterclockwise) to equal the atmospheric pressure. Initiate the pressure transducer by supplying a stable direct current of 15 V and 9 mA from a power supply. The reading from the data logger now should be around 0.000 ± 0.001 due to the gauge pressure being monitored. After the calibration, turn the backpressure regulator clockwise to close the system completely.

The pressure transducer measures the pressure ranging from 0 to 51.7 MPa with a linear voltage output from 0 to 5 V. We calibrated the pressure transducer by comparing the reading from the data logger with the data obtained from the ISCO high-pressure pump and mechanical pressure gauge (reference value). The results showed that the pressure difference between the ISCO pump, P_{ISCO} , and the pressure gauge, P_{gauge} , is always less than 0.1%. Therefore, we consider that P_{ISCO} is accurate enough as a reference value. The deviation presented below will be the relative error between P_{ISCO} and data from the pressure transducer, P_{trans} , which is expressed as $|P_{trans} - P_{ISCO}|/P_{ISCO}$. Here, the maximum error was about 3.3% as $P_{gauge} = 3.45$ MPa. The error decreased to about 1.6% as P_{gauge} raised to 11 MPa.

2.4.4 Control and monitor the temperature of fluids

Before the injection, we gradually heated up the high-pressure microfluidic platform to about 60 °C using a ceramic-covered heat plate directly affixed, which connects to a DC power supply with adjustable voltage and current outputs. Meanwhile, the temperature of the microfluidic chip will increase due to the good thermal conductivity of aluminum and silicon. We wait until the chip temperature reaching the target temperature (for instance, 35 °C for the experiment using supercritical CO₂) and start injecting the working fluids. Two thermocouples were applied for monitoring the temperature on the heat plate and the microfluidic chip. After flowing through the heated microfluidic platform, the temperature of injected fluids (T_o) was estimated, by applying the classic heat

transfer calculation assuming a constant sidewall temperature, T_w , via

$$T_o = T_w - (T_w - T_i) \exp\left(\frac{-hA_s}{\dot{m}C_p}\right), \quad (2.5)$$

where T_i is the initial temperature of the injected fluid before introduced into the microfluidic platform. h denotes the heat transfer coefficient for a fully developed thermal flow. \dot{m} is the mass flow rate of the injected liquid. C_p represents the specific heat capacity of the fluid. A_s is the total surface area of the injection channel. According to Eqn. (2.5), CO₂ with an initial temperature of 20 °C and the injection rate of 20 $\mu\text{m}/\text{min}$ will increase to about 50 °C if we kept the temperature of the microfluidic platform above 60 °C.

2.4.5 CO₂ injection

After finishing the steps mentioned above, we can initiate the CO₂ injection by switching on the check valve (2), as seen in Fig. 2.6, to steadily introduce CO₂ into the microfluidic system. It should be noted that the check valve (1) and (3) should remain off to prevent CO₂ flowing into the syringe pump and the CO₂ tank. Second, we carefully ramp up the pressure to the target value using a constant flow rate when the pressure in the system reaches a steady-state ($P_{trans} \sim P_{ISCO} \pm 3\%$). Third, after reaching the target pressure, switch the pump program to the "constant pressure mode" that keeps the pump pressure at a constant value and wait until the system becomes stable again (P_{trans} also shows the target pressure). Fourth, switch on the check valve (3) and inject the continuous phase (water) at a constant flow rate (10 ~ 20 $\mu\text{l}/\text{min}$ in this study) into the microfluidic system. Finally, raise the CO₂ injection pressure to create a fixed pressure difference ($P_{ISCO} - P_{trans} \sim 300 - 400$ KPa for all experiments) across the microchannel once the continuous phase enters the T-junction. CO₂ bubbles/droplets in different sizes can be generated at the T-junction depending on the flow rate ratio of the continuous phase and CO₂.

2.5 Image analysis

We develop a method to extract the data of a single CO₂ bubble/droplet, including displacement and length, as it moves along the microchannel using ImageJ [181]. First, we set the main channel's center point right above the central T-junction as the microchannel origin, $P(t=0) = (x_0, y_0)$. The second step is setting a threshold value to binarize the grayscale images. The binary image can help identify the coordinates of two edges of a bubble/droplet, $P_f(t)$ and $P_r(t)$. Fig. 2.7 (a) and (b) are

the representative snapshots showing the image before and after the thresholding process.

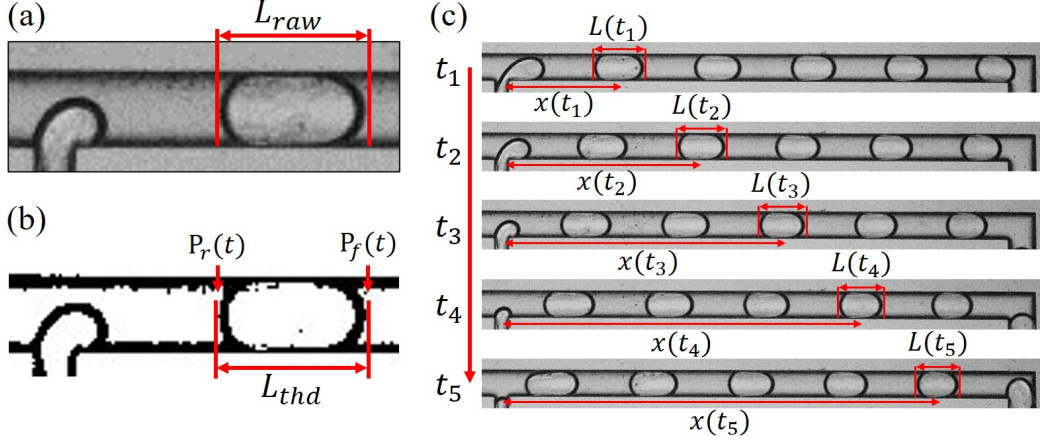


Figure 2.7. Snapshots of experiment data for demonstrating the image processing steps. (a) The raw sample image before processing. (b) The binarized image after enhancing the sharpness of interface and thresholding. (c) The image sequence shows the idea of tracing a moving object along the microchannel using functions in ImageJ.

As one approach, subsequently we follow a bubble/droplet to measure the coordinates of two edges changing with time t . The length of a bubble/droplet is the difference between the two edges, $L(t) = P_f(t) - P_r(t)$. The mean of $P_f(t)$ and $P_r(t)$ expresses the center coordinate of a bubble/droplet, $x(t) = \frac{1}{2} (P_f(t) + P_r(t))$, as illustrated in Fig. 2.7 (c). As a second approach, the ROI (region of interest) Manager with wand selection tool in ImageJ allows us to estimate the emulsion's length and central location, $x_c(t)$, varying with time. The displacement of a bubble/droplet from the origin can be calculated according to the center coordinate.

After a series of tests, we picked a threshold value that gives the resultant bubble length, L_{thd} , a maximum difference of 3.8% from the manually measured results, L_{raw} . The biggest standard deviation measured from the bubble/droplet length is about 4%, which primarily comes from the elongation when a bubble/droplet passes through corners. The error obtained from bubbles/droplets moving on the straight channel reduces to about 2%. Finally, the consistency of bubbles/droplets formatted in our experiments is evaluated using the method mentioned. We measure at least five individual bubbles/droplets from three different phase states and pressure conditions: the gas state at 1 MPa, the liquid state at 7 MPa, and the supercritical state at 9 MPa and 35 °C. The results show excellent consistency among the generated bubbles/droplets in terms of length, $L(t)$, and displacement, $x(t)$, which gave the maximum error of 3.7% in $L(t)$ and 3.1% in $x(t)$.

Chapter 3

Microfluidic Mass Transfer of CO₂ at Different Phases¹

3.1 Introduction

The technology of CCS in saline aquifers is one of the most promising options to store a large volume of anthropogenic CO₂ captured from major emission sites due to the high potential storage capacity (estimated to be more than the order of 10³ Gt) [81, 182]. Understanding the dissolution and mass transfer of CO₂ in the pore fluid (water or brine) is critical because these processes affect the storage capacity of the early trapping mechanisms (i.e., structural and residual trapping) as well as the long term solubility trapping and mineralization with the host rock [110, 183]. In addition, CO₂ is a sustainable “green” solvent widely utilized in cleaning, drying, and extraction, particularly the supercritical state due to its low viscosity and surface tension with a high diffusivity [184].

Conventional methods of measuring CO₂ dissolution rates and mass transfer include bubble column reactors [185, 186] and stirred vessels [187]. A bubble column consists of a cylindrical vessel with a gas distributor at the bottom. The gas is sparged in the form of bubbles into a liquid phase or a liquid-solid slurry [188, 189]. Stirred vessels usually have similar configurations to bubble columns, but an additional stirrer and motor are equipped to enhance the mixing and increase the interfacial area [190]. However, the drawbacks of these methods include considerable back mixing in the collecting tank, bubble coalescence, and requirement of relatively large operation space and

¹This chapter is based on Ho, TH. M., Yang, J., and Tsai, P. A., “Microfluidic Mass Transfer of CO₂ at Different Phases”, Lab on a Chip (in press), 2021.

fluid volume [185, 187] and, hence, motivate alternative efficient approaches.

Microfluidics has offered emerging and promising platforms for a variety of energy and environmental technologies [191, 20, 21, 23, 22]. To name a few, microfluidics has been beneficially utilized for visualizing the multiphase flow patterns of viscous fingering during the gas-liquid and liquid-liquid displacement in a porous medium [22, 192, 193] as well as measuring mass transfer rates of CO₂ [113, 194, 114, 175] and ozone [195], gas diffusivity in different solvents [196], and CO₂ solubility (under temperature effect [115], under surfactant influence [116] and in different solvents [196, 175]).

Very recently, high-pressure microfluidic platforms have been developed to investigate the behaviors of CO₂ with a background fluid at high pressure and temperature to simulate the conditions of deep saline formations, which typically have the pressure (P) range of 6 MPa < P < 27 MPa, while temperature (T) range of 26 °C < T < 110 °C [197]. For example, the investigations using high-pressure microfluidics have focused on the flow patterns of CO₂ displacing fluid [96, 100], the applications of CO₂ in oil recovery processes [198, 199], physical properties (e.g., density and viscosity) at the supercritical state [200], fast screening the CO₂ phase state in different solvents [201, 202], and the solubility of CO₂ in brine [117].

Nevertheless, microfluidic experimental studies regarding the CO₂ transport rate in water or brine at the $P - T$ condition close to or in the reservoir conditions are relatively limited [118, 119, 203, 120]. Sell *et al.* applied sodium fluorescein tracer to measure the diffusivity of CO₂ in brine (up to 5M) at the pressure ranging from 0.1 to 5 MPa using a PMMA microfluidic cell. They reported that the salinity had a significant impact on the CO₂ diffusivity, while the system pressure seemed to have a minor effect on the measured diffusion coefficient [118]. Yao *et al.* [119] performed microfluidic T-junction experiment and found a gradual increase in the mass transfer coefficient, k_L (from 1.8×10^{-4} to 5.3×10^{-4} m/s) of CO₂ bubbles in water with the rising pressure (from $P = 0.1$ to $P = 3$ MPa). In 2017, Yao *et al.* investigated the influence of elevated pressure on the CO₂ absorption in water and a chemical solvent DEA (diethanolamine) by adjusting P ranging from 0.1 to 4 MPa. They reported a decrease in $k_L a$ with the rising pressure in both physical and chemical absorption processes due to the shrinkage of the interfacial area at high pressure [203]. Qin *et al.* experimentally estimated the mass transfer coefficient k_L to be $1.5 \times 10^{-4} < k_L < 7.5 \times 10^{-4}$ m/s for supercritical CO₂ in water (at $P = 8$ MPa and $T = 313$ K), based on the three-dimensional morphology of a shrinking Taylor bubble in a rectangular channel [204]. Additionally, the results showed that a higher water volume fraction results in a larger k_L , and a faster-moving droplet generally has a higher k_L [120].

In this study, we experimentally investigated the influence of different thermodynamic states on the microfluidic CO₂ mass transfer, which is not fully addressed in the literature, particularly the supercritical state. CO₂ bubble/droplet was generated in a T-junction microchannel under various conditions ranging from the standard state ($P = 0.1$ MPa and $T = 24$ °C) to reservoir conditions ($P = 9.5$ MPa and $T = 35$ °C). The mass transfer rate is characterized by the volumetric mass transfer coefficient, $k_L a$, extracted from the length change of a CO₂ slug when traveling in a meandering microchannel. The influence of pressure on the mass transfer rate was examined. We further investigate other key parameters that may affect the mass transfer rate, such as the capillary number (Ca) and the Reynolds number (Re), and compare with other existing experimental results, which used different hydrodynamic diameters.

3.2 Material and methods

We experimentally generated CO₂ bubbles/droplets in milli-Q water using a T-junction microfluidics [32, 50] and measured the size change of traveling CO₂ to acquire the mass transfer data. Microchannels were fabricated using silicon wafers and bound with a cover glass after applying the deep reactive ion etching (DRIE) technique [205, 206]. Fig.3.1a is an experimental snapshot, illustrating the generation of CO₂ bubbles at the T-junction with injection pressure of 1.45 MPa. The water (illustrated by the blue arrow) directly enters the main microchannel (whose width and depth are 100 μm and 30 μm , respectively) as the continuous phase, while CO₂ is injected via the narrower side-channel (of a width of 50 μm) to form the dispersed phase.

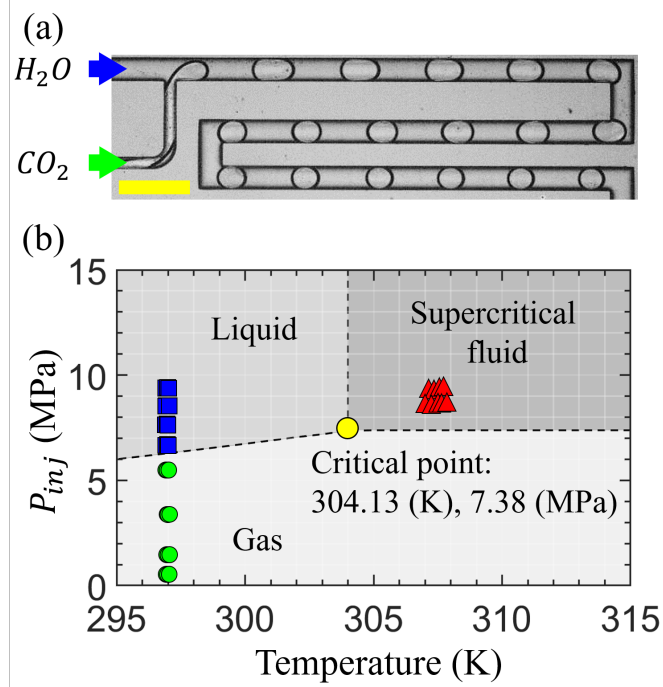


Figure 3.1. (a) The snapshot of CO₂ bubbles generated using a microfluidic T-junction, while subsequently moving in the channel. The water inlet has the same width as the main microchannel of a width of 100 μm , and the CO₂ channel is 50 μm in width. The depth of microchannel is 30 μm . The (yellow) scale bar represents 300 μm . (b) The CO₂ thermodynamic phase diagram near the critical point (yellow ●). Different symbols show our various experimental conditions for the CO₂ injection pressure, P_{inj} , facilitating different CO₂ phases of liquid (■), gas (●), and supercritical (▲). Image of the phase diagram is adapted from the National Institute of Standards and Technology (NIST) [207].

3.2.1 Experimental procedures

The microfluidics was installed in a metal platform that allows operation from the standard atmospheric condition ($P = 0.1$ MPa and $T = 24$ °C) to reservoir conditions ($P = 9.5$ MPa and $T = 35$ °C), covering the gas, liquid, and the supercritical state of CO₂, as shown in Fig. 3.1b. A heating plate and two thermocouples (K-type) were attached to the platform to heat up and monitor the temperature of the assembly, respectively. Milli-Q water was loaded in stainless steel syringes and pumped by a syringe pump (Chemyx Inc. Fusion 6000) after one hour of degassing in a vacuumed chamber. CO₂ was controlled by a high-pressure gas pump (ISCO 100DX), which directly connects with the gas tank (Praxair, RES K CO₂ 99.998 %). A backpressure regulator (TESCOM BP 25-4000PSI) was connected to the system's outlet to keep a proper pressure gradient across the channel. The

flow pattern was observed by using an inverted microscope (Zeiss Axio Observer 7 Materials) and recorded by a high-speed camera (Phantom V710L) at a rate of 5000 frames per second (fps).

3.2.2 Image analysis

We processed the recorded images using ImageJ (NIH Image) [181] to measure the size of a single bubble and track its position varying with time. The measured data were further analyzed by using a customized code written in Matlab (MathWorks®). The data variation was evaluated by calculating the standard deviation of at least five bubbles for each pressure condition. The result showed good consistency in both the bubble size and position. The variance is about 3 % in bubble length and within ≈ 4 % in displacement.

3.2.3 Determining the volumetric mass transfer coefficient

As revealed by the experimental observation, e.g., Fig. 3.1a, CO₂ bubbles slowly dissolve in water, resulting in shrinkage in size, when they move along the microchannel. We hence analyze the change of the CO₂ bubble length, L_b , with time (t) to extract the (liquid-side) volumetric mass transfer coefficient ($k_L a$) as it moves at a speed, u_b , downstream (adjacent to a liquid slug of water a length of L_s) in a microchannel width (d_c), schematically illustrated by Fig. 3.2a.

To estimate $k_L a$, we used the so-called unit cell model [72, 119, 66] by analyzing the mass transfer between one single bubble and its adjacent liquid slug, illustrated by the red dotted-line compartment in Fig. 3.2a. Assume the liquid slug is initially free from CO₂ and in time CO₂ slowly dissolved while well-mixed in the adjacent liquid slug, based on the mass balance concept, the mass transfer of CO₂ from the bulk phase (of bubble) through the phase boundary to the liquid slug can be mathematically described by

$$\dot{M}_{\text{CO}_2} = -\frac{\rho dV_b}{dt} = V_L \frac{dc}{dt}, \quad (3.1)$$

where V_L and V_b are the volumes of the liquid slug and CO₂ bubble/drop, respectively. The CO₂ density, ρ , is assumed to be a constant. The volume of the liquid slug V_L remains unchanged because of the fixed water injection rate ($Q_L = 15 \mu\text{l}/\text{min}$). c denotes the CO₂ concentration in a liquid slug as a function of position (x) and time (t). Here, the unit-cell model also assumes no mass transfer between different unit cells [66, 119].

Eq. (3.1) correlates the CO₂ concentration changes in a fluid element to the decrease in the bubble volume. As CO₂ bubbles/droplets move, fluid elements (in the liquid slug) repeatedly move

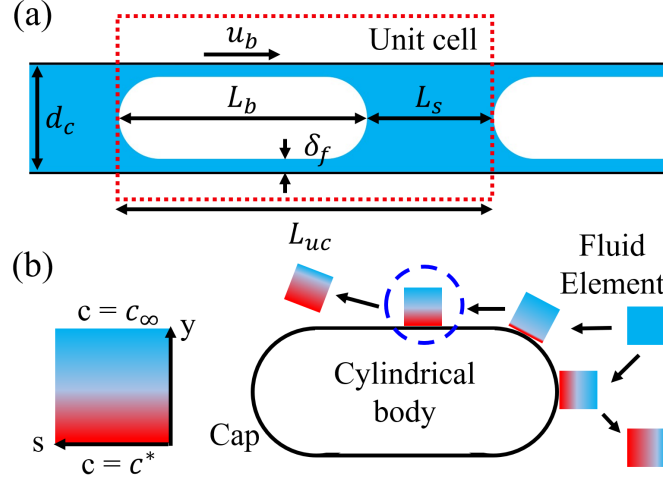


Figure 3.2. The schematic of theoretical conceptual model: (a) A unit cell. The length of a unit cell, L_{uc} , is the sum of L_b and L_s , where L_b and L_s represent the length of the CO₂ bubble/drop and liquid plug, respectively. A bubble is surrounded by the thin liquid film of δ_f in thickness. It travels at the velocity of u_b in the channel with a hydraulic diameter d_c . (b) Higbie's penetration theory [19]: A fluid element from the bulk phase may contact the phase boundary at a finite time. During this period, the mass transfer is assumed only via molecular diffusion. The y -axis denotes the direction of mass transport, and the s -axis represents the streamline direction.

from the bulk fluid phase onto the phase boundary (contacting with CO₂) and stay for a limited time, δt . The process is schematically illustrated by Fig. 3.2b, showing CO₂ concentration variation in liquid bulk and along the phase boundary. The initial concentration of CO₂ in a liquid element equals that in the bulk fluid phase, denoted as $c(x)$, varying with the downstream location (x) as the CO₂ bubble/drop traveling downstream. Due to the direct contact the phase boundary (at $y = 0$) is always saturated with CO₂, whose saturation concentration is denoted as $c^*(P, T)$ as a function of P and T . In short, these boundary conditions at the phase boundary and the liquid bulk can be expressed as $c(y = 0) = c^*$ and $c_\infty \equiv c(y \approx \infty) = c(x)$, respectively.

The mass transfer rate from a CO₂ bubble to the surrounding liquid is the integral of the mass flux through a fluid element over the surface area of the phase boundary around a bubble, A_b :

$$\dot{M}_{CO_2} = \int_{cs} J_{CO_2} dA_b = k_L A_b (c^* - c_\infty). \quad (3.2)$$

The CO₂ mass flux, J_{CO_2} , can be further expressed using the mass transfer coefficient, k_L , which by definition is determined by the ratio of CO₂ mass flux to the concentration gradient.

The rate change of CO₂ concentration in a liquid slug equals the mass transfer of CO₂ through

the phase boundary; We therefore combine Eqs. (3.1) and (3.2):

$$\frac{dc}{dt} = k_L \frac{A_b}{V_L} (c^* - c(x)) = k_L a (c^* - c(x)), \quad (3.3)$$

where a is the specific area and defined by the ratio of A_b to V_L . The prefactor $k_L a$ in Eqn. (3.3) is the volumetric mass transfer coefficient, as an important measure for the CO₂ transport efficiency in a unit cell.

By integrating (3.3) and using the chain rule of total time-derivative, the CO₂ concentration change in a liquid slug can be modeled by:

$$c^* - c(x) = (c^* - c_0) \exp\left(-\frac{k_L a}{j_L} x\right), \quad (3.4)$$

where c_0 is the initial concentration of CO₂ in the water, $c_0 \equiv c_\infty(t=0)$. j_L is the superficial velocity of liquid, that is, $j_L = Q_L/A$, the ratio of liquid injection rate (Q_L) to the cross-sectional area of the microchannel (A).

Eqn. (3.4) describes the concentration difference with an exponentially decay at a rate of $k_L a/j_L$. Substituting Eqn. (3.4) into Eqn. (3.3), the change of bubble size (or length) relates to the concentration change of liquid slugs ($\Delta c = c^* - c_0$) and $k_L a$:

$$\rho \frac{DV_b}{Dt} = \rho A_c u_b \frac{dL_b}{dx} = -k_L a V_L (c^* - c_0) \exp\left(-\frac{k_L a}{j_L} x\right). \quad (3.5)$$

Here, A_c is the cross-sectional area of CO₂ bubble and assumed to be a constant. L_b denotes the bubble length, changing with downstream position, x .

By integrating Eqn. (3.5) and dividing by the initial bubble length (L_{b0}), the dimensionless size (or length) change of a moving (CO₂) bubble with the position away from the origin (T-junction) is described by:

$$\frac{L_{b0} - L_b}{L_{b0}} = \frac{1}{L_{b0}} \frac{j_L V_L}{A_c u_b \rho} (c^* - c_0) \left[1 - \exp\left(-\frac{k_L a}{j_L} x\right)\right]. \quad (3.6)$$

The first term of prefactor determines the maximum size change at the equilibrium state, and the second one ($k_L a/j_L$) determines the speed to reach equilibrium. Eq. (3.6) is used to obtain the $k_L a$ from the size change of bubbles in a microfluidic system without measuring the concentration change in liquid slugs [72, 119]. We extracted $k_L a$ using a best nonlinear fit of Eq. (3.6) with our data measured at elevated CO₂ injection pressures to investigate the influence of pressure on the CO₂ mass transfer, i.e., $k_L a$.

3.3 Results and discussion

3.3.1 CO₂ bubble/droplet size change at different phases

Our experiments were operated from gas ($P_{\text{inj}} = 0.25, 1.45, 3.45, \text{ and } 5.45$ MPa) to liquid ($P_{\text{inj}} = 6.45, 7.5, 8.5, \text{ and } 9.5$ MPa at room temperature) and supercritical ($P_{\text{inj}} = 8.5$ and 9.5 MPa at $35 (\pm 0.5)$ °C) states of CO₂ to reveal the dynamics of CO₂ transfer in water and the influence of pressure. For each injection pressure, we conducted at least three times of experiments independently to check the reproducibility. In total, thirty-four sets of experimental data were summarized and presented in this work. The complete experimental data is shown in Fig. A.1 in Appendix A. Revealed in Fig. 3.3a are representative snapshots (taken from five fixed, downstream locations along the channel), including the T-junction's origin point. The initial length of CO₂ bubbles/droplets (L_{b0}) was controlled within $212 (\pm 7)$ μm , with the length of liquid slugs of $194 (\pm 11)$ μm and the mean CO₂ bubble/droplet speed of $0.33 (\pm 0.07)$ m/s.

Fig. 3.3b and 3.3c show the dimensionless length, $L_b^* = L_b/L_{b0}$, and dimensionless length change, $dL/L_{b0} = 1 - L_b/L_{b0}$, of CO₂ *vs.* the traveling distance recorded from (a), respectively. It is noteworthy that all CO₂ bubbles/droplets experienced a rapid shrinkage when they departed from T-junction and later reached a final steady state. At high-pressure conditions, the size change became subtle. As seen in (b), CO₂ bubbles shrank more than half of its initial length at the low system pressure (e.g., 1.45 MPa depicted by \circ). As the pressure increased, the range of drastic size change became smaller, shown by the data of 5 MPa (depicted by \square). In the liquid (\diamond) and supercritical state (\triangle), the shrinkage of a droplet decreased to about 10 % of its initial length. Meanwhile, these high-pressure CO₂ drops reached the final steady-state size faster than the low-pressure ones. It took 12 ms on average for liquid and supercritical CO₂ droplets to reach a final steady state, whereas the CO₂ bubbles at 1 MPa needed more than 30 ms to reach its stable size.

To examine the above distinct observations, we correlated the dimensionless maximum size change of CO₂ (dL_{max}^*) with the CO₂ density, $\rho(P, T)$, bubble velocity, u_b , and liquid volume, v_{slug} , measured from experiments to investigate their influences on the (quasi-)equilibrium size (see A.2 in Appendix A). The dL_{max}^* was determined using the mean value of the dL^* in the plateau region of Fig. 3.3c. The results showed that CO₂ density has a strong but negative correlation with its size change. The significant difference in size change at the different states likely attributed to the increase in CO₂ density with increasing P , as it transforms from the gas, to liquid, and to SC state. For instance, CO₂ density increases by $\approx 25\times$, rising from $\rho = 28.19$ to 693.95 Kg/m³, when

P increases from $P = 1.45$ MPa to $P = 9.5$ MPa for the same $T = 24$ °C, as shown in Table A.1 in Appendix A. Although the CO₂ solubility in the water, i.e., $c^* - c_0$, also increases with pressure, this solubility increase (by $\approx 3\times$, from 21.86 Kg/m³ at 1.5 MPa [208] to ≈ 67.3 at 9.63 MPa [209]) is smaller than the contribution from the increase in CO₂ density.

The bubble velocity and the liquid volume had only a minor correlation on the size change of gas CO₂ ($P \leq 6.29$ MPa). The influences of these two parameters (for the ranges explored) are negligible when CO₂ phase changed into the liquid and the supercritical CO₂ (as shown in Fig. A.2 in Appendix A).

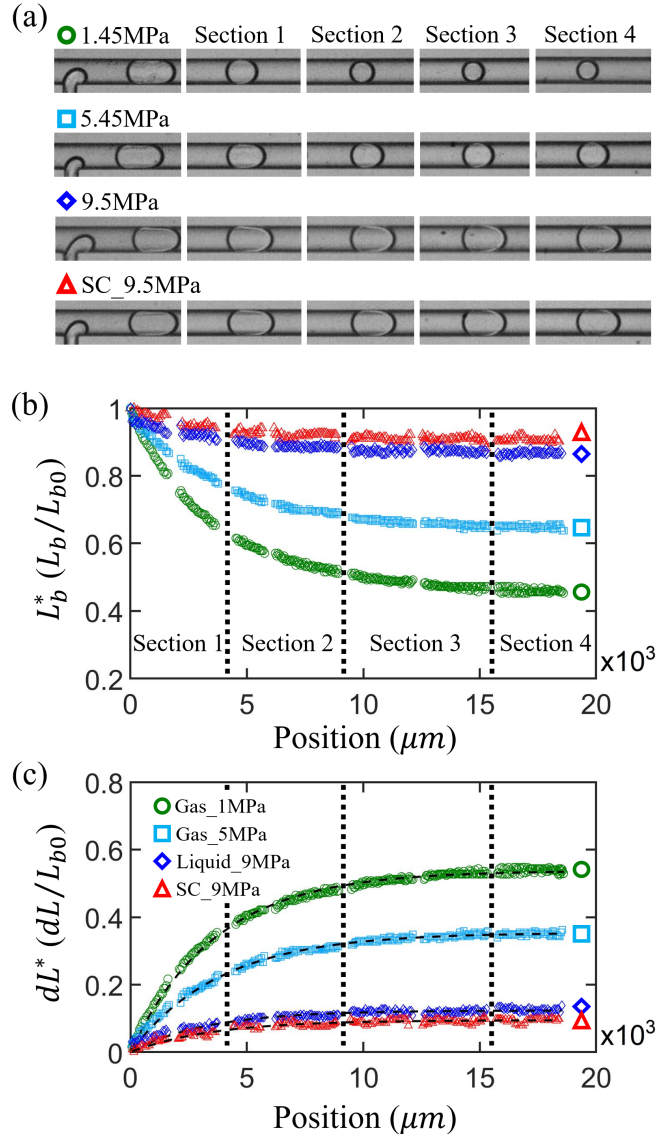


Figure 3.3. (a) Experimental snapshots of CO₂ bubbles or droplets in water in the microchannel for four different injection pressures, covering the CO₂ phase state from gas (\circ and \square) to liquid (\diamond) and supercritical state (\triangle). As a reference of scale, the width of channel is 100 μm . CO₂ bubbles/droplets shown in (a) correspond to different locations: at initial position ($x = 0$), 4,000 μm (section 1), 9,000 μm (section 2), 15,000 μm (section 3), and 18,600 μm (section 4) away from the T-junction. Dimensionless length and length change of the CO₂ bubbles/droplets measured from the image sequences are shown in (b) and (c), respectively. In (c), the comparison of the measured CO₂ length change with the results of nonlinear regression fitting of the simplified form of Eqn. (3.6): $dL^* = \alpha(1 - \exp(-\beta x))$. The volumetric mass transfer coefficient, $k_L a$, is obtained by multiplying the fitting coefficient, $\beta = k_L a / j_L$, by the inlet water flux, j_L .

3.3.2 Volumetric mass transfer coefficient under elevated pressure

We extracted the volumetric mass transfer coefficient, $k_L a$, by applying a nonlinear regression method with a reduced form of Eqn. (3.6): $Y = \alpha(1 - \exp(\beta X))$, to fit the experimental data of dependent variable Y as a function of parameter X , which is the downstream location x from the T-junction. Fig. 3.3c reveals the dimensionless size-change of CO₂ dL^*/L_{b0} at different pressure conditions and the resultant fitting of the nonlinear regression (depicted by the black dashed lines). Overall, Eqn. (3.6) models well our experimental data. At the gas states ($P \leq 6.29$ MPa), The R-squared values were between 0.97 and 0.99. The standard deviation of fitting coefficients was smaller than 1 % for the prefactor α and within 3.2 % for the mass transfer coefficient term β . For the results in the liquid and supercritical CO₂, the uncertainty of α increased to 5 % and 10 – 15 % for the error of β . The larger percentage errors in the latter cases are associated with the experimental resolution (corresponding to $\approx 4\mu\text{m}$ per pixel) and due to relatively smaller change in the CO₂ size in the high- P regime.

The data reveals that the majority of CO₂ transports in the rapid shrinkage stage at initial time, as seen in Section 1 in Fig. 3.3, especially for high-pressure cases. We hence focused on this short period (about 9 ms) to highlight the influence of pressure on CO₂ mass transfer in water. Fig. 3.4 shows the resultant volumetric mass transfer coefficient, $k_L a$, in the rapid shrinkage stage and the data from previous experiments [113, 194, 195, 119, 120], which primarily focused on low pressures. As seen in the figure, $k_L a$ does not change significantly for low injection pressure when P_{inj} is smaller than 8 MPa, with an average $k_L a = 28.85 \text{ s}^{-1}$. When P_{inj} raises to above 8 MPa, $k_L a$ increases to 45.4 s^{-1} on average for the liquid CO₂ and greatly enlarges to a mean value of 100 s^{-1} for the supercritical CO₂. Our data reveal that the average volumetric mass transfer coefficient, $k_L a$, is increased from the gas, liquid, to supercritical state for a comparative CO₂ traveling speed (of $u_b \approx 0.33 \text{ m/s}$) in a microfluidic channel. This significant gain in $k_L a$ for the supercritical state may primarily attribute to the temperature increase, from 24°C (room temperature) to 35°C for a comparable u_b range in our experiments. The rising temperature activates both water and CO₂ molecules and thus enhances the mass transfer processes by increasing CO₂ diffusivity. As a reference, the diffusion coefficient of CO₂ in the water increases from 1.88×10^{-9} to 2.18×10^{-9} (m^2/s) as measured in the temperature at 25 and 35 °C, respectively [210].

Overall, CO₂ droplets in the rapid shrinkage stage gives an average value of $k_L a = 46.4 \text{ (1/s)}$ (black dashed line in Fig. 3.4) in a microfluidic channel of a small hydrodynamic diameter (of $d_h = 46 \mu\text{m}$). This value is greater than those from previous microfluidic data operated at lower pressure

conditions (0.1 – 3 MPa) and room temperature, with their $k_L a$ values ranging between 0.3 and 16 (1/s) [113, 194, 195, 119]. The enhanced $k_L a$ measured in our experiments, by 3× to 150× compared to those from the previous data. Since the range of CO₂ traveling speed, u_b , is comparable between the experiments, the significant increase in $k_L a$ measured in our experiments compared to previous low- P data likely come from the larger specific area (a) created by our micro-channel, elaborated below.

The specific area, a , conventionally defined as the ratio of interfacial area to the volume of the two phases [57]. For a similar total volume of the two phase, a can greatly enhance mass transfer process by increasing the contact area of the multiphase. According to the calculation proposed by Vandu *et al.* [66], the specific area consists of two parts, namely two spherical caps and a cylindrical

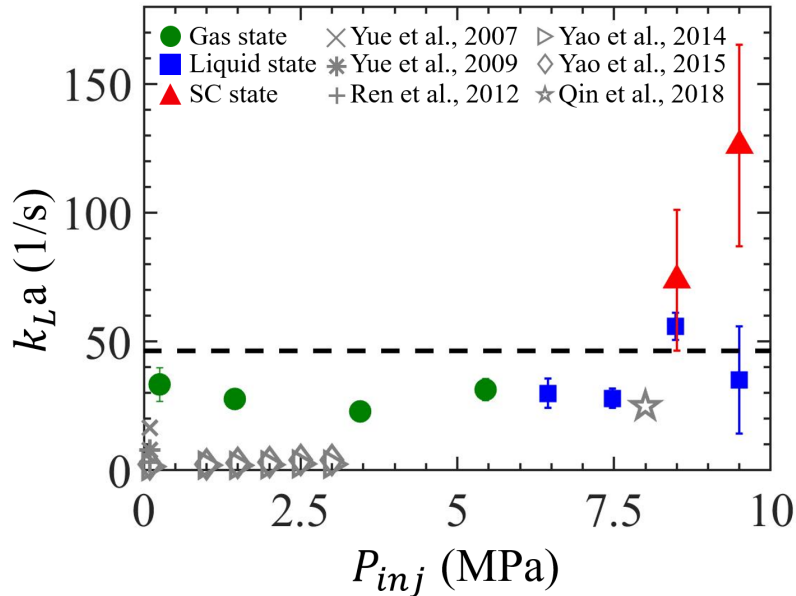


Figure 3.4. The volumetric mass transfer coefficients, $k_L a$, during the rapid shrinkage stage (Section 1) against elevated injection pressures, P_{inj} . Our data span a wide range of P_{inj} , covering three different states, gas (●), liquid (■), and supercritical (▲) of CO₂. The shown points represent the average value of at least three independent experiments repeated for the same experimental conditions. Error bars denote the standard deviations. The black dashed line presents the mean value over all the presenting data, $\langle k_L a \rangle = 46.4$ (s^{-1}). Grey symbols are the maximum $k_L a$ available from previous microfluidic experimental results [113, 194, 195, 119, 120], which mostly focused on low range of P_{inj} and used a microchannel of a size greater than 100 μm .

body of the drop or bubble (i.e., CO₂), as follows:

$$a = a_{cap} + a_{body} \approx \frac{4}{L_s} + \frac{4(L_b - d_c)}{d_c L_s}. \quad (3.7)$$

The specific area hence is inversely related to the microfluidic hydraulic diameter, d_c .

Most of microfluidic experiments studying the mass transfer rates for the segmented gas-liquid flow applied the hydraulic diameters larger than 200 μm , which could generate bubbles with the specific area (a), calculated based Eq. (3.7), ranging from 3,400 to 10^4 m^{-1} [113, 194, 195, 119]. As a comparison, our microchannel has a low hydraulic diameter of 46 μm , which significantly enlarges the specific area of CO₂ bubbles/droplets up to 10^5 m^{-1} on average, approximately 10 \times to 30 \times greater than those of previous microfluidic experiments [113, 194, 195, 119]. In addition, recent high-pressure microfluidic experiment (with $P_{inj} = 8 \text{ MPa}$ and $T \approx 313 \text{ K}$) done by Qin *et al.* [120] found mass transfer coefficient, k_L , to be between 1.5×10^{-4} and $7.5 \times 10^{-4} \text{ m/s}$, consistent with the low-pressure regime data [113, 194, 195, 119]. With a large specific area of 33,200 m^{-1} , this high-pressure microfluidic data also yields a large $k_L a$ up to 24.9 (s^{-1}) (depicted by *) [120], consistent with our microfluidic data at comparable pressure range. In short, these comparisons reveal that smaller microfluidic channel enlarges volumetric mass transfer coefficient significantly by increasing specific interfacial area, thereby benefiting various chemical reactions using a smaller h_d .

Furthermore, the mass transfer coefficient, k_L , at room temperature in this work is estimated $3.4 (\pm 0.71) \times 10^{-4} \text{ m/s}$ on average. This result is consistent with the k_L reported in previous micro-scale experiments ($1.8 \times 10^{-4} \leq k_L \leq 7.3 \times 10^{-4} \text{ m/s}$) [113, 194, 195, 119]. For supercritical CO₂, the k_L is calculated as high as $9.96 \times 10^{-4} \text{ m/s}$ on average, which is about three times larger than the values estimated in the gas and liquid state. The higher $K_L a$ value of supercritical CO₂ compared to the liquid/gas counterpart may be attributed to the greater temperature (35 $^\circ\text{C}$) and a shorter contact time of a fluid element on the CO₂-water interface. The latter is suggested by the Higbie's penetration theory [19], where the mass transfer coefficient is modeled to be proportional to the square root of diffusivity:

$$k_L \sim \sqrt{\frac{D}{\pi \tau_c}}, \quad (3.8)$$

where D is the diffusivity and τ_c denotes the contact time of a fluid element on the CO₂-water interface. D generally has a linear correlation to temperature, reported by previous experimental [211, 210, 212] and simulation works [213].

3.3.3 CO₂ mass transfer rate

We further investigate the influence of the Capillary number (Ca) and Reynolds number (Re) of the injecting water on $k_L a$ (see Fig. 3.5). Here, $Ca = \mu_l \cdot u_b / \sigma$, representing the ratio of viscous drag of the carrier liquid (i.e., water) to the interfacial tension between CO₂ and water, σ . $Re = \rho_l u_b d_c / \mu_l$ is calculated by comparing the inertial force of a moving bubble to the liquid's viscous force, where ρ_l is the liquid density, u_b is CO₂ traveling speed, and d_c is the hydrodynamic diameter of the microfluidic channel. The values of these thermodynamic parameters used are given in Table A.2 and A.3 in Appendix A.

On the one hand, as shown in Fig. 3.5a, the volumetric mass transfer coefficient does not significantly correlate with the Capillary number, Ca , ranging from 1.9×10^{-3} to 1.4×10^{-2} in this study. The change in Ca primarily stems from the decrease in the CO₂-water surface tension (σ) as CO₂ phase changed from gas to the supercritical state. On the other hand, we correlated the $k_L a$ with the Reynolds number in Fig. 3.5b, to study the influence of CO₂ velocity. The black dashed line represents the result of linear regression analysis from all the experimental data, showing the $k_L a$ grows linearly with a prefactor of 0.53 (± 0.58) with Re .

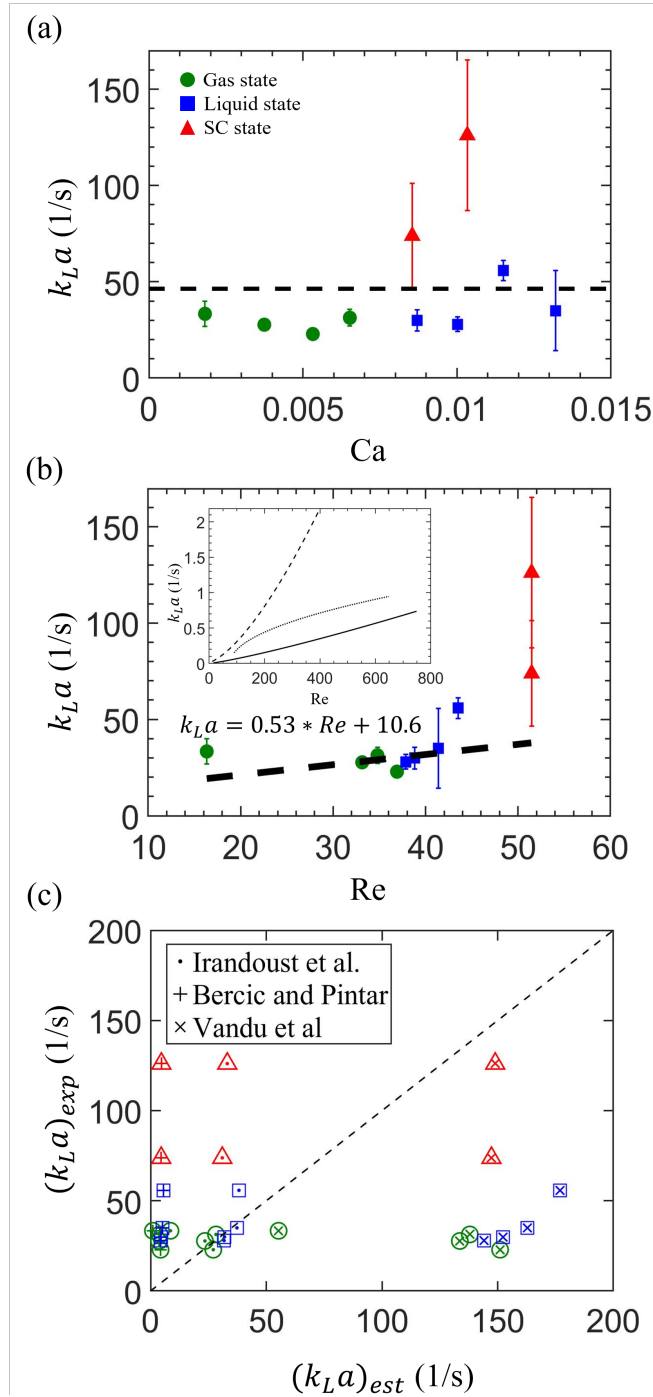


Figure 3.5. The correlation of the measured volumetric mass transfer coefficient, $k_L a$, with (a) the capillary number and (b) the Reynolds number of the continuous liquid phase. (c) The comparison of experimental data from this study, $(k_L a)_{exp}$, and values estimated using the above empirical approximations, $(k_L a)_{est}$, previously proposed by Irandoust et al. (·) [57], Bercic and Pintar (+) [112], and Vandu et al. (×) [66]. Three different colors represent the experimental conditions in three phase states of CO₂: green color denotes the gas state, and blue and red symbols represent the conditions using the liquid and the supercritical CO₂, respectively.

The dependence of $k_L a$ on Re , observed from our data, indicates the significance of CO₂ bubble velocity, u_b , on enhancing the mass transfer. This observation generally agrees with approximations proposed previously, considering the bubble velocity (u_b) as the critical parameter that determines $k_L a$ [57, 112, 66]. Illustrated in Fig. 3.5b inset are the previous empirical approximations of $k_L a$ in millimeter-scale capillaries proposed by Irandoust et al. [57] [dashed line (with $y_m = 0.5$)], Bercic and Pintar [112] (solid line), and Vandu et al. [66] (dotted line). Here, we plot their data as the function of Re based on their experimental conditions. All of the empirical results show a growing $k_L a$ with the increasing Re , i.e., moving speed of bubbles. This dependent relation between $k_L a$ and Re may associate with the fact that a faster u_b enhances the mixing of fluid elements on the phase boundary and the fresh bulk fluid due to the more intensive liquid slug's internal recirculation [61, 71]. Also, from the perspective of Higbie's penetration theory [19], the more intensive internal recirculation implies the more frequent contact of fluid elements with the phase boundary and the shorter contact time for a fluid element on the phase boundary, thereby increasing k_L [based on Eq. (3.8)].

How do our microfluidic results compared with the $k_L a$ obtained using the segmented gas-liquid flow (so-called Taylor flow) in millimeter-sized capillaries [57], which are beneficially used in monolithic chemical catalyst reactors? Fig. 3.5c shows such comparison between our experimental results and the $k_L a$ estimated by three empirical approximations with millimeter-scale capillaries. Our experimental results of $(k_L a)_{\text{exp}}$ are plotted in the Y-axis, whereas the correspondingly estimated values, $(k_L a)_{\text{est}}$, in X-axis, by substituting our experimental conditions into the previous empirical equations, described below.

First, the semi-theoretical model developed by Irandoust *et al.* (depicted by *) considers the bubble speed (u_b) playing a crucial role in the mass transfer on both cap sides and the center cylinder of a Taylor bubble [57]:

$$k_L a = 4[\delta_f(d_c - \delta_f)U_{av} y_m + D Sh(d_c - 2\delta_f)]/(d_c^2 L_{uc}), \quad (3.9)$$

where U_{av} is the mean velocity of the liquid film passing through the cylindrical part of a bubble, which is the function of u_b (Re). Sh denotes the Sherwood number, defined by the ratio of convective to diffusive mass transport [58]. y_m is defined as the mix cup concentration of the solute in the liquid film (contacting the cylindrical part of Taylor bubble) [57] and represents the dimensionless fraction of dissolving gas in the liquid film ($0 < y_m < 1$). The higher y_m implies more solute dissolving in the solvent via the cylindrical part of a bubble. Previous experimental data of $k_L a$ (for $11 < Re < 824$) using millimeter-scale capillaries showed consistent results [57], albeit $\approx 30\%$ lower, compared to

the (semi-)theoretical predictions. Notably, this model performs a good prediction on our results at room temperature if assuming $y_m = 0.052$, as depicted by blue and green symbols. The low y_m implies that the film contribution is small and inactive for mass transfer [see Eq. (3.9)].

Second, results calculated using Bercic and Pintar’s model underestimates the $k_L a$ comparing to our measurements (depicted by +):

$$k_L a = p_1 \times u_b^{p_2} / L_s^{p_3}, \quad (3.10)$$

where $p_1 = 0.111$, $p_2 = 1.19$, and $p_3 = 0.57$ [112], respectively. This empirical model was developed to fit the results measured from experimental conditions of long L_{b0} ($28 \text{ mm} < L_{b0} < 110 \text{ mm}$) and relatively low u_b ($0.076 \text{ m/s} < u_b < 0.15 \text{ m/s}$). In the previous experiments, the long gas bubble and slow velocity make the mass transfer from the cylindrical side of a bubble inactive, i.e., corresponding to the case of $y_m = 0$ in Eqn. (3.9). Therefore, without modeling the contribution from the thin film, this model would underestimate and result in smaller $k_L a$ for our experimental conditions (as shown in Fig. 3.5c).

Third, the empirical model proposed by Vandu *et al.* suggests that the mass transfer happens primarily via the cylindrical body to the liquid film. The contribution from the cap side can be neglected because of the small specific area a of the cap side comparing to the cylindrical body [66]; therefore

$$k_L a = C_1 \sqrt{\frac{DU_g}{L_{uc}}} \frac{1}{d_c} \approx C_1 \frac{\sqrt{Du_b L_{b0}}}{L_{uc} d_c}, \quad (3.11)$$

where the prefactor C_1 is found to be 4.5 to fit their results the best, D is the diffusion coefficient of the solvent, and $U_g = u_b \cdot (L_{b0}/L_{uc})$. This model considering only the film contribution, however, overestimates the $k_L a$ under our experimental conditions (depicted by x). This model corresponds to another extreme condition of Eqn. (3.9) as $y_m \approx 1$, when fluid elements on the cylindrical body remain active.

In brief, our microfluidic measurements of $k_L a$ for the segmented gas-liquid are significantly greater than those obtained by millimeter-size capillaries. Consistently, $k_L a$ generally increases with increasing u_b and, hence, Re . Compared with various empirical models developed for the millimeter-size capillaries, our microfluidic segmented Taylor flow measurements show the contributions of mass transfer from both the spherical caps and the thin liquid film.

3.4 Conclusions

We experimentally investigated microfluidic CO₂ mass transfer rate in water under high-pressure conditions, covering from the normal state on the ground (0.25 MPa and 24 °C) to the deep formation’s reservoir condition (9.5 MPa and 35°C) for the CCS applications. With the pore-scale measurements of the segmented flow’s size-change in a high-pressure microfluidic device, we extracted the liquid-side volumetric mass transfer coefficient $k_L a$ to quantify the dynamic mass transport of CO₂ bubbles/droplets in gas, liquid, and supercritical state. The resultant $k_L a$ reveals a more intensive mass transfer for the supercritical CO₂. The measurement of $k_L a$ also shows a linear dependency on the Reynolds number of the continuous phase with a factor of 0.53. Our microfluidic results with $d_h \approx 50 \mu\text{m}$ show a significant increase of $k_L a$, by $O(1 - 10^2)$ compared to other low-pressure microfluidic measurements (with $d_h \approx 200 \mu\text{m}$) and by $O(10^2 - 10^3)$ compared to those obtained using millimeter-size capillaries.

In terms of CCS applications, our experimental results revealed intensive mass transfer ($k_L a$) of CO₂ in the supercritical state at a pore-scale ($d_h \approx 50 \mu\text{m}$), leading to fast saturation in the water at the early stage and benefiting subsequent sequestration of CO₂. In addition, the increase in the CO₂’s traveling velocity (u_b) considerably enhances its mass transfer. These two primary outcomes can help assess the relevant time-scale and volume of supercritical CO₂’s mass transfer in water for the P–T conditions and fluid inject rates used. Furthermore, the microfluidic platform presented can be extended for beneficial applications of pore-scale visualizations of CO₂-EOR at different reservoir conditions and intensive extractions using the green solvent of supercritical CO₂.

Chapter 4

Multiphase CO₂ Emulsions in Microfluidics: Formation, Phases, and Mass Transfer¹

4.1 Introduction

The technologies of carbon capture, utilization, and sequestration (CCUS) are essential to reduce CO₂ emissions and consequently mitigate global warming issues [214, 215]. CCUS integrates methods to gather and transport CO₂ from large emission sites, such as power plants and oil refineries [216]. The concentrated CO₂ can be utilized for enhanced oil recovery (EOR) [217] and enhanced coalbed methane [218, 219] for energy fuel production while sequestering CO₂, and the further purified CO₂ can be used for chemical synthesis [220, 221]. Alternatively, the captured CO₂ can be stored in various geological formations, such as in ocean [80, 110], in sub-seabeds [222, 223], and in deep saline aquifers for a long time [224].

The CO₂ mass transport behavior, therefore, plays a critical role in many CCUS processes, including the CO₂ absorption in the capture process [216, 23] and the CO₂ dissolution in the pore fluids of sequestration sites. For example, in EOR engineering precise data of CO₂ dissolution in the

¹This chapter is based on Ho, TH. M., Sameoto, D., and Tsai, P. A., “Multiphase CO₂ Emulsions in Microfluidics: Formation, Phases, and Mass Transfer”, submitted to Chemical Engineering Research and Design, 2021.

pore-fluids helps estimate the required injection pressure to reach the minimum miscibility pressure for a better recovery efficiency [217]. The CO₂ dissolution and mass transfer processes affect the storage capacity of deep saline aquifers during the early injection stage (via structural and residual trapping of CO₂ in micropores) as well as the long-term solubility trapping and mineralization of CO₂ with the host, porous rock [225, 224, 110]. Furthermore, understanding the CO₂ mass transport processes helps evaluate the sealing integrity and calculate the pressure build-up and CO₂ leakage [226], which are essential for mitigating potential environmental impacts [222, 227].

The early experimental investigations for measuring the CO₂ dissolution rate and mass transfer include both in-situ field experiments [228, 229, 227, 230] and laboratory measurements using stirred vessels [187] or bubble column reactors [185, 186]. However, the field experiments usually are time- and budget-consuming, and most of the previous laboratory experiments require large apparatuses to handle working fluids at high pressure safely [231, 232, 233] and therefore more space, resources, and experimental time. Hence, it motivates us to explore alternatives for acquiring essential mass transfer data at elevated pressure more efficiently since the relevant experimental studies are crucial but rare currently.

Microfluidics has become an emerging and useful tool for fluid physics [234, 235] as well as energy and environmental technologies due to its time and economic efficiency [191, 20, 21, 22]. A variety of microfluidic platforms have been utilized to investigate the mass transfer rate of gases (e.g., CO₂ [113, 114, 175], air [194], and ozone [195]) in different solvents, the CO₂ take-up capacity of physical solvents for CO₂ capture applications [114, 196, 175], and the influence of temperature [115] and surfactants [116] on CO₂ solubility in water. Moreover, the development of high-pressure microfluidic devices in the last decade enables experiments to operate in a broader pressure (P) and temperature (T) range up to $P = 45$ MPa and $T = 500$ °C [121]. A few of microfluidic studies exploiting high- P platforms provide insights into the CO₂ behaviors in different carbon storage scenarios, including the invasion patterns of CO₂ displacing the pore fluid [96, 100], the applications in the enhanced oil recovery (EOR) [198, 199], the physical properties at the supercritical state [200], fast screening the CO₂ phase state in different solvents [201, 202], and the CO₂ solubility in brine [117].

Microfluidic studies addressing the mass transfer rate of CO₂ in water/brine at high P - T conditions, especially for the liquid and supercritical CO₂, are still limited [118, 119, 203, 204, 120]. Sell et al. [118] reported a minor influence of pressure on the CO₂ diffusion coefficient as P increased from 0.1 to 5 Mpa. In contrast, the salinity significantly hinders CO₂ diffusion process in water, with a decrease in the diffusion coefficient by 60% with increasing salinity (from 0 to 5 M).

Yao et al. studied the pressure effects on the CO₂ mass transfer rate in water by measuring the liquid side volumetric mass transfer coefficient, $k_L a$, under elevated pressure from 0.1 to 3 MPa. They found that $k_L a$ increased with the rising pressure and attributed this to the enlarged cross-sectional area of a CO₂ bubble at high pressure, which increases the CO₂-water contact area and enhances CO₂ mass transfer [119]. Interestingly, they did not observe a significant influence of pressure on the CO₂ absorption in the chemical solvent DEA (diethanolamine) from their later experiments. They attributed to the shrinking interfacial area due to the altering flow patterns and the channel geometry [203].

Qin et al. calculated the mass transfer coefficient (k_L) from the shrinkage of supercritical CO₂ at 8 MPa and 40 °C according to the 3-D morphology of an ideal Taylor bubble in a rectangular channel [204]. Their results showed that k_L rose from 1.5×10^{-4} to 7.5×10^{-4} m/s as the water volume fraction increased from 0.28 to 0.9. Additionally, CO₂ droplets with a faster-moving speed had a high k_L due to the strong inner recirculation in the water slugs, enhancing the mixing of CO₂ and water [120].

In this work, we experimentally investigate the dissolution of liquid CO₂ in water at the injection pressure $P_{inj} = 6.5$ MPa and room temperature, $T = 23.5$ °C. To the best knowledge of ours, we observe intriguing and remarkable multiphase-coexisting CO₂ dispersions at high pressure, for the first time, generated by a two-phase CO₂ flow merging with water at the microfluidic T-junction (see Figure 4.1), while most similar microfluidic studies using two-phase flow have focused on the generation of monodisperse segmented flows and associated fluid dynamics and patterns [236, 237, 238, 239, 240, 241]. To analyze the complex dynamics of the multi-component CO₂ droplets, which involves phase change and dissolution processes, we first differentiate the phase state of CO₂ inside the dispersion by comparing the mass change and the solubility limit in water (for a particular P and T condition). A detailed discussion is provided according to two different phase combinations. Based on these results, we further quantify the mass transfer process by calculating the dissolution rate of CO₂, \dot{M}_{dis} , and calculating the volumetric mass transfer coefficient, $k_L a$. We find that the estimated $k_L a$ decreases rapidly with time, which may attribute to the change of the specific area, CO₂ concentration in the water slug, and the moving speed of dispersions.

4.2 Material and methods

We experimentally observed an intriguing two-phase CO₂ flow with a clear interface in the CO₂ injection channel before the microfluidic T-junction. Consequently, the multiphase coexisting CO₂ dispersions were formed in the T-junction microchannel after merging with Milli-Q water, as shown in Fig. 4.1a. The experiments were operated at the injection pressure, $P_{inj} = 6.5 \pm 0.05$ MPa and the chip temperature, $T_{chip} = 23.5 \pm 0.5$ °C, as pointed by the blue circle (●) in Fig. 4.1b. The microchannel was fabricated using the deep reactive ion etching method (DRIE) [205, 206]. The main channel is 100 μm in width and 30 μm in height. The side-channel for introducing CO₂ is 50 μm in width and has the same height as the main channel.

4.2.1 Experimental

The microfluidics was installed in a metal platform that can sustain high-pressure. CO₂ pressure was ramped up from the atmospheric condition (0.1 MPa and 23.5 °C) to a high-pressure condition for transforming to the liquid state (6.5 MPa and 23.5 °C). This process was controlled by a high-pressure gas pump (ISCO 100DX), which directly connects with the gas tank (Praxair, RES K CO₂ 99.998%). A back-pressure regulator (TESCOM BP 25 – 4000 PSI) was connected to the system’s outlet to control the CO₂ flow rate by regulating a proper pressure gradient across the channel. Milli-Q water was loaded in stainless steel syringes and pumped by a syringe pump (Chemyx Inc. Fusion 6000) after one hour of degassing in a vacuum chamber. Water is injected at the flow rate of 10 $\mu\text{l}/\text{min}$ for the bubbly, intermittent, and annular-1 flow. The water injection rate for the annular-2 flow is lower, at 5 $\mu\text{l}/\text{min}$. A thermocouple (K-type) was attached to the microfluidic chip and to monitor the temperature. The flow was observed by using an inverted microscope (Zeiss Axio Observer 7 Materials, with a 5 \times objective) and recorded by a high-speed camera (Phantom V710L) at 5,000 frames per second (fps).

4.2.2 Image analysis

We applied a series of post-image processing functions in ImageJ (NIH Image) [181] to measure the size of a single dispersion and track its position with respect to time. We first calibrated these data by comparing them with the manually measured results. The maximum difference between them is within 2.3 % in length. The measured data were further analyzed by using a customized code written in MATLAB (MathWorks [®]). The variation between dispersions was evaluated by

calculating the standard deviation of at least five bubbles for each representative flow pattern. The result showed good consistency in the size and position. The variance is about 2.5 % maximum in dispersion's length and within 2.9 % in displacement.

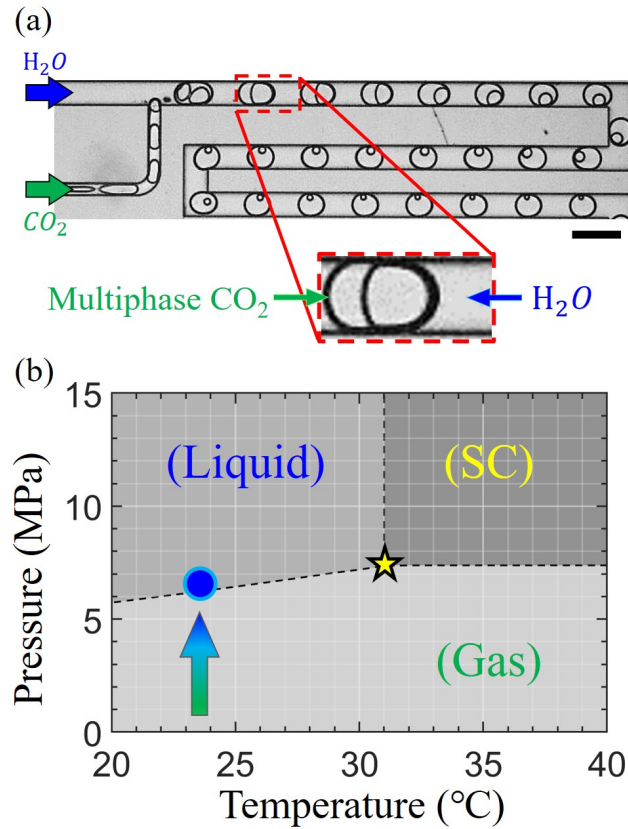


Figure 4.1. (a) An experimental snapshot of dispersions, containing multiphase (gas/liquid) CO_2 surrounded by the continuous phase of water, generated with a microfluidic T-junction. The scale bar represents $200 \mu m$. (b) Plotted in the CO_2 phase diagram are the experimental pressure and temperature conditions (shown by ●) where the coexisting multiphase dispersions are observed. Experimentally, the pressure of CO_2 was gradually increased to ≈ 6.5 MPa (●) at room temperature, as the arrow indicates. The CO_2 saturation pressure at $23.5^{\circ}C$ is 6.14 MPa, as the black dashed line shows the gas-liquid phase boundary of CO_2 . The phase diagram is plotted based on the database provided by the National Institute of Standards and Technology (NIST) [207].

4.2.3 Estimations of the total volume and surface area of a CO₂ dispersion

From our experimental images we notice that a dispersion comprises a brighter area surrounded by the back contour, as shown in Fig. 4.2a. We consider this black contour line resulting from the curved CO₂-water interface, which deflects the light and reduces the interface's brightness. The width of the black contour is measured to be about 8 μm . Therefore, we assume the geometry of a CO₂ dispersion is a planar disk, with two spherical caps on both ends (see Fig. 4.2b). The red area represents the curved CO₂-water interface. Fig. 4.2c and 4.2d show the schematic shape of the CO₂ dispersion from the top view and the side view, respectively. The volume of a dispersion, V_T , is the sum of the center planar part and the two-sided caps:

$$V_T = 2V_{\text{cap}} + V_{\text{body}}. \quad (4.1)$$

The volume of the cap V_{cap} equals the volume of the green fan minus the volume of the triangle OP1P2, from Fig. 4.2c. The volume of the green fan, V_{fan} , and triangle OP1P2, V_{tri} , can be written as:

$$V_{\text{fan}} = \frac{1}{2} \int_{-(\frac{\pi}{2}-\theta_c)}^{\frac{\pi}{2}-\theta_c} A_s R_1 d\theta, \quad (4.2)$$

$$V_{\text{tri}} = \frac{1}{2} (W - 2\delta_f) R_1 \cos\left(\frac{\pi}{2} - \theta_c\right) (H - 2\delta_f), \quad (4.3)$$

where W and H are the width and height of the channel, R_1 is the radius of the circular cap, θ_c represents the contact angle between the (outer) cap and the microchannel (see Fig. 4.2c), and δ_f denotes the thickness of water film between CO₂ dispersion and the sidewall. A_s in Eqn. (4.2) is the cross-sectional area of the green fan through the A-A plane, as the gray area in Fig. 4.2d. The dimensions of A_s can be seen in Fig. 4.2e; note that the dimensions presented are exaggerated for better demonstration. A_S can be expressed as:

$$A_S = (R_1 - C)(H - 2\delta_f) + \beta r^2 - \frac{1}{2} r \cos \beta (H - 2\delta_f), \quad (4.4)$$

where r is the radius of the circular cap projected from the side view, and β is half of the central angle. We acquired these two parameters according to their geometrical relations:

$$r \cos \beta = r - C, \quad (4.5)$$

$$r \sin \beta = \frac{H}{2} - \delta_f. \quad (4.6)$$

The volume of the center body of a CO₂ dispersion is calculated as $V_{\text{body}} = A_c(L_{\text{drop}} - 2L_{\text{cap}})$, where $L_{\text{cap}} = R_1 \cos(\frac{\pi}{2} - \theta_c)$ is the length of the circular cap on both ends. A_c denotes the cross-sectional area of the center body through the B-B plane. We assume the center section's cross-sectional area is constant. Fig. 4.2f schematically demonstrates the idealized dimensions of this cross-section. We consider the shaded region of the body section is due to the curvilinear CO₂-water interface. A_c hence can be expressed as:

$$A_c = (W - 2\delta_f)(H - 2\delta_f) - (4 - \pi)(C - \delta_f)^2. \quad (4.7)$$

By substituting Eqn. (4.2), (4.3), and (4.7) into Eqn. (4.1), the volume of CO₂ dispersion is acquired. This calculation result agree well with the 3-D model built using computer-aided design software (PTC Creo), with an estimated, average error of 1.5%.

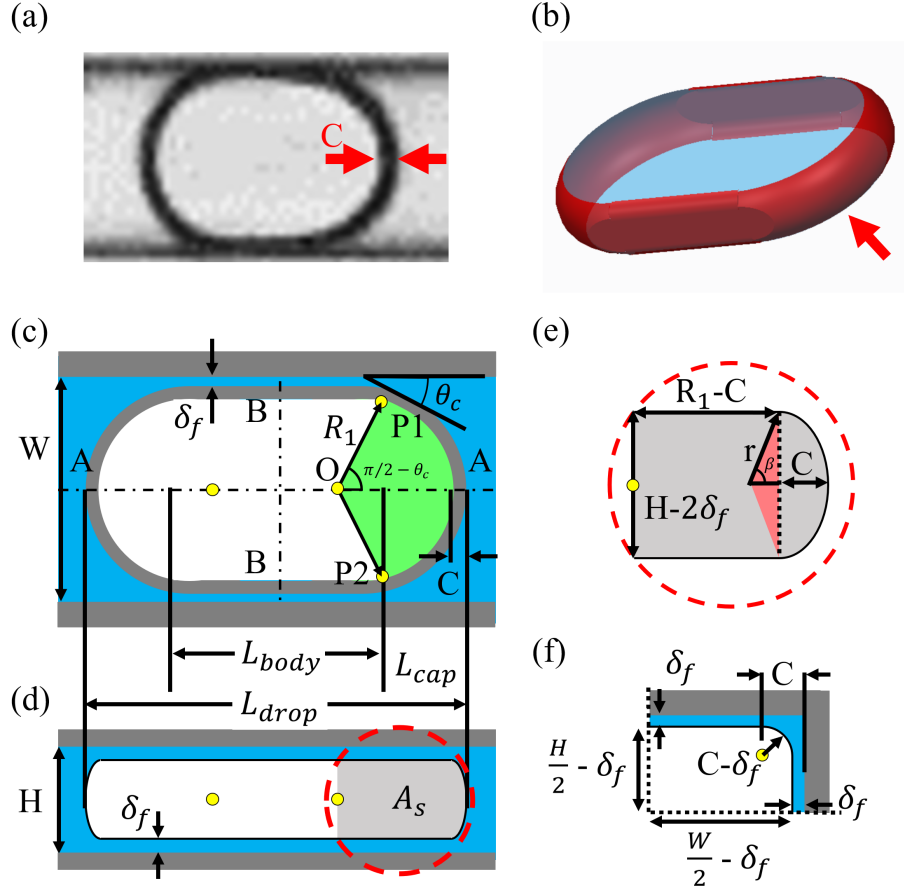


Figure 4.2. The schematic of an idealized microfluidic droplet, whose volume is comprised of a central section and two spherical caps on both ends. (a) Experimental snapshot of a CO_2 droplet. The black contour has a constant width, C ($\approx 8 \mu\text{m}$), for each droplet. (b) Schematic 3D model of CO_2 droplet volume. The red area is the curved CO_2 -water interface, resulting in the shadow area shown in (a). (c) The top view of a droplet with a total length of $L_{\text{drop}} = 2L_{\text{cap}} + L_{\text{body}}$. L_{cap} is the length of the circular caps, and L_{body} denotes the central section of a CO_2 droplet, which is assumed to have a liquid film of a constant thickness, δ_f , between the drop and sidewall. R_1 represents the radius of spherical caps that contact the sidewall with a contact angle, θ_c . C is estimated as the width of the dark area surrounding a droplet shown in (a). Both θ_c and C are measured from experiments. (d) The schematic drawing for the droplet's side-view. A_s denotes the cross-sectional area of the fan region (OP1P2) highlighted in color green in (c). (e) The detailed dimensions of the gray area A_s in (d). (f) The drawing of the quarter cross-section of the center body through the B-B plane.

4.3 Results and discussion

4.3.1 Multiphase CO₂ flow and dispersions

Fig. 4.3a–c are experimental snapshots, showing three distinct CO₂ multiphase flow patterns observed in the CO₂ channel before the T-junction (when $P_{\text{inj}} = 6.51$ and 6.48 MPa, $P_{\text{back}} = 6.15$ MPa and $T_{\text{chip}} \approx 23.5^\circ\text{C}$, close to the CO₂ gas–liquid phase boundary). The multiphase flow quickly transitioned from a segmented flow pattern (Fig. 4.3a) to a parallel flow with an upstream pinch-off nose, emitting segmented flow periodically (Fig. 4.3b). This parallel flow kept propagating along with the CO₂ channel and finally anchored at the T-junction, seen in (c). These three flow modes are similar to the classic condensation flows observed when flowing the vapor state of water [242, 243] or refrigerants [244, 245] in the microchannel as the sidewall temperature (T_w) is lower than the vapor temperature of the fluid. We hence follow the same naming convention, calling the first segmented flow the "Bubbly flow" (Fig. 4.3a), the "Intermittent flow" for the second transitional pattern (in Fig. 4.3b), and the "Annular flow" for the final stratified flow pattern (in Fig. 4.3c). We artificially dyed the central or inner dispersed phase in light green in the images for better visualization.

At the microfluidic T-junction, the multiphase CO₂ flow periodically generates and emits dispersions in the main channel after being sheared off by the water flow. Fig. 4.3d shows such image sequences of the development of CO₂ dispersions for the different CO₂ flow patterns shown in Fig. 4.3a–c. These dispersions are multiphase with a clear interfacial boundary observed between the phases. Although each of the multi-phases is known to be either gas or liquid CO₂ because of the experimental pressure condition, without presumptions each exact phase was not certain and needed to be determined first. From the sequential images in Fig. 4.3 a–c, the inner phase (artificially dyed in light green) prefers to stay on the right side of a CO₂ dispersion, while the outer phase accumulates on the left. For clarification and convenience, we call the phase on the right side of the CO₂ dispersion the "inner (dyed) phase" and the other the "outer (undyed) phase" based on their appearance before the microfluidic T-junction (see Fig. 4.3 a–c).

Fig. 4.3e shows the total length of CO₂ dispersions, L_{drop} , changing with traveling time. The size change of the inner (dyed) phase seems to influence L_{drop} greatly. For dispersions generated by the bubbly flow (depicted by ●) and the intermittent flow (depicted by ■), L_{drop} decreases due to the shrinkage of the inner (dyed) phase. L_{drop} reaches the steady-state when the inner phase completely vanishes. In general, we observe the same behavior for most dispersions generated by the annular flow, as depicted by ◆ in Fig. 4.3d. However, we surprisingly observed a different size

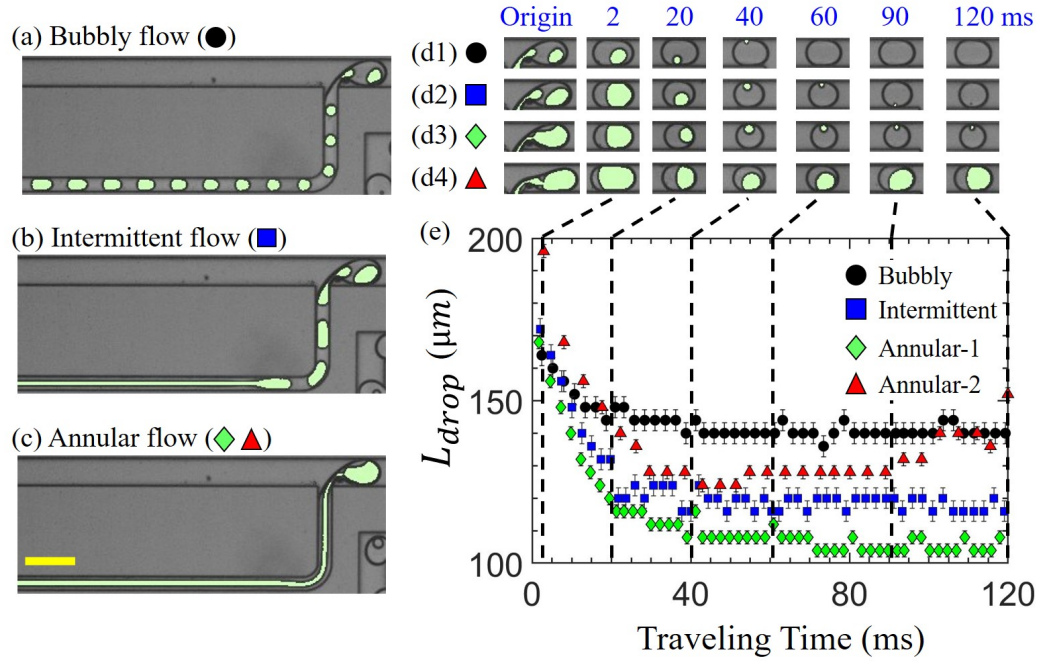


Figure 4.3. The snapshots of three different CO₂ flow patterns in our experiments: (a) the bubbly flow, (b) the intermittent flow, and (c) the annular flow. In the CO₂ channel, the inner part of CO₂ is highlighted in color light green. The yellow scale bar denotes 200 μm. (d) Representative image sequences of gas-liquid coexisting CO₂ dispersions in water of the bubbly flow in (d1), the intermittent flow in (d2), and two annular flow cases in (d3)-(d4). (e) the total length, L_{drop} , of dispersions changes with time in the main channel after the microfluidic T-junction. Notably, we observed two different phase change modes in the CO₂ annular flow pattern. The first one is named Annular-1 (depicted by ◇), and the second one is called Annular-2 (depicted by ▲), respectively.

change behavior of inner (dyed) phase in some dispersions generated by the annular CO₂ flow. As shown in Fig. 4.3 (d4), the inner phase shrank at the beginning when the dispersion detached from the T-junction. However, it started to expand after the dispersion traveled around 60 ms in the main channel, leading to the growth of CO₂ dispersions after moving 55 mm away from the T-junction (depicted by ▲).

4.3.2 Determination of the phase states of a multiphase CO₂ dispersion

Before detailed analyses on CO₂ flow and dissolution dynamics, we have to first differentiate and analyze the exact phases in the multiphase CO₂ droplets/bubbles without any presumptions. Based on the experimental condition ($P_{\text{inj}} = 6.5$ MPa and $T_{\text{chip}} \approx 23.5$ °C), we knew the coexistence of

liquid and gas CO₂ in a dispersion before the T-junction. However, it is challenging to identify the phase states from the experimental grayscale images directly. These phases' grayscale values were close, measured to be 133.7 (± 5.8) and 132.3 (± 6.3) for the inner (dyed) and outer (undyed) phases, respectively. In addition, the surface tension at the water-gas CO₂ interface ($\sigma_{W-G} = 31.7$ mN/m) is very close to that at the water-liquid CO₂ ($\sigma_{W-L} = 30.8$ mN/m) [246]. This implies that both gas and liquid CO₂ could affix to the water and wrap the other phase. Here, we discuss the processes determining the phase state of CO₂ dispersions in more detail by analyzing the volume change, density difference, mass loss, and solubility in water.

Fig. 4.4a demonstrates the total volume of CO₂ dispersions, V_T , changing with time, while 4.4b and 4.4c show the volume fraction of the inner (dyed) phase (V_{in}) and of outer (undyed) phase (V_{out}), respectively. From the observations, V_{in} initially decreases dramatically for all representative cases, while V_{out} increases in the range of 25% – 30% of the change of V_{in} , implying the mass exchange between two phases inside a CO₂ dispersion. Dispersions with a larger initial V_{out} result in a bigger final size in the steady-state (flat regime), as seen in the bubbly flow (depicted by ●), comparing to other cases with larger V_{in} (depicted by ■, ◆, and ▲).

To systematically determine each exact phase (gas or liquid) for the multiphase CO₂, we furthermore consider two different phase combinations and look into their corresponding mass change with time. By comparing with the CO₂ solubility data at 6.5 MPa and 23.5 °C, this data would help differentiate the phase state in a CO₂ dispersion. The first presumption considers that the inner (dyed) phase is liquid CO₂ and the outer gas. The second presumption is the other way, assuming that the inner (dyed) phase is gas and the outer liquid.

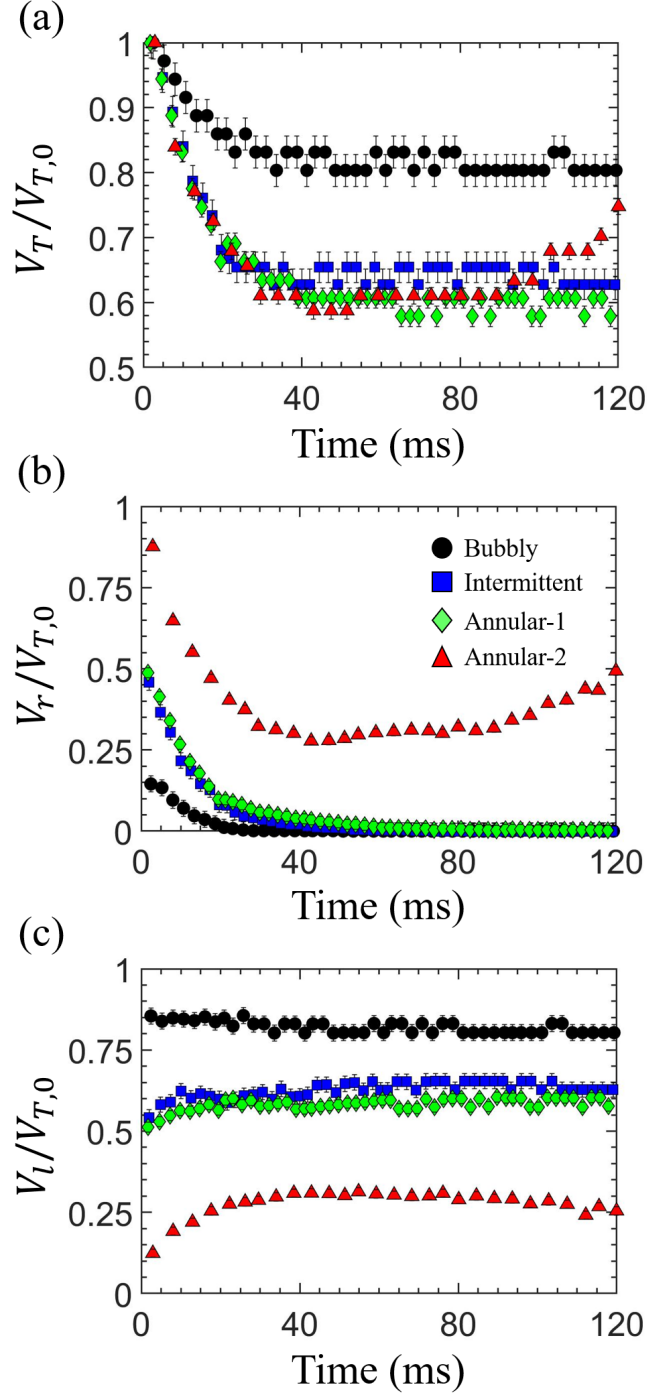


Figure 4.4. (a) The dimensionless volume of CO_2 dispersions changes with time, where V_T is estimated according to Eq.(4.1)-(4.7) and $V_{T,0}$ denotes the initial volume of a dispersion, i.e., $V_T(t = 0)$. The corresponding volume change of phase right and phase left inside the dispersion is presented in (b) and (c), respectively. Dispersions generated by the three distinct CO_2 flow patterns are shown, including the bubbly flow (●), the intermittent flow (■), and the two different CO_2 phase change behavior observed in the annular flow [annular-1 (◆) and annular-2 (▲)].

Fig. 4.5 shows the calculation results according to the two presumptions by showing the total cumulative mass, M_T , the net mass change, ΔM_T , and the estimated CO₂ concentration in water slugs, $|\Delta M_T|/V_{slug}$. Under the first presumption (assuming the inner (dyed) phase is liquid CO₂), M_T dramatically decreases in the first 20 ms and reaches the steady-state for dispersions of the bubbly, intermittent, and annular-1 flow, as shown in Fig. 4.5a. The net mass change, ΔM_T , during this period is between -5×10^{-11} to -20×10^{-11} kg, shown in Fig. 4.5b. Notably, dispersions in Annular-2 (\blacktriangle) show a gradual gain of the mass after 40 ms of traveling time, which is different from the previous three cases. Here, we consider that the mass transfer in a CO₂ dispersion includes two processes: (1) the phase transition between the two phases and (2) the dissolution of CO₂ into the surrounding water. The phase change processes should follow mass conservation, resulting in zero (or negligible) mass change (see Appendix A for a detailed analysis). Therefore, the net mass change, ΔM_T , should always be negative due to the dissolution.

We further estimate the CO₂ concentration in the water changing with time by dividing the absolute value of ΔM by the volume of the adjacent water slug, V_{slug} . Fig. 4.5c shows that the estimated CO₂ concentration for all representative cases under presumption one is above 100 kg/m³, much higher than the CO₂ solubility in water, $S = 61$ (kg/m³), at the experimental conditions of $P_{inj} = 6.5$ MPa and $T_{chip} = 23.5$ °C [247]. Fig. 4.5d–f reveal the analyzed M_T , ΔM_T , and the estimated CO₂ concentration changing with time under the second presumption, respectively. The total cumulative mass of CO₂ dispersions decreases in a range of $1 \times 10^{-11} \sim 3 \times 10^{-11}$ kg, smaller than the results from the first presumption. All representative cases experienced an initial mass loss and reached steady-state at about 40 ms of traveling time. It should be noted that presumption two does not result in the strange mass gain in Annular-2 (depicted by \blacktriangle) in (d). Also, the net mass loss, $\Delta M_T = M_T - M_T(t = 0)$, is between -1×10^{-11} to -3×10^{-11} kg, giving the estimated CO₂ concentration in a range between 13.8 and 69.7 kg/m³. This range is consistent with the CO₂ solubility data in the literature, $S = 61$ (kg/m³) [247].

The above analyses show that the second presumption yields consistent results with the CO₂ solubility data given P and T . Therefore, we confirm that the inner (dyed) phase is CO₂ gas state, and the outer phase is the liquid state. This conclusion is further validated due to the following two reasons. First, the volume change ratio of the outer to inner phase, V_{out}/V_{in} , is about 0.25–0.3. This value is also close to the density ratio of gas to liquid CO₂, $\rho_g/\rho_l = 0.33$, suggesting the shrinkage of the inner (dyed) phase in a CO₂ dispersion is the process combining the phase transition from the gas to liquid and the dissolution into the surrounding water. Second, presumption one yields an

unusual increase in the total mass of case Annular-2 (demonstrated in Fig. 4.4a), implying that this assumption is incorrect because there are no other external mass sources. Besides, the presumption one overestimates the amount of dissolving CO₂ in water.

4.3.3 Formation of multiphase CO₂ dispersions

We further look into how the multiphase flow is formed in the CO₂ channel and what happens to such a CO₂ dispersion evolving in the microchannel, as seen in Fig. 4.3. These multiphase patterns are observed when increasing P_{inj} from 1 atm up to 6.5 MPa at room temperature, and CO₂ in the pump started to phase change from the gas to liquid state slowly. Most of CO₂ likely stayed in the gas state as the oversaturated CO₂ vapor.

As CO₂ entered the microfluidics, CO₂ in the gas state flows in the center of the CO₂ channel, while the liquid CO₂ stayed on sidewalls because it is more viscous than the gas state. The formation of three distinct flow patterns observed might be similar to the jetting flow generated using the co-flow [37] and the cross-type microchannel [248]. This kind of flow pattern may occur when the central fluid's velocity (gas CO₂) is greater than the outer one (liquid CO₂). The upstream annular flow may form because the inertia force from CO₂ gas stream stabilizes with the viscous force and surface tension at the gas-liquid interface [37]. At the nose of the central CO₂ stream, gas bubbles detached and became the downstream bubbly flow, which might be triggered by the amplified capillary waves due to the surface tension gradient [249]. The intermittent flow may be the transition between the bubbly and the annular flow. We observed that the intermittent flow emits droplets/bubbles downstream while upstream became an annular flow.

After the CO₂ flow merging with the continuous water phase, the multiphase CO₂ dispersions were formed periodically. The vapor CO₂ in a dispersion (i.e., the dyed inner phase) continued to transform from the gas to the liquid state, resulting in the rapid shrinkage of inner phase when moving in the main channel, as shown in Fig. 4.3d (first three rows). The expansion of dispersion in Annular-2 case (as demonstrated by ▲ in Fig. 4.3d and 4.3e) might due to the lower CO₂ vapor temperature than the microchannel's sidewall temperature. The local pressure along the channel keeps decreasing due to the hydraulic pressure gradient that drives the movement of a CO₂ dispersion [250]. CO₂ vapor temperature drops with the descending pressure, based on the Clausius-Clapeyron relation [251], leading to the $P - T$ condition moving toward the phase boundary (Fig. 4.1b). Once the vapor temperature decreases to the sidewall temperature, CO₂ starts phase change from the liquid to gas state and expands L_{drop} .

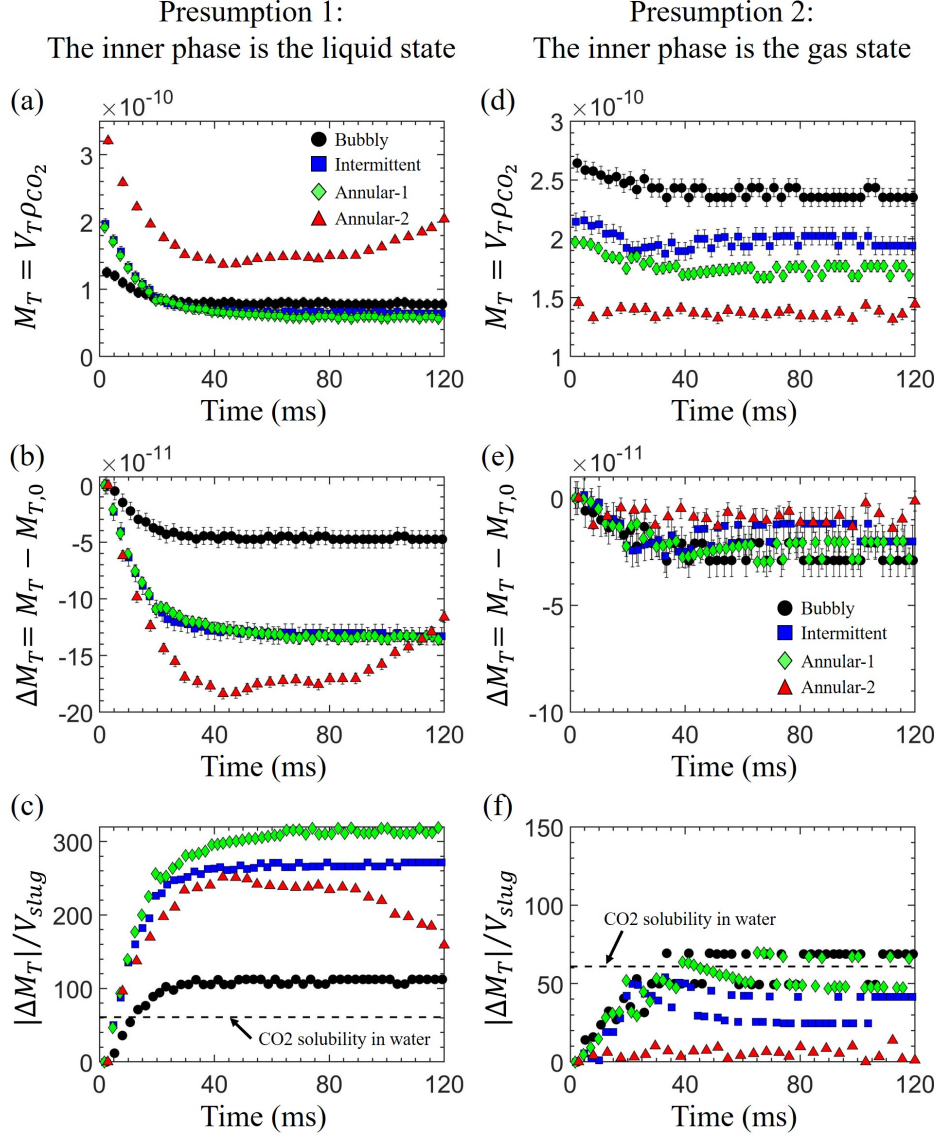


Figure 4.5. Results of time-varying CO₂ mass change estimated according to the presumption 1 and 2. (a) and (b) compare the cumulative mass of a CO₂ dispersion, $M_T = M_{in} + M_{out}$ (kg), changes with time, where M_{in} and M_{out} represent the mass of the inner (dyed) and outer phase of the dispersion, respectively. (c) and (d) show the net mass change of CO₂ dispersions, where $\Delta M_T = M_T - M_T(t = 0)$ (kg). Here, the negative sign of ΔM_T implies the dissolution of CO₂ in the water. (e) and (f) demonstrate the CO₂ concentration change in water, estimated by dividing the absolute value of ΔM_T by the volume of adjacent water slug, V_{slug} (m³). The black dash line denotes the theoretical solubility of CO₂ in water at $P = 6.5$ MPa and $T = 23.5$ °C [247].

4.3.4 Mass transfer of the multiphase CO₂ dispersions

To unravel the dissolution process while phase change is taking place, we develop an analysis to estimate the volumetric mass transfer coefficient, $k_L a$ (1/s), of CO₂ in water according to the dissolution rate of CO₂, \dot{M}_{dis} , and mass conservation. We first assume that the continuous phase, water, is initially free from CO₂. Both gas and liquid CO₂ are incompressible due to the negligible density variation in a small pressure difference (estimated ~ 22 kPa). The CO₂ dissolution rate equals the net mass change rate of a dispersion, which can be expressed to the sum of the liquid and the gas parts:

$$\dot{M}_{\text{dis}} = \frac{dM_T}{dt} = \rho_l \frac{dV_l}{dt} + \rho_g \frac{dV_g}{dt}, \quad (4.8)$$

where ρ_l (ρ_g) is the density of CO₂ in the liquid (gas) state. V_l (V_g) denotes the volume of liquid (gas) CO₂. By integrating Eqn. (4.8), the total mass of dissolving CO₂ is expressed as:

$$\int_0^t \dot{M}_{\text{dis}} dt = \rho_l (V_l - V_{l,0}) + \rho_g (V_g - V_{g,0}), \quad (4.9)$$

where $V_{l,0}$ and $V_{g,0}$ (m³) denotes the volume of liquid and gas CO₂ at $t = 0$, respectively.

The dissolved CO₂ increases its concentration in a water slug, and the convective mass transfer can be expressed as: [119]

$$\dot{M}_{\text{dis}} = -k_L A_T (C^* - C(t)) = -V_{\text{slug}} \frac{dC}{dt}. \quad (4.10)$$

Here, k_L (m/s) denotes the mass transfer coefficient of CO₂ in water. A_T (m²) is the surface area of a dispersion, and V_{slug} is the volume of the adjacent water slug. C^* and $C(t)$ represent the saturation concentration of CO₂ in water and the mean CO₂ concentration in a water slug, respectively.

The CO₂ concentration change in the water slug, $C^* - C(t)$, can be written as an exponential function by integrating the second identity in Eqn. (4.10), so $C^* - C(t) = (C^* - C_0)e^{-k_L a t} = S e^{-k_L a t}$. The dissolved CO₂ in water as a function of time thus can be expressed as:

$$\dot{M}_{\text{dis}} = -k_L a S V_{\text{slug}} e^{-k_L a t}, \quad (4.11)$$

where C_0 is the initial CO₂ concentration in water. Because we assume water is initially free from CO₂, $C^* - C_0$ represents the CO₂ solubility in the water (S) in the unit of kg/m³. $a \equiv A_d/V_{\text{slug}}$; The volumetric mass transfer coefficient, $k_L a$, is associated with the mass change of CO₂ with time via integrating Eqn. (4.9) after substituting \dot{M}_{dis} by Eqn. (4.11):

$$k_L a = -\frac{1}{t} \ln \left\{ 1 + \frac{1}{S V_{\text{slug}}} [\rho_l (V_l(t) - V_{l,0}) + \rho_g (V_g(t) - V_{g,0})] \right\}. \quad (4.12)$$

It should be noted that Eqn. (4.10) and Eqn. (4.11) consider a flat CO₂-water interface for the mass transfer. Studies have shown that the Laplace pressure between the two phases can enhance gas molecules' transport of a stationary gas bubble into the surrounding solvent due to the overpressure. This enhancement becomes significant when the bubble radius is smaller than 15 μm and the solvent is nearly saturated [252, 253]. In our experiments, we degas water for an hour to ensure it is initially free from any dissolving gases, including CO₂. A large concentration difference between CO₂ dispersion and adjacent water would primarily drive the mass transfer of CO₂ [253]. In addition, the Laplace pressure at $P_{\text{inj}} = 6.5 \text{ MPa}$ is estimated to be 1.5 kPa (about 0.023% of P_{inj}). Therefore, the influence of the Laplace pressure or surface curvature on the CO₂ mass transfer is likely negligible in our cases.

Fig. 4.6a shows the semi-log plot of the estimated $k_L a$ for four representative cases by using Eqn. (4.12). All cases show a decreasing trend of $\log(k_L a)$ with a slope of -7.5 ± 2.2 . The black dashed line depicts the linear function as an eye guide. Overall, the average $k_L a$ is estimated to be 25 (1/s), which is consistent with our previous experimental results from injection pressures smaller than 8.5 MPa, giving the value of 29 (1/s) on average (**Chapter 3**). This dynamic change in $k_L a$ was also observed and reported in a recent sub-millimeter scale experimental study of CO₂ mass transfer in water [254].

The decreasing trend of $k_L a$ may attribute to the three following factors. First, the specific area (a) decreases with the reducing length of CO₂ dispersion L_{drop} due to phase change and dissolution, where a is defined by the ratio of the surface area of a CO₂ dispersion (A_T) and the sum of V_T and V_{slug} . Second, the CO₂ concentration across the water-CO₂ interface is initially high as water contacts with CO₂ at $t \approx 0$, leading to the large $k_L a$ because CO₂ molecules dissolve in water in a very short time. The dissolution rate of CO₂ would quickly drop due to the surrounding water gradually saturated with CO₂. Finally, we found that the traveling speed of CO₂, u_e , influences $k_L a$ significantly.

Fig. 4.6b shows that $k_L a$ is the linear function of $\alpha \cdot u_e + \beta$ for all representative cases. The fitting coefficient α shows a larger value of 9150.9 (± 1383.9) for the bubbly (●), intermittent (■), and annular-1 (◆) cases. A smaller α of 1162.9 is found for the annular-2 (▲). The faster u_e allows fluid elements to pass the body part of CO₂ dispersions in a shorter time, preventing the fluid element from saturated with CO₂ and therefore increasing the mass transfer rate. Also, a high u_e induces more intensive inner circulation inside the water slug, enhancing the mixing of dissolving CO₂ in the water [61, 71].

Furthermore, the annular-2 flow shows a smaller estimated $k_L a$ than the other three flow patterns. The data suggest that the pattern of the multiphase CO₂ flow and the water injection rate play a significant role in CO₂ mass transfer. The annular-2 flow is observed at the water injection rate of 5 $\mu\text{l}/\text{min}$, whereas the other cases are generated at a high water injection rate of 10 $\mu\text{l}/\text{min}$. The small water injection implies the weaker shear stress exerting from the continuous water on the dispersed CO₂ phase. As a result, the water phase takes a longer time to rupture the multiphase CO₂ stream and thus generates longer CO₂ dispersions ($177.2 \pm 2 \mu\text{m}$) and water slugs ($216.8 \pm 1.6 \mu\text{m}$). The average length of CO₂ dispersions and water slugs for the bubbly, the intermittent, and the annular-1 flows are $162.9 \pm 4 \mu\text{m}$ and $109.1 \pm 4 \mu\text{m}$, respectively. The long CO₂ dispersion may prohibit the CO₂ mass transfer due to the inactive liquid film surrounding the CO₂ dispersion [57, 70]. In addition, a long water slug may also hinder the mass transfer of CO₂ to water due to the inefficient mixing inside the water slug [112, 255]. As a result, the annular-2 flow shows a small $k_L a$ than the other cases.

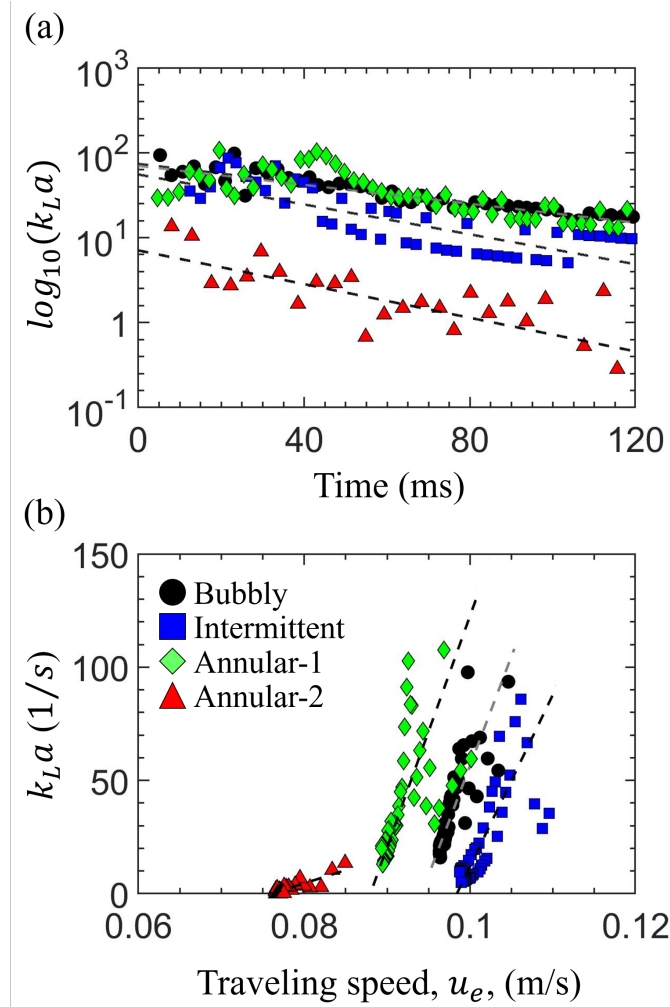


Figure 4.6. (a) The semi-log plot of estimated volumetric mass transfer coefficient, k_{La} , of CO_2 changes with time. The black dashed lines are fitting curves showing the linear relation of $\log_{10}(k_{La})$ to time t . (b) The correlations of the estimated k_{La} and the traveling speed of CO_2 dispersions, u_e . The black dashed line represents the linear function of $k_{La} = \alpha u_e + \beta$. Here, u_e is defined by dividing the displacement from the origin by the traveling time.

4.4 Conclusions

We experimentally investigate an intriguing dissolving dynamics of multiphase CO_2 dispersions in water at the P-T condition close to the gas-liquid phase boundary of CO_2 ($P = 6.5$ MPa and $T = 23.5 \pm 0.5$ °C). The multiphase CO_2 dispersions are generated by merging the gas-liquid CO_2 flow with water using a microfluidic T-junction. Three flow patterns were observed sequentially, from the bubbly flow to the intermittent flow and the annular flow, representing the gaining dominance of the central CO_2 vapor stream over the liquid. A series of strategies are proposed and discussed

to differentiate the phase state of CO₂ inside a dispersion, including estimating the volume of two distinct phases, calculating the corresponding mass change, and evaluating the possible CO₂ concentration change in the water. We find that the gas CO₂ with lower viscosity traveling faster at the center of the CO₂ channel and could be pitched off to form bubbles surrounded by liquid CO₂.

We further estimate the volumetric mass transfer coefficient, $k_L a$, from the multiphase dispersion dissolving into the surrounding water by considering both dissolution and the phase change processes. The estimated $k_L a$ in our experiments ($\approx 25 \text{ s}^{-1}$) is greater than those from previous experimental data (of $0.3 < k_L a < 1.6 \text{ s}^{-1}$) obtained when P between 0.1 and 3 MPa [113, 194, 195, 119]. The larger $K_L a$ value found is likely attribute to the smaller hydraulic diameter used in our design ($d_c \approx 50 \text{ }\mu\text{m}$), giving rise to a larger specific area (a) compared to previous work. Finally, the resultant $k_L a$ of the multiphase CO₂ dispersion shows an exponential decay with time due to decreasing a and, moreover, a significantly linear increase with the CO₂ traveling speed, u_e .

Chapter 5

Microfluidic Salt Precipitation: Implications for Geological CO₂ Storage¹

5.1 Introduction

The carbon capture and sequestration (CCS) technology in deep saline formations is one of the most promising methods to mitigate the anthropological emission of CO₂ due to the ample storage capacity of saline aquifers. [182, 256, 78, 197, 257, 225, 110]. Salt, particularly Halite, precipitation may impede the CCS process and efficiency in deep saline formations, by blocking pore spaces [81] and, in turn, decreasing the permeabilities of the formations. [102, 258, 259, 103] Such alterations and decrease of rock pores can detrimentally affect the injectivity, sealing, and storage capacity of the saline formations for the CCS technology. [258, 259, 103, 104]

To evaluate the influence of salt precipitation during CO₂ injection in the CCS process, the core-flooding method with CT (computed tomography) scans has been often used, by measuring the distributions of salt deposits, the change of pore-size, and the possible impairment of the rock permeability. [260, 261, 262, 263, 264, 265, 266, 267, 268, 269] Two common types of nucleated salt patterns have been observed experimentally: homogeneous and local salt precipitations. On the

¹This chapter is based on the publication Ho, TH. M. and Tsai, P. A. "Microfluidic salt precipitation: implications for geological CO₂ storage." Lab on a Chip. 2020;20(20):3806-14.

one hand, the homogeneous nucleation has a minor effect on the rock formation due to sufficiently-connected pore-space remained after the salt deposits. [267] On the other, local salt precipitation can be a massive salt accumulation at the near-inlet regime of core samples. [265, 266] Some numerical studies have also revealed the dense deposits locally at near-wellbore region, leading to a reduction of the injectivity and a build-up of the injection pressure. [261, 269] More recently, several studies have been carried out to investigate the effects of injection rate, [260, 261, 263, 264] salinity, [261, 263] and temperature [269] on the salt precipitation.

Besides the conventional core-flooding experiments, microfluidics is another useful approach by providing pore-scale observations and insights of salt precipitation at micro/nano-scale. With various microfabrication methods, microfluidics allows direct visualization and quantitative measurements of multiphase flow and dynamics in a well-defined (patterned or random) micro-structures. [270, 105, 21, 106, 107, 109, 108] Recent microfluidic experiments mimicking the CCS process have identified that salt precipitation is composed of two different crystal configurations: bulk crystals and polycrystalline aggregates. Salt aggregates tend to grow around the bulk crystals and extend to a large range. [105] R. Miri et al. proposed a self-enhancing mechanism to explain the poly-crystal aggregation process, in which a liquid film exists and plays a critical role by connecting residual brine pools and drying front. The liquid film delivers salt ions to support the growth of salt aggregates. [106] The significance of water film is also mentioned by A. Rufai and J. Crawshaw, who reported a decrease of permeability in the water-wet channel, whereas no noticeable permeability change in the oil-wet channel. [109] In addition, M. Nooraiepour et al. injected different states of CO₂ (gas, liquid, or supercritical) into a vessel made of organic-rich shale rock that simulates the fractures of caprock. From their measurements, gas CO₂ results in the most extensive salt coverage compared to those for the liquid and the supercritical state of CO₂ injected. [108]

Albeit these previous pioneering investigations of obtaining insights into salt precipitation at the pore scales, due to complex multiphase processes and interactions, quantitative pore-scale measurements of (i) salt distributions varying with brine-drying rate and (ii) the dependence of salt growing rate on the "in-situ" brine drying rate are still missing. To fill the knowledge gaps, in this work, we quantitatively elucidate the pore-scale dynamics of both salt precipitation and de-wetting patterns of brine in a well-defined porous network during continuous gas injection. By applying a series of post-image processes, we extract quantitative data and correlate the brine-evaporation and salt-nucleation rates at the pore-scale. We further analyze the distributions and morphologies of the salt precipitation changing with time and discuss the underlying mechanisms. Finally, we also

investigate the effect of porosity on the dynamics of both brine drying and salt precipitation that mimic the CCS processes in a deep saline formation at pore-scales.

5.2 Materials and Methods

5.2.1 Microfluidics

The microfluidic device consists of an elastomer substrate covered by a thin transparent cover glass for clear visualization (see Fig. 5.1a). We fabricated the substrate using a replica molding method with Polydimethylsiloxane (PDMS) to create a well-defined porous structure [271]. In the replica-molding method, we first designed and fabricated the mold master by applying the standard deep reactive ion etching procedures (DRIE). PDMS elastomer was cast on the mold to form the microstructures and subsequently bonded with a microscope cover-slide for better sealing and observation. Two patterns of different porosity values, $\phi = 0.52$ and $\phi = 0.23$, are designed and used. Regular circular pillars (of the diameter of $d = 550 \mu\text{m}$) are arranged in a body-centered lattice to form the porous pattern for $\phi = 0.52$. The $\phi = 0.23$ pattern is formed by micro-pillars (of the diameter of $d = 460 \mu\text{m}$) in a hexagonal lattice. The pillar height (h) is fixed to be $h = 25 \mu\text{m}$. The details of microfluidic patterns (with images) and replica-molding processes are described in Appendix C.1 and C.2.

5.2.2 Experimental Section

We experimentally investigate the pore-scale dynamics of fluid transport and salt precipitation when air is injected in a porous medium initially saturated with brine. After air displaces brine, water molecules in the residual brine gradually evaporated. Subsequently, salt started to precipitate due to the supersaturation of salt as evaporation goes on. Fig. 5.1 shows representative snapshots of our microfluidic experiment in a porous network, initially fully saturated with brine in (a) and salt crystals precipitated at a later time in the residual brine in (b).

Three initial brine concentrations were used: 16.5% , 21.6%, and 25.6% (in weight fraction of NaCl in 100 ml DI water). Potassium permanganate (KMnO_4 , 1wt%) was added as a purple dye for better visualization and to conveniently and accurately measure the brine drying rate. We also tested the experiments without the additive dye but would need to manually analyze the data of brine-drying and salt-precipitation areas varying in time. We found consistent results of salt

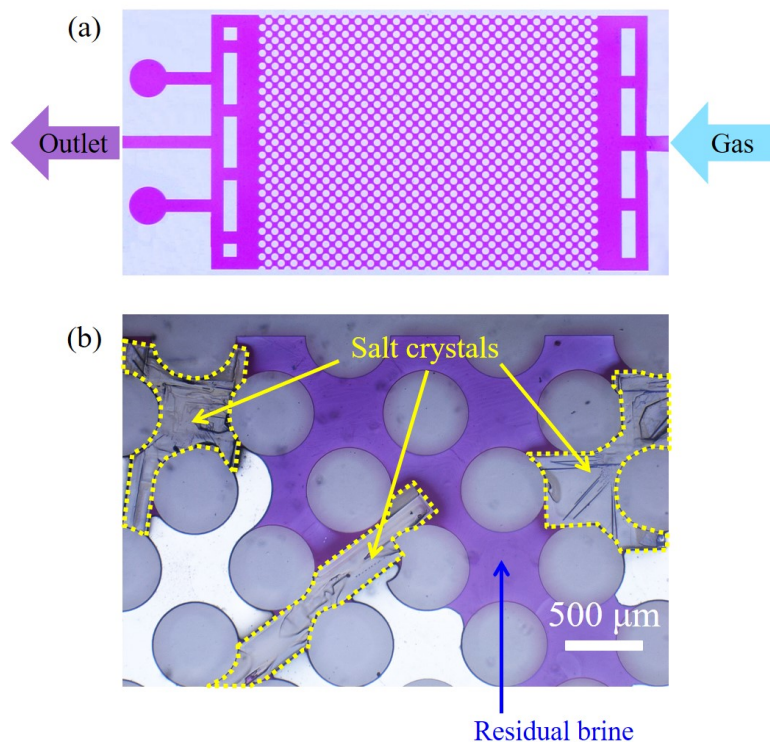


Figure 5.1. Snapshots of our microfluidic experiments: (a) The microfluidic chip is initially saturated with a dyed salt solution. The brine is displaced by air (injected from right to left) at a rate of $500 \text{ } (\mu\text{l}/\text{min})$ at room temperature and 1 atm. (b) Precipitated salt crystals (indicated by the yellow dashed lines) nucleated in a residual brine pool (shown by the mauve color). As gas was continuously injected, salt concentration gradually exceeded the saturation point because of water evaporation, leading to more salt precipitation.

precipitation rates and morphologies of a NaCl solution without and with KMnO_4 , although the latter may contribute to more poly-crystalline and feather-shaped precipitations as well as a maximal error of 5% for the total amount of salt crystallization, which corresponding to a maximal error of $\approx 5 \times 10^{-3}\%$ for the growth-rate (per second). For each concentration, a new microfluidic device was initially placed in a vacuumed chamber to saturate with a brine solution fully. The ambient air (with $\approx 16\%$ relative humidity) was injected by a syringe pump (Chemyx Inc. Fusion 6000) at a constant rate of $500 \text{ } (\mu\text{l}/\text{min})$ at room temperature (22°C), and the microfluidic outlet is open to 1 atm. A digital camera (Canon EOS 70D) was used with a LED backlighting to capture the dynamics of water drying and salt precipitation (at a rate of one frame per 60 secs for 9 hours to record a set of a complete experiment).

5.2.3 Image Analysis

To accurately quantify the brine-drying and salt-nucleation dynamics, we performed a series of post image processes of the captured snapshots to distinguish and analyze the changes of the three phases (e.g., gas, liquid, and solid) involved. As shown in Fig. 5.1b, the solid salt crystal gradually nucleated after the injected air drains the residual brine. Our image analysis can differentiate the time-evolution of the coverage areas (or volumes) of remaining brine and salt nucleation. To precisely identify the boundaries of the porous structure, residual brine, trapped air, and nucleated salts, the recorded image sequences were processed via a color threshold algorithm using ImageJ (NIH Image). [181] For a better result, the CIELAB color space (L^* , a^* , and b^*) was used as the thresholding color space. This color space includes all perceivable colors, which allows us to differentiate the minor color difference between the boundaries of salt crystals and the PDMS substrate. We also minimize the background light deviation between each image by adjusting the desirable range of brightness. [272]

From each series of experimental images recorded, we finally generated two binary image sequences displaying (i) the drying process of residual brine and (ii) nucleation process of salt crystals. By measuring coverage areas of these two binary-image sequences, i.e., $A_B(t)$ and $A_C(t)$ for the brine residual and the salt nucleation areas varying with time (t), respectively, we were able to calculate several relevant time-evolving results accurately. Because our microfluidic porous network has a uniformed height ($h = 25 \mu\text{m}$), the (volumetric) brine drying rate will be $\dot{V}_{brine} = |h \cdot (dA_B/dt)|$. Similarly, by assuming the salt crystallizations occupy the entire channel height, h , the (volumetric) growing rate of the salt precipitation is $\dot{V}_{salt} = h \cdot (dA_C/dt)$. We hence carried out linear fits of $dA_B(t)/dt$ and $dA_C(t)/dt$ to accurately calculate the the drying rate of residual brine and the nucleation growth rate of salt crystals, respectively, for the different drying periods. These are critical for further analyzing the salt precipitation dynamics at the pore-scale. The thresholding setting and image calibration are described in Appendix C.3.

5.3 Results and discussion

5.3.1 Brine Drying and Salt Precipitation

Fig. 5.2 reveals the general dynamics of (i) de-wetting and drying of brine as well as (ii) salt precipitation in the microfluidic porous medium. Shown in Fig. 5.2a are the typical experimental snapshots, revealing the sequential processes of initial brine drainage, subsequent drying, and later-

time salt precipitation, under a constant injection of air. These processes, occurring at different timescales, are revealed by the initial, rapid-drainage of brine (with fast-decreasing purple area in Fig. 5.2a), subsequent slow-change of brine coverage (e.g., at 30%–50% drying time in Fig. 5.2a) and slow salt nucleation (shown by the appearance and accumulation of black spots between 30%–100% of drying time in Fig. 5.2a), respectively. By quantitative image analysis of the time-varying coverage area (e.g., Fig. 5.2a snapshots), we measured the initial brine-drainage, subsequent drying, and final salt-precipitation rates, as shown in Fig. 5.2b, to elucidate the corresponding dynamics and mechanisms at different times.

From inspections of sequential snapshots and quantitative measurement (e.g., 5.2a and b, respectively), we observe three sequential states of brine de-wetting: initially full-saturation, drainage, and drying of residual brine. More specifically, the microfluidic observations generally show that, in the first half-hour of air-injection, the brine solution in the pore structure remained fully-saturated because the gas pressure needs to overcome the capillary pressure when displacing water at the pores. [273] This period corresponds to the initial steady, constant plateau region of normalized residual brine volume, shown by the Fig. 5.2b initial data (\blacktriangledown) between a dimensionless time, $t^* = -0.2$ and 0. Here, the dimensionless time (t^*) is defined as $t^* = (t - t_o)/(t_f - t_o)$, where t_o is the initial time of drainage, and t_f is the complete drying time.

Once the pressure is greater than the capillary pressure, injected air starts to expel brine quickly and, hence, dramatically reduces the brine saturation in the porous network. This drainage state is illustrated by the steep decrease in the volume of residual brine displaced (see Fig. 5.2b data (\blacktriangledown) for $0 < t^* \lesssim 0.1$). After air drains the majority of brine, the residual brine is nearly immobile and trapped in some areas of the pores, forming several pools of residual brine of various sizes. Because the injected air is unsaturated with water vapor (about 16% of relative humidity), water molecules keep evaporating from these brine patches to the surrounding air. The evaporating stage shows three slightly different trends of drying rates, revealed by the blue curve right after the sharp drop of the drainage phase.

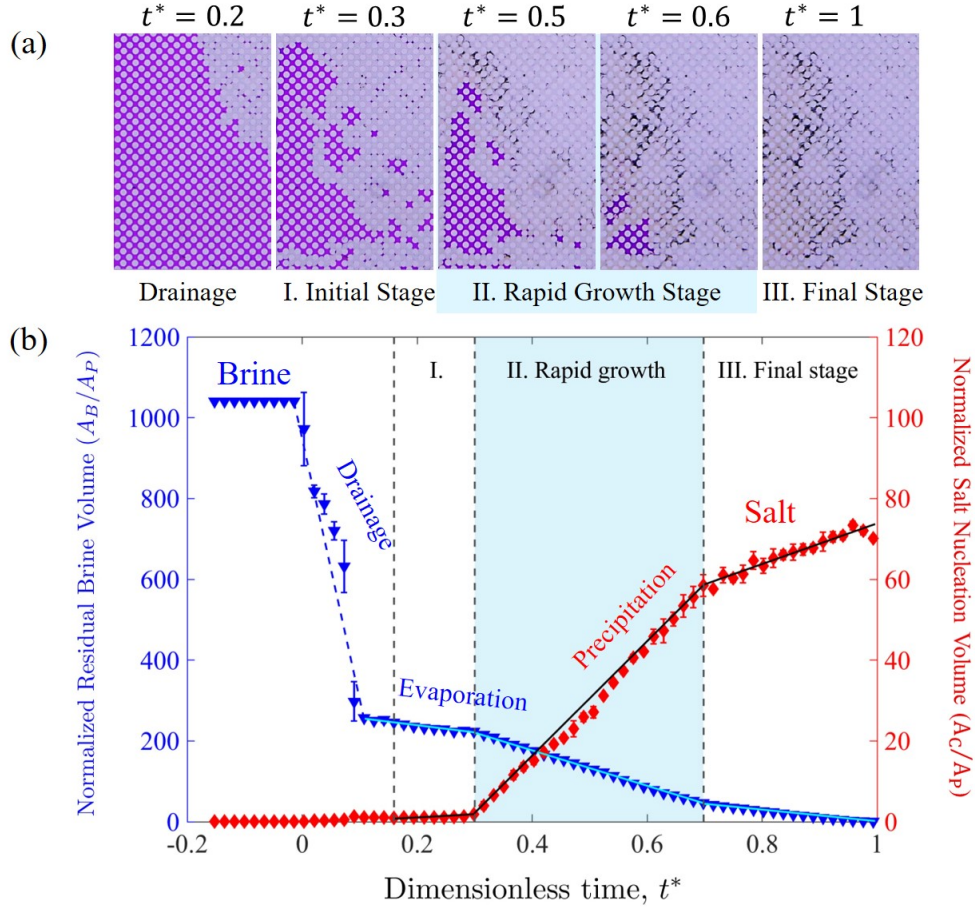


Figure 5.2. Simultaneous dynamics of both brine drainage/drying (\blacktriangledown) and salt nucleation (\blacklozenge) in a well-defined microfluidic network of a constant depth, under a constant air injection (with 16.7% w/w initial salt concentration). (a) Representative experimental snapshots of salt precipitation during a brine drainage. The dimensionless time (t^*) represents a characteristic time with the definition of $t^* = (t - t_o)/(t_f - t_o)$, where t_o is the initial time of drainage, and t_f is the final time when the brine is dried completely ($t_o = 2760$ s and $t_f = 20,040$ s in this case). (b) The changes of residual brine (\blacktriangledown) and salt nucleation (\blacklozenge) volumes in time; here the dimensionless volume is normalized by the unit volume of the regular pore-structure (with a constant depth), i.e., in terms of the numbers of unit-pore. From (b), the development of salt nucleation reveals three distinct phases: (I) initial slow, (II) rapid growth, and (III) final stages characterized by different growth rates measured. Here, A_B represents data of residual brine area varying in time; A_C means the area of salt precipitation; A_P is a constant of a unit pore area we defined ($A_P = 2.51 \times 10^5 \mu\text{m}^2$ in this case; see Fig. C.1 for a detailed A_P).

The dynamics of salt nucleation is simultaneously measured and shown by the increasing area of salt crystals in time, depicted by (◆) in Fig. 5.2(b). The data presented is for the case of 16.7wt% initial salt concentration and $\phi = 0.52$. We observe three phases of salt precipitation and categorized them into: (I) *initial*, (II) *rapid growth*, and (III) *final* stages, based on the different nucleation growth rates observed. We also observed that the faster drying period of residual brine corresponds to a more rapid precipitation of salt. Measurement in Fig. 5.2(b) reveals the salt nucleation at the initial stage (I) grows at a rate of 0.6 (unit pore size/ t^*) while under a slower drying rate of residual brine of 210 (unit pore size/ t^*). Subsequently, the nucleation growth rate at the rapid growth stage (II) accelerates up to 172.8 (unit pore size/ t^*) with the corresponding highest drying rate of 450 (unit pore size/ t^*). At the final stage (III), nucleation growth tends to slow down to a rate of 51.8 (unit pore size/ t^*) as the drying rate of brine decreases to a smaller rate of 170 (unit pore size/ t^*) before completely drying out. We conducted three independent experiments for each salt concentration for the two porosity cases, and in total 18 sets of experimental data were analyzed. For all the concentration and porosity cases, three distinct salt growing regimes as described above are observed, as shown in Fig. C.5 in Appendix C.

To further illustrate the correlation between the nucleation rate and drying rate at different stages, we propose the following possible mechanisms. In the initial phase, the residual brine is confined in the throat (or neck) of pillars by capillary force, i.e., the narrowest gap of pore structure. The evaporation rate, therefore, stays low because of the limiting contact area between gas and liquid. Salt nucleation at this early stage mainly occurs in the small residual brine area (trapped in the throat). Due to this limiting size of the brine area, the coverage of nucleated salt grows slowly.

As water further evaporates, the salt concentration of large brine pools, occupying more than 20 pore units in Fig. 5.2, gradually exceeds the solubility limit to initiate the rapid growth of salt nucleation. This fast process is shown in the second (II) rapid growth region (in the light blue shaded area) in Fig. 5.2b. Two following mechanisms are observed and likely cause this significant increase in the nucleation rate. First, the gas-liquid contact front gradually shifts from the throat towards the region with bigger pore space, which enlarges the gas-liquid contact area and, in turn, accelerates water evaporation and salt nucleation. Second, the small salt deposits, nucleated at the initial stage, can help to speed up the evaporation and nucleation processes at the same time by creating a positive feedback loop discussed below.

The hydrophilic nature of salt crystals can play a crucial role in initiating this feedback loop by attracting the surrounding brine to form a thin film on the crystal surfaces. [103] This affixed brine

film largely increases the gas-liquid contact area and enhances water evaporation. Meanwhile, a new layer of salt crystal nucleates on the original crystal surfaces after water escapes from the brine film, and it extends the coverage of salt precipitation. This newly formed salt creates a more brine-film covered area. It further promotes the positive feedback loop, thereby enhancing further nucleation. Large brine pools adjacent to the drying and nucleation interfaces are the major ions sources in this rapid growth stage. They continuously provide sufficient salt ions to the nucleation region and keep the salt precipitation growing by capillary forces supplying with the ionic current. As a result, the majority of residual brine is consumed and large salt precipitate in this stage.

The final stage of salt nucleation occurs when most of the large brine pools are completely dried, and the majority of salt ions in the system is consumed. The growing rate of salt nucleation thus becomes slower due to the salt concentration in the remaining brine being too low to keep in a supersaturation state, as shown in the final region III in Fig. 5.2b. It hence takes time to regain the supersaturation condition and continues to nucleate the rest of salt ions before the system is completely dried out.

5.3.2 Pore-scale Salt Precipitation

We observed two primary types of salt morphology from the images of final drying patterns under a microscope: large bulk crystals and polycrystalline aggregates. These observations are in agreement with previous microfluidic studies. [105, 106] Large bulk crystals, with transparent and ordered cubic structure, nucleate first via the self-assembly process of salt ions in the liquid phase when the ion concentration exceeds the solubility in certain thermodynamic conditions. [274] After the appearance of bulk crystals, polycrystalline aggregates nucleate on the gas-liquid-solid interfaces and further grow into a group of disordered salt crystals, when a sufficient ion supply is received from the brine sources. [275] The assemblies of bulk crystals and polycrystalline aggregates are revealed in all three nucleation stages, illustrated in Fig. 5.3. For each phase, each row of image sequences demonstrates the evolution of salt nucleation before and after the appearance of the precipitant as well as the zoom-in microscopic images, using 5 \times and 20 \times magnifications.

At the initial stage (I), the majority of salt crystals first appear inside the small brine spot (≈ 1 pore space), trapped within the throat of the pore space. As the shrinkage of small drying brine spots, a few salt crystal branches nucleate and extend from the gas-liquid interface towards the air region to construct the backbone structure for the *polycrystalline* aggregates. Because of the limiting ion supply from these brine spots, these backbone structures stop growing and deposit in the form of tiny salt debris, as shown in the image sequence in Fig. 5.3a.

During the rapid growth stage (II), large brine pools provide sufficient salt ions to assemble bigger bulk crystals. Thus, the poly-crystalline backbones further developed to create the dendritic (or feather-liked) frameworks inside the pore area, as shown in Fig. 5.3b. The dendritic structure helps to increase the contact area between the air and brine by forming a thin brine film via a capillary effect. The brine film can further transport ions from other brine patches. With more salt ions participate in constructing the poly-crystal, dendritic salts start to connect and merge. They generate a much larger and more complicated salt aggregate, which gradually fills the pore space, as shown in the 20 \times magnification of image sequence Fig. 5.3b. This self-enhancing process can, therefore, precipitate a large salt crystal assembly, also shown in Fig. 5.4a, in the pores before completely drying out.

In the final stage (III), salt ions in the rest of brine pools continue migrating to the vast precipitation region and nucleating on the surface of salt aggregates because of the strong capillary induced flow. The hydrophilic nature of salt crystals also helps to keep these delivered ions on the crystal surface. It makes the whole aggregate structure more complicated, as shown in the 20 \times

magnification of image sequence Fig. 5.3c.

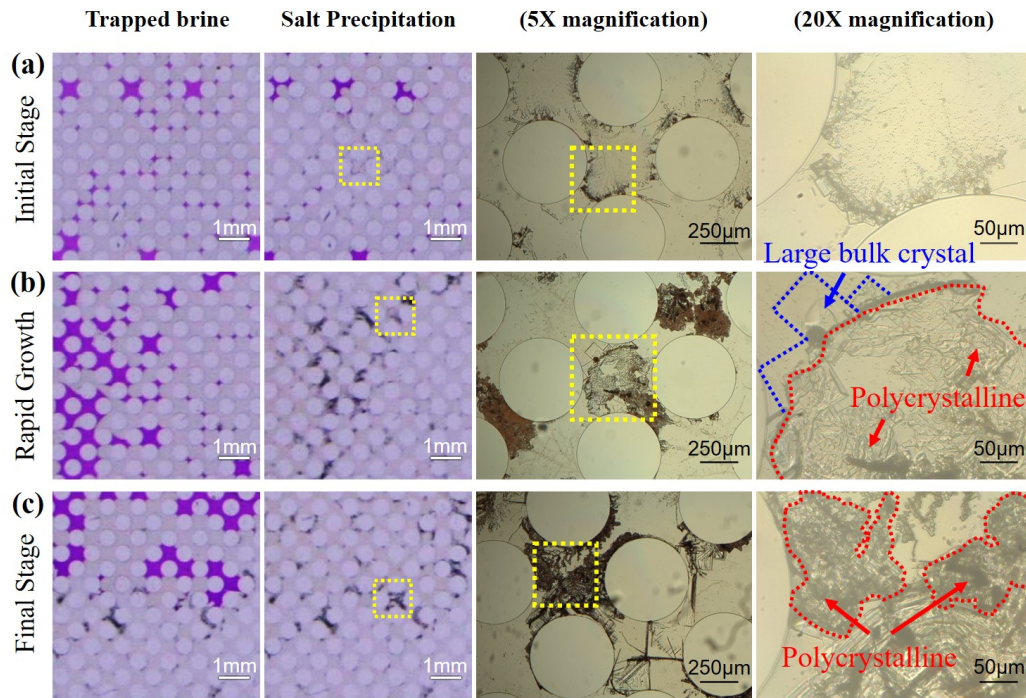


Figure 5.3. Morphologies and patterns of the salt nucleation at the different nucleation stages. Each row of image sequence reveals the development of salt nucleation with the initial residual brine area, subsequent salt precipitation patterns, and magnified salt morphologies under 5× and 20× magnifications at different nucleation stages: (a) initial stage, (b) rapid growth stage and (c) final stage, which are delineated by the different crystallization speeds measured in Fig. 5.2b.

5.3.3 Global Distribution of Salt Precipitation

Fig. 5.4a shows the final distribution of salt precipitation after the porous structure was completely dried. A large amount of salt accumulates locally at the position close to the outlet channel to form banded salt deposits, as highlighted by the yellow dash line. This banded precipitation can block accessible pathways for the injecting gas and can potentially damage the pore structure. How to explain the appearance of this massive local salt accumulation? We first noticed that the distribution of salt precipitation strongly depends on the initial location of residual brine. Large brine pools are trapped in the area close to the outlet channel. In contrast, the remaining brine of small and medium-size widely distributes around the region close to the injection channel after the majority of brine was drained by gas.

Fig. 5.4b shows the size-distribution of the salt deposits precipitated in the three nucleation stages. The bottom x-axis represents the size of salt nucleation in the unit of micron squares (μm^2), while the top axis is the number of pore spaces (being occupied by salt). From this statistic result of the salt distribution, about 75% of salt is nucleated during the (II) rapid growth stage. Most salt (more than 64%) that is precipitated in the initial stage (I) is smaller than $\approx 500 \mu m^2$ (i.e., $\approx 0.2\%$ of A_p). These small salt deposits mostly scatter around the near-inlet region but have little impact on the pore connectivity. In contrast, the salt aggregates of a size larger than $0.5 \times 10^5 \mu m^2$, occupying $\approx 20\%$ of A_p , are all jamming at the region close to the outlets of the channel to form the banded salt deposits as mentioned in Fig. 5.4a. This massive local precipitation can likely block the pathway of air flow that may potentially reduce the permeability of porous medium and affect the injectivity.

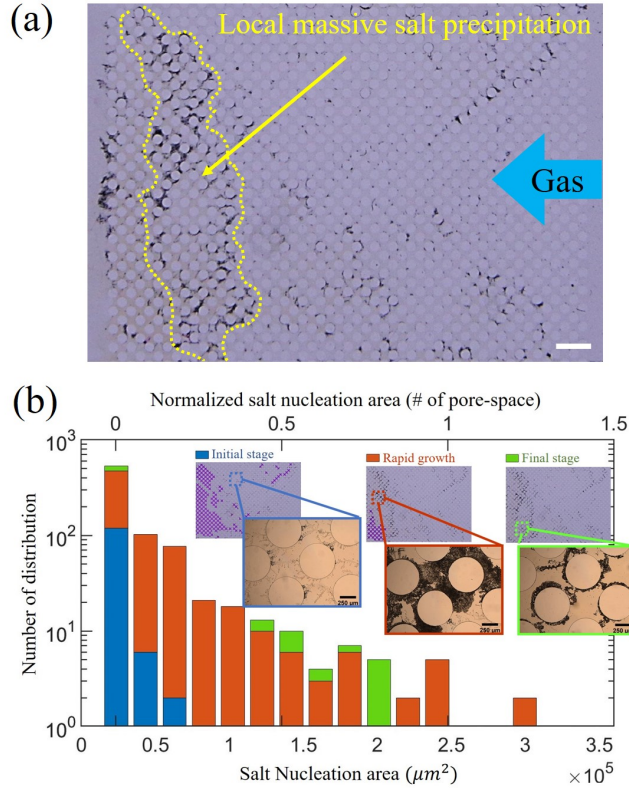


Figure 5.4. The spatial and size distributions of salt precipitation for the case of $\phi = 0.52$. (a) A snapshot of salt distribution after the porous system was completely dry. The scale bar represents 2 mm. (b) Statistical analysis of the size distribution of salt precipitations nucleated at the different stages: I, II, III, shown by the bars of ■, ■, ■, respectively. This distribution diagram presents the numbers of salt-nucleation spots of particular sizes, in μm^2 (in the bottom axis) and by the numbers of unit pore size of $A_P = 2.51 \times 10^5 \mu m^2$ (in the top axis).

5.3.4 Development of Extended Salt Precipitation

Shown in Fig. 5.5 are representative sequential snapshots demonstrating how a massive salt precipitation develops locally during the rapid growth stage (II). Initially, a few salt deposits have been precipitated near the large residual brine pools in the initial stage (I). The leftover brine was observed to shrink in the direction pointed by the blue arrows in Fig. 5.5a. With the brine shrinkage, the pore area, shown by the blue dashed rectangular in Fig. 5.5b, in front of the brine pool turns to the color of lighter purple, indicating the brine liquid moving from the original pore space to the salt-covered region. Simultaneously, more salt precipitates and further extends the coverage shown

in the red rectangular in Fig. 5.5c. This process is consistent with the self-enhancing mechanisms proposed by the previous studies [106, 103] and discussed above. The hydrophilic nature of salt sustains a brine film on the surfaces of salt aggregate, which helps deliver the residual brine pools to the areas of precipitated salt (see Fig 5.5d). As water keeps evaporating from the brine film, fresh brine is provided from the pool to the drying surface to dilute the salt concentration, as in Fig 5.5e. As a result, more salt ions transport to the drying area and enhance the growth of the salt aggregates to become massive salt precipitation (see Fig 5.5f).

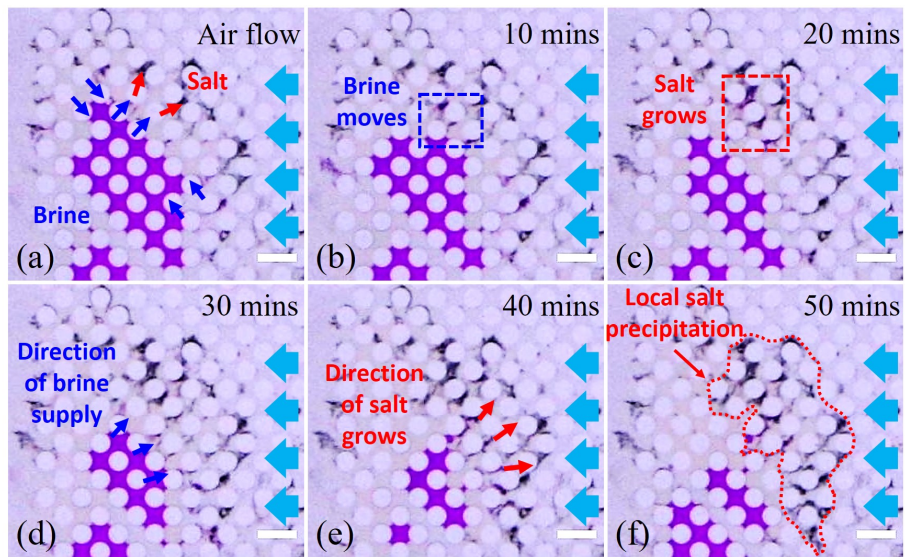


Figure 5.5. Development of local salt precipitation in the rapid growing regime (II). The representative image sequences are taken about 4 hours after air injection, with 10 minutes time lapse. Blue arrows indicate the flow direction of the brine, attracted by nucleated salt. Red arrows show the growing direction of salt aggregate, which attracts the fresh brine. The air flow goes from the right hand side. The scale bars represent 1 mm.

5.3.5 Effect of Porosity

The porosity not only is a key parameter measuring the permeability of the porous structure [276, 273] but also influences the competition between viscous and capillary forces on a multi-phase interface. [277, 273] Porosity, hence, can affect the transport of salt ions, which directly affects the rates of water evaporation and nucleation growth. As a major objective, here we investigate the influence of porosity on the distribution and size of salt precipitation. By comparing the microfluidic observations obtained from two porosity cases ($\phi = 0.52$ and $\phi = 0.23$), we observed that, under the same conditions of air injection (of $500 \mu\text{l}/\text{min}$), the cases of $\phi = 0.23$ require $\approx 20\%$ more time to initiate the drainage process than that of $\phi = 0.52$, because of a greater local capillary pressure to be overcome due to the low permeability (or porosity).

Fig. 5.6 reveals the correlation between the (areal) growing rate of salt nucleation (i.e., \dot{V}_{salt}/h) and the (areal) drying rate of residual brine (i.e., \dot{V}_{brine}/h) in the rapid growth stage (II) for three different initial salt concentrations, as the microfluidic gap (h) is kept constant. The dashed lines in Fig. 5.6 represent the fitting curves of linear regression, based on a least-squares fit. Detailedly, we carried out a fitting of simple linear regression of a functional form of $Y = aX + b + \epsilon$, where Y is the dependent (or responsive) variable (e.g., areal salt growing rate for Fig. 5.6), X is the independent (or input) variable (e.g., areal brine drying rate for Fig. 5.6), ϵ represents the error or residual. The fitting results explicitly describes a relationship between the response and input variables, with approximately a linear relationship. The fitting results also illustrate the positive correlation between salt precipitation and the evaporation of brine rates, with a constant and positive slope. More specifically, the slopes of the fitting lines are $a = 0.38 (\pm 0.12)$ for the large pore space ($\phi = 0.52$) and $a = 0.31 (\pm 0.12)$ for $\phi = 0.23$, as shown by the dashed lines in Fig. 5.6 a and b, respectively.

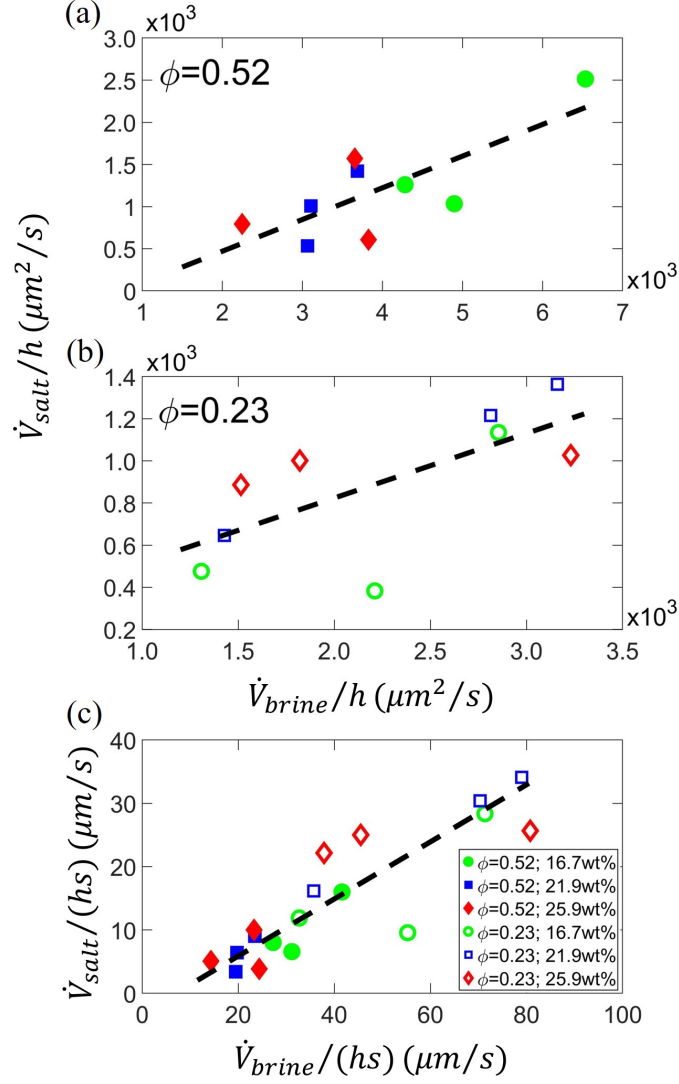


Figure 5.6. Correlations between the growth rate of salt nucleation and drying-rate of the residual brine in the (II) rapid growth phase of nucleation, for $\phi = 0.52$ and $\phi = 0.23$ in (a) and (b), respectively. Here, \dot{V}_{salt} and \dot{V}_{brine} represent the volumetric salt growing rate and brine drying rate, respectively; h ($= 25 \mu\text{m}$) is the uniform depth of the porous structures. (C) Data collapse of a new correlation of the data in (a) and (b) divided by the interspacing distance, s . The dashed lines represent best fitting results based on the (least-squares residual) linear fit for the corresponding variables in (a) – (c), respectively. As shown in SI Fig. S1, $s = 157.1 \mu\text{m}$ and $40 \mu\text{m}$ for $\phi = 0.52$ and $\phi = 0.23$, respectively.

The overall trend of the correlations shows that the greater evaporation rate, the higher salt growth rate. Residual brine evaporates faster in the media with large pore space ($\phi = 0.52$) and results in more salt nucleation. According to our measurements, the water evaporation rate is about

$3.9 \times 10^3 \mu\text{m}^2/s$ on average for the cases of $\phi = 0.52$, which is about 1.73 times than that of $\phi = 0.23$ ($\approx 2.26 \times 10^3 \mu\text{m}^2/s$) due to the larger air-brine contact area. Therefore, the salt-growing rate is faster on average (by $\approx 33\%$) in the cases of $\phi = 0.52$ ($\approx 1.2 \times 10^3 \mu\text{m}^2/s$) than those measured from $\phi = 0.23$ ($\approx 0.9 \times 10^3 \mu\text{m}^2/s$).

To further analyze the correlation between the salt-precipitation rate and brine drying rate for different ϕ , we divided the correlation data (Fig. 5.6 a-b) by their respective interspacing, s , between the two pillars and found a good data collapse, shown in Fig. 5.6c, for different ϕ and initial salt concentrations. Here, the quantity $\dot{V}_{\text{brine}}/(hs)$ physically can represent the receding speed of the residual brine undergoing drying, while $\dot{V}_{\text{salt}}/(hs)$ indicates the speed of local salt precipitation. The well-collapse of our data shown in Fig. 5.6c reveals a positive and universal correlation with a linear slope of 0.47 (± 0.04), i.e., implying the salt precipitation speed, $\dot{V}_{\text{salt}}/(hs)$, is about half of Relevant to the CCS in saline formations, this quantitative result would help predict the total amount and the rate of salt precipitation at pore-scale if the brine-drying rate is known or estimated for different porosities.

5.4 Conclusions

Our microfluidic results reveal the gas-liquid-solid interactions applicable to the CCS processes at pore scales and can offer the following implications for evaluating the effect of salt precipitation at an operational CCS site. First, the three distinct phases of salt precipitation are always observed at pore scales and could be expected during a CCS process. These distinct phases are dependent on the local drying rates of brine, resulting in various size distributions of salt crystals. Second, the positive correlation found, with good data collapse, can be used to relate the speed of salt nucleation with brine drying rate for different porosities. Third, the location of large brine pools plays an essential role in nucleating salt and, hence, the possibility of impairment of the CCS process. From our microfluidic measurements, on the one hand, we notice that small salt crystals precipitate first from the brine trapped in a single-pore area in the first phase, which has an insignificant influence on reducing formation permeability. On the other, in the second fast-drying phase, a large volume of residual brine trapped (close to the outlet) provides an ion source for extended salt nucleation via a self-enhancing mechanism with a capillary flow, providing a positive feedback loop. The extended salt nucleation can reduce the pore connectivity and, hence, hinder the displacement of CO_2 flow during the CCS deployment in deep saline aquifers.

Chapter 6

Conclusions and Outlook

6.1 Conclusions

This thesis describes experimental studies on the transport phenomena of CO₂-water system using microfluidic devices to mimic $P-T$ conditions and porous environments of a CO₂ storage reservoir. The aim of this work is to explore the microfluidic application on carbon storage engineering and to investigate how pressure elevation and porosity can influence pore-scale mass transfer.

Microfluidics can visualize the mass transport of CO₂ in water by recording the size change of CO₂ bubbles/droplets as they move along the microchannel after launching from the T-junction. According to the size change of CO₂ bubbles/droplets, we can extract the volumetric mass transfer, $k_L a$, to quantify the dynamic mass transport inside the microchannel. With the aid of the high-pressure microfluidic platform coupled with a ceramic heat plate, the CO₂ injection pressure can cover from 0.1 to 10 MPa, and the inlet temperature of liquids can reach up to 50 °C during the test (**Chapter 2**). This P-T range covers the CO₂ phase state from the gas to the liquid and the supercritical state.

The mass transfer of supercritical CO₂ is measured to be more intensive than that of in the gas and the liquid state, whereas the pressure elevation does not affect CO₂ mass transfer to water obviously at room temperature (**Chapter 3**). The measured $k_L a$ shows a dependency on the Reynolds number of the continuous phase, implying the significance of the bubbles/droplets moving speed. Moreover, the significant rise in the mass transfer of supercritical CO₂ may associate with the greater temperature and a shorter contact time of a fluid element on the CO₂-water interface, according to Higbie's penetration theory.

As injection conditions are close to the CO₂ gas-liquid phase boundary, an intriguing multiphase CO₂ emulsion is generated by merging the multiphase CO₂ flow with the continuous water phase at the T-junction (**Chapter 4**). We find that the mass transfer of CO₂ is more rapid at the beginning (right after leaving the T-junction) and decreases with time, which may attribute to the shrinking specific area, the increase of CO₂ concentration in water slugs, and the dependence on the moving speed.

Chapter 5 reveals the gas-liquid-solid interactions at pore scales to address the brine-drying and salt-growing relation for salt precipitation problems. Our results show that the salt growing rate increases linearly with the brine drying rate, while the structure of higher porosity dries brine faster and thus precipitates salt more rapidly due to a wider gas-liquid contact area. Also, large residual brine pools' location is crucial because they provide sufficient salt ions to build extended salt precipitation, which can reduce the pore connectivity and thus limit the CO₂ injection.

6.2 Outlook

6.2.1 Mass transfer of supercritical CO₂ in the microchannel

We have experimentally demonstrated the high-pressure microfluidic platform's capability to provide the essential mass transfer data of CO₂ in water for CCS applications (**Chapter 3** and **Chapter 4**). Our next step is to understand the mass transfer of supercritical CO₂ in more detail. First of all, we observed a considerable high $k_L a$ measured from supercritical CO₂ comparing to those from the gas and the liquid CO₂ with similar initial bubble/droplet size and traveling speed. Although we suspect that the temperature and the convective effect play key roles in the mass transport enhancement, the underlying mechanisms are still unclear. One of the potential options to further verify the data could be applying the PH value-sensitive fluorescent dye [118] to show the CO₂ concentration change in water slugs. Furthermore, the traveling speed of a bubble/droplet significantly influences the mass transport between two phases by controlling the liquid film thickness between the dispersed phase and sidewalls [278, 69], the mixing efficiency of the liquid film [70, 255], and the circulation intensity of continuous slugs [279, 280]. However, the optimum traveling speed of a CO₂ bubble/droplet in the microchannel representing the hydrodynamic condition in the reservoirs is still unclear in the literature. An additional systemic study to further understand the dependence of mass transfer of supercritical CO₂ on injection rate, including the moving speed and flow topology, is essential to link the microfluidic results and field operations. Finally, most of the pore fluids (brine) and

seawater have several inorganic ions dissolved. The salinity of brine has been experimentally proved to negatively influence both diffusivity [118] and solubility [117] of CO_2 in water. Our high-pressure microfluidic platform can systematically instigate the effect of salinity on the supercritical CO_2 mass transfer rate in various $P - T$ conditions.

6.2.2 Microfluidic salt precipitation by injecting supercritical CO_2

Chapter 5 has shown the capability of microfluidic methods to help visualize and quantify the dynamics of salt precipitation in pore-scale. The next step will be investigating the precipitation process during the injection of supercritical CO_2 using our high-pressure microfluidic platform. We may focus on three critical parameters influencing salt precipitation underground, which are the temperature effect, the CO_2 injection rate, and the aqueous phase's mobility [103]. The temperature is a key parameter that affects salt precipitation. The solubility of water in supercritical CO_2 increases with the rising temperature. As a result, more salt may precipitate as water becomes more soluble in the CO_2 phase [281, 261]. Nevertheless, the experimental study addressing the temperature effect on salt precipitation, is still rare that could be a potential future work.

Some studies have suggested that a high CO_2 injection rate would, on the one hand, remedy the intensive salt accumulation because the increased pressure gradient suppresses the capillary backflow [263, 282, 283, 261]. On the other hand, however, an increase in the injection pressure may result in a slower mean speed of CO_2 due to the dependence of viscosity on pressure, leading to a higher evaporation rate of residual brine and more extensive salt precipitation [284]. An optimized injection rate (mean flow speed of CO_2) is essential for minimizing the impact from salt precipitation.

Moreover, the mobility of brine controls the injection pressure and the saturation of residual brine. The latter has a significant influence on salt precipitation in terms of distribution and total volume, as demonstrated in **Chapter 5**. Brine would become more mobile as the substrate's wettability tends to oil-wet (hydrophobic). It thus reduces the coverage of residual brine and less salt precipitation. In addition, the more mobile brine may increase the mean injection speed of CO_2 that suppresses the capillary backflow [282]. Studying the combining effect of surface wettability and critical injection rate on salt precipitation could be an exciting topic for evaluating the storage site's rock properties.

References

- [1] Mohamed Gad-El-Hak. The fluid mechanics of microdevices—the freeman scholar lecture. *Journal of Fluids Engineering*, 121(1):5–33, 1999.
- [2] George M. Whitesides. The origins and the future of microfluidics. *Nature*, 442(7101):368–373, 2006.
- [3] Andreas Manz, D. Jed Harrison, Elisabeth M.J. Verpoorte, James C. Fettingner, Aran Paulus, Hans Lüdi, and H. Michael Widmer. Planar chips technology for miniaturization and integration of separation techniques into monitoring systems. capillary electrophoresis on a chip. *Journal of Chromatography A*, 593(1-2):253–258, 1992.
- [4] P. Gravesen, J. Branebjerg, and O.S. Jensen. Microfluidics-a review. *Journal of Micromechanics and Microengineering*, 3:168–182, 1993.
- [5] Chih-ming Ho and Yu-chong Tai. Micro-electro-mechanical-systems (mems) and fluid flows. *Annual Review of Fluid Mechanics*, 30:579–612, 1998.
- [6] Howard A. Stone, Abraham D. Stroock, and Armand Ajdari. Engineering flows in small devices: Microfluidics toward a lab-on-a-chip. *Annual Review of Fluid Mechanics*, 36:381–411, 2004.
- [7] Dino Di Carlo. Inertial microfluidics. *Lab on a Chip*, 9(21):3038–3046, 2009.
- [8] Jun Zhang, Sheng Yan, Dan Yuan, Gursel Alici, Nam Trung Nguyen, Majid Ebrahimi Warkiani, and Weihua Li. Fundamentals and applications of inertial microfluidics: A review. *Lab on a Chip*, 16(1):10–34, 2016.
- [9] Katherine S. Elvira, Xavier Casadevall I Solvas, Robert C.R. Wootton, and Andrew J. Demello. The past, present and potential for microfluidic reactor technology in chemical synthesis. *Nature Chemistry*, 5(11):905–915, 2013.
- [10] Chia Yen Lee, Chin Lung Chang, Yao Nan Wang, and Lung Ming Fu. Microfluidic mixing: A review. *International Journal of Molecular Sciences*, 12(5):3263–3287, 2011.

- [11] Kai Wang and Guangsheng Luo. Microflow extraction: A review of recent development. *Chemical Engineering Science*, 169:18–33, 2017.
- [12] Chun Xia Zhao and Anton P. J. Middelberg. Two-phase microfluidic flows. *Chemical Engineering Science*, 66(7):1394–1411, 2011.
- [13] Taotao Fu and Youguang Ma. Bubble formation and breakup dynamics in microfluidic devices: A review. *Chemical Engineering Science*, 135:343–372, 2015.
- [14] Pingan Zhu and Liqiu Wang. Passive and active droplet generation with microfluidics: a review. *Lab on a Chip*, 17(1):34–75, 2017.
- [15] Howard A. Stone and S. Kim. Microfluidics: basic issues, applications, and challenges. *AIChE Journal*, 47(6):1250–1254, 2001.
- [16] Nam-Trung Nguyen, Steven T. Wereley, and Seyed Ali Mousavi Shaegh. *Fundamentals and applications of microfluidics*. Artech house, 2019.
- [17] Bo Bao, Jason Riordon, Farshid Mostowfi, and David Sinton. Microfluidic and nanofluidic phase behaviour characterization for industrial CO₂, oil and gas. *Lab on a Chip*, 17(16):2740–2759, 2017.
- [18] William S. Janna. *Engineering heat transfer*. CRC press, 2018.
- [19] Thomas K. Sherwood, Robert L. Pigford, and Charles R. Wilke. *Mass transfer*. McGraw-Hill, 1975.
- [20] Erik Kjeang, Ned Djilali, and David Sinton. Microfluidic fuel cells: A review. *Journal of Power Sources*, 186(2):353–369, 2009.
- [21] David Sinton. Energy: The microfluidic frontier. *Lab on a Chip*, 14(17):3127–3134, 2014.
- [22] Victor A. Lifton. Microfluidics: An enabling screening technology for enhanced oil recovery (EOR). *Lab on a Chip*, 16(10):1777–1796, 2016.
- [23] Milad Abolhasani, Axel Günther, and Eugenia Kumacheva. Microfluidic studies of carbon dioxide. *Angewandte Chemie International Edition*, 53(31):7992–8002, 2014.
- [24] Taotao Fu. Microfluidics in CO₂ capture, sequestration, and applications. *Advances in Microfluidics - New Applications in Biology, Energy, and Materials Sciences*, 2016.
- [25] Zhanxiao Kang, Tiantian Kong, Leyan Lei, Pingan Zhu, Xiaowei Tian, and Liqiu Wang. Engineering particle morphology with microfluidic droplets. *Journal of Micromechanics and Microengineering*, 26(7), 2016.
- [26] J. K. Nunes, S. S. H. Tsai, J. Wan, and H. A. Stone. Dripping and jetting in microfluidic multiphase flows applied to particle and fibre synthesis. *Journal of Physics D: Applied Physics*,

46(11), 2013.

- [27] Sujit S. Datta, Alireza Abbaspourrad, Esther Amstad, Jing Fan, Shin Hyun Kim, Mark Romanowsky, Ho Cheung Shum, Bingjie Sun, Andrew S. Utada, Maike Windbergs, Shaobing Zhou, and David A. Weitz. 25th anniversary article: Double emulsion templated solid microcapsules: Mechanics and controlled release. *Advanced Materials*, 26(14):2205–2218, 2014.
- [28] Tae Yong Lee, Tae Min Choi, Tae Soup Shim, Raoul A.M. Frijns, and Shin Hyun Kim. Microfluidic production of multiple emulsions and functional microcapsules. *Lab on a Chip*, 16(18):3415–3440, 2016.
- [29] Ronald Suryo and Osman A. Basaran. Tip streaming from a liquid drop forming from a tube in a co-flowing outer fluid. *Physics of Fluids*, 18(8), 2006.
- [30] Andrew. S. Utada, L Chu, D. R. Link, C Holtze, and David. A. Weitz. Dripping, jetting, drops, and wetting : Microfluidics. *Mrs Bulletin*, 32:702–708, 2007.
- [31] Shelley Lynn Anna. Droplets and bubbles in microfluidic devices. *Annual Review of Fluid Mechanics*, 48:285–309, 2016.
- [32] Todd Thorsen, Richard W. Roberts, Frances H. Arnold, and Stephen R. Quake. Dynamic pattern formation in a vesicle-generating microfluidic device. *Physical Review Letters*, 86(18):4163–4166, 2001.
- [33] J. H. Xu, S. W. Li, J Tan, Y. J. Wang, and G. S. Luo. Preparation of highly monodisperse droplet in a t-junction microfluidic device. *AIChE Journal*, 52:3005–3010, 2006.
- [34] Adam R. Abate and David A. Weitz. Air-bubble-triggered drop formation in microfluidics. *Lab on a Chip*, 11(10):1713–1716, 2011.
- [35] P. B. Umbanhowar, V Prasad, and David A Weitz. Monodisperse emulsion generation via drop break off in a coflowing stream. *Langmuir*, 16(2):347–351, 2000.
- [36] Carsten Cramer, Peter Fischer, and Erich J. Windhab. Drop formation in a co-flowing ambient fluid. *Chemical Engineering Science*, 59(15):3045–3058, 2004.
- [37] Andrew S. Utada, Alberto Fernandez-Nieves, Howard A. Stone, and David A. Weitz. Dripping to jetting transitions in coflowing liquid streams. *Physical Review Letters*, 99(9):1–4, 2007.
- [38] A. G. Marín, F. Campo-Cortés, and J. M. Gordillo. Generation of micron-sized drops and bubbles through viscous coflows. *Colloids and Surfaces A: Physicochemical and Engineering Aspects*, 344(1-3):2–7, 2009.
- [39] Piotr Garstecki, Howard A. Stone, and George M. Whitesides. Mechanism for flow-rate controlled breakup in confined geometries: A route to monodisperse emulsions. *Physical Review*

- Letters*, 94(16):1–4, 2005.
- [40] Alfonso M. Gañán-Calvo. Generation of Steady Liquid Microthreads and Micron-Sized Monodisperse Sprays in Gas Streams. *Physical Review Letters*, 80(2):285–288, 1998.
- [41] Alfonso M. Gañán-Calvo and J. M. Gordillo. Perfectly monodisperse microbubbling by capillary flow focusing. *Physical Review Letters*, 87(27 I):2745011–2745014, 2001.
- [42] Alfonso M. Gañán-Calvo, Román González-Prieto, Pascual Riesco-Chueca, Miguel A. Herrada, and María Flores-Mosquera. Focusing capillary jets close to the continuum limit. *Nature Physics*, 3(10):737–742, 2007.
- [43] Levent Yobas, Stefan Martens, Wee Liat Ong, and Nagarajan Ranganathan. High-performance flow-focusing geometry for spontaneous generation of monodispersed droplets. *Lab on a Chip*, 6(8):1073–1079, 2006.
- [44] Shoji Takeuchi, Piotr Garstecki, Douglas B. Weibel, and George M. Whitesides. An axisymmetric flow-focusing microfluidic device. *Advanced Materials*, 17(8):1067–1072, 2005.
- [45] A. S. Utada, E. Lorenceau, D. R. Link, P. D. Kaplan, H. A. Stone, and D. A. Weitz. Monodisperse double emulsions generated from a microcapillary device. *Science*, 308(5721):537–541, 2005.
- [46] Piotr Garstecki, Irina Gitlin, Willow Diluzio, George M. Whitesides, Eugenia Kumacheva, and Howard A. Stone. Formation of monodisperse bubbles in a microfluidic flow-focusing device. *Applied Physics Letters*, 85(13):2649–2651, 2004.
- [47] Shelley L. Anna and Hans C. Mayer. Microscale tipstreaming in a microfluidic flow focusing device. *Physics of Fluids*, 18(12), 2006.
- [48] Pingan Zhu, Tiantian Kong, Zhanxiao Kang, Xiaowei Tian, and Liqiu Wang. Tip-multi-breaking in capillary microfluidic devices. *Scientific Reports*, 5:1–8, 2015.
- [49] Joshua D. Tice, Adam D. Lyon, and Rustem F. Ismagilov. Effects of viscosity on droplet formation and mixing in microfluidic channels. *Analytica Chimica Acta*, 507(1):73–77, 2004.
- [50] Piotr Garstecki, Michael J. Fuerstman, Howard A. Stone, and George M. Whitesides. Formation of droplets and bubbles in a microfluidic T-junction - Scaling and mechanism of break-up. *Lab on a Chip*, 6(3):437–446, 2006.
- [51] M. De menez, P. Garstecki, F. Jousse, and H. A. Stone. Transition from squeezing to dripping in a microfluidic T-shaped junction. *Journal of Fluid Mechanics*, 595:141–161, 2008.
- [52] Pierre Guillot, Annie Colin, Andrew S. Utada, and Armand Ajdari. Stability of a jet in confined pressure-driven biphasic flows at low reynolds numbers. *Physical Review Letters*,

- 99(10):1–4, 2007.
- [53] Jing Fan, Yuxiang Zhang, and Liqiu Wang. Formation of nanoliter bubbles in microfluidic T-junctions. *Nano*, 5(3):175–184, 2010.
- [54] Michele Zagnoni, Jamie Anderson, and Jonathan M. Cooper. Hysteresis in multiphase microfluidics at a T-junction. *Langmuir*, 26(12):9416–9422, 2010.
- [55] T. C. Thulasidas, M. A. Abraham, and R. L. Cerro. Flow patterns in liquid slugs during bubble-train flow inside capillaries. *Chemical Engineering Science*, 52(17):2947–2962, 1997.
- [56] P. Angeli and A. Gavriilidis. Hydrodynamics of taylor flow in small channels: A review. *Proceedings of the Institution of Mechanical Engineers, Part C: Journal of Mechanical Engineering Science*, 222(5):737–751, 2008.
- [57] Said Irandoust, Sylvie Ertlé, and Bengt Andersson. Gas-liquid mass transfer in taylor flow through a capillary. *The Canadian Journal of Chemical Engineering*, 70(1):115–119, 1992.
- [58] Roland Clift, John R Grace, and Martin E Weber. *Bubbles, drops, and particles*. Courier Corporation, 2005.
- [59] P. Sobieszuk, J. Aubin, and R. Pohorecki. Hydrodynamics and mass transfer in gas-liquid flows in microreactors. *Chemical Engineering and Technology*, 35(8):1346–1358, 2012.
- [60] Axel Günther, Saif A. Khan, Martina Thalmann, Franz Trachsel, and Klavs F. Jensen. Transport and reaction in microscale segmented gas-liquid flow. *Lab on a Chip*, 4(4):278–286, 2004.
- [61] Axel Günther, Manish Jhunjhunwala, Martina Thalmann, Martin A. Schmidt, and Klavs F. Jensen. Micromixing of miscible liquids in segmented gas-liquid flow. *Langmuir*, 21(4):1547–1555, 2005.
- [62] Severin Waelchli and Philipp Rudolf von Rohr. Two-phase flow characteristics in gas-liquid microreactors. *International Journal of Multiphase Flow*, 32(7):791–806, 2006.
- [63] Volkert van Steijn, Michiel T. Kreutzer, and Chris R. Kleijn. μ -PIV study of the formation of segmented flow in microfluidic T-junctions. *Chemical Engineering Science*, 62(24):7505–7514, 2007.
- [64] Christoph Meyer, Marko Hoffmann, and Michael Schlüter. Micro-PIV analysis of gas-liquid Taylor flow in a vertical oriented square shaped fluidic channel. *International Journal of Multiphase Flow*, 67:140–148, 2014.
- [65] J. M. van Baten and R. Krishna. CFD simulations of mass transfer from Taylor bubbles rising in circular capillaries. *Chemical Engineering Science*, 59(12):2535–2545, 2004.
- [66] C. O. Vandu, H. Liu, and R. Krishna. Mass transfer from Taylor bubbles rising in single

- capillaries. *Chemical Engineering Science*, 60(22):6430–6437, 2005.
- [67] C. O. Vandu, J. Ellenberger, and R. Krishna. Hydrodynamics and mass, transfer in an up-flow monolith loop reactor. *Chemical Engineering and Processing: Process Intensification*, 44(3):363–374, 2005.
- [68] N. Dietrich, K. Loubière, M. Jimenez, G. Hébrard, and C. Gourdon. A new direct technique for visualizing and measuring gas-liquid mass transfer around bubbles moving in a straight millimetric square channel. *Chemical Engineering Science*, 100:172–182, 2013.
- [69] Youngbae Han and Naoki Shikazono. Measurement of the liquid film thickness in micro tube slug flow. *International Journal of Heat and Fluid Flow*, 30(5):842–853, 2009.
- [70] Ryszard Pohorecki. Effectiveness of interfacial area for mass transfer in two-phase flow in microreactors. *Chemical Engineering Science*, 62(22):6495–6498, 2007.
- [71] Simon Kuhn and Klavs F. Jensen. A pH-sensitive laser-induced fluorescence technique to monitor mass transfer in multiphase flows in microfluidic devices. *Industrial and Engineering Chemistry Research*, 51(26):8999–9006, 2012.
- [72] Chaoqun Yao, Zhengya Dong, Yuchao Zhao, and Guangwen Chen. An online method to measure mass transfer of slug flow in a microchannel. *Chemical Engineering Science*, 112:15–24, 2014.
- [73] Niall MacDowell, Nick Florin, Antoine Buchard, Jason Hallett, Amparo Galindo, George Jackson, Claire S. Adjiman, Charlotte K. Williams, Nilay Shah, and Paul Fennell. An overview of CO₂ capture technologies. *Energy & Environmental Science*, 3(11):1645–1669, 2010.
- [74] Ahmed Al-Mamoori, Anirudh Krishnamurthy, Ali A. Rownaghi, and Fateme Rezaei. Carbon capture and utilization update. *Energy Technology*, 5(6):834–849, 2017.
- [75] Matthew E. Boot-Handford, Juan C. Abanades, Edward J. Anthony, Martin J. Blunt, Stefano Brandani, Niall Mac Dowell, José R. Fernández, Maria Chiara Ferrari, Robert Gross, Jason P. Hallett, R. Stuart Haszeldine, Philip Heptonstall, Anders Lyngfelt, Zen Makuch, Enzo Mangano, Richard T.J. Porter, Mohamed Pourkashanian, Gary T. Rochelle, Nilay Shah, Joseph G. Yao, and Paul S. Fennell. Carbon capture and storage update. *Energy & Environmental Science*, 7(1):130–189, 2014.
- [76] Rosa M. Cuéllar-Franca and Adisa Azapagic. Carbon capture, storage and utilisation technologies: A critical analysis and comparison of their life cycle environmental impacts. *Journal of CO₂ Utilization*, 9:82–102, 2015.
- [77] Stefan Bachu, W. D. Gunter, and E. H. Perkins. Aquifer disposal of CO₂: Hydrodynamic and

- mineral trapping. *Energy Conversion and Management*, 35(4):269–279, 1994.
- [78] Bert Metz, Ogunlade Davidson, Heleen De Coninck, et al. *Carbon dioxide capture and storage: special report of the intergovernmental panel on climate change*. Cambridge University Press, 2005.
- [79] Hongqun Yang, Zhenghe Xu, Maohong Fan, Rajender Gupta, Rachid B. Slimane, Alan E. Bland, and Ian Wright. Progress in carbon dioxide separation and capture: A review. *Journal of Environmental Sciences*, 20(1):14–27, 2008.
- [80] E. Eric Adams and Ken Caldeira. Ocean storage of CO₂. *Elements*, 4(5):319–324, 2008.
- [81] Curt M. White, Brian R. Strazisar, Evan J. Granite, James S. Hoffman, and Henry W. Pennline. Separation and capture of CO₂ from large stationary sources and sequestration in geological formations—coalbeds and deep saline aquifers. *Journal of the Air and Waste Management Association*, 53(6):645–715, 2003.
- [82] Philip H. Nelson. Pore-throat sizes in sandstones, tight sandstones, and shales. *AAPG bulletin*, 93(3):329–340, 2009.
- [83] Richa Shukla, Pathegama Ranjith, Asadul Haque, and Xavier Choi. A Review of Studies on CO₂ Sequestration and Caprock Integrity. *Fuel*, 89(10):2651–2664, 2010.
- [84] Saeko Mito, Ziqiu Xue, and Tatsuya Sato. Effect of formation water composition on predicting CO₂ behavior: A case study at the nagaoka post-injection monitoring site. *Applied Geochemistry*, 30:33–40, 2013.
- [85] Weon Shik Han, Si Yong Lee, Chuan Lu, Brian J. McPherson, and Richard Esser. Role of correlation structures of permeability field on residual trapping mechanisms and buoyancy-driven CO₂ migration. *Energy Procedia*, 1(1):3493–3498, 2009.
- [86] Youngsoo Lee, Kihong Kim, Wonmo Sung, and Inhang Yoo. Analysis of the leakage possibility of injected CO₂ in a saline aquifer. *Energy and Fuels*, 24(5):3292–3298, 2010.
- [87] P. J. Armitage, R. H. Worden, D. R. Faulkner, A. C. Aplin, A. R. Butcher, and A. A. Espie. Mercia mudstone formation caprock to carbon capture and storage sites: Petrology and petrophysical characteristics. *Journal of the Geological Society*, 170(1):119–132, 2013.
- [88] Barbara Cantucci, Giordano Montegrossi, Orlando Vaselli, Franco Tassi, Fedora Quattrocchi, and Ernie H. Perkins. Geochemical Modeling of CO₂ Storage in Deep Reservoirs: The Weyburn Project (Canada) case study. *Chemical Geology*, 265(1-2):181–197, 2009.
- [89] Guttorm Alendal and Helge Drange. Two-phase, near-field modeling of purposefully released CO₂ in the ocean. *Journal of Geophysical Research: Oceans*, 106(C1):1085–1096, 2001.

- [90] Toru Sato and Kei Sato. Numerical prediction of the dilution process and its biological impacts in CO₂ ocean sequestration. *Journal of Marine Science and Technology*, 6(4):169–180, 2002.
- [91] Danae A. Voormeij and George J. Simandl. Geological, ocean, and mineral CO₂ sequestration options: A technical review. *Geoscience Canada*, 31(1):11–22, 2004.
- [92] Roland Lenormand, Eric Touboul, and Cesar Zarcone. Numerical models and experiments on immiscible displacements in porous media. *Journal of Fluid Mechanics*, 189:165–187, 1988.
- [93] Luqman K. Abidoye, Kamal J. Khudaida, and Diganta B. Das. Geological carbon sequestration in the context of two-phase flow in porous media: a review. *Critical Reviews in Environmental Science and Technology*, 45(11):1105–1147, 2015.
- [94] Sally M. Benson and David R. Cole. CO₂ sequestration in deep sedimentary formations. *Elements*, 4(5):325–331, 2008.
- [95] Fang Yang, Baojun Bai, Dazhen Tang, Dunn-Norman Shari, and Wronkiewicz David. Characteristics of CO₂ sequestration in saline aquifers. *Petroleum Science*, 7(1):83–92, 2010.
- [96] Changyong Zhang, Mart Oostrom, Jay W. Grate, Thomas W. Wietsma, and Marvin G. Warner. Liquid CO₂ displacement of water in a dual-permeability pore network micromodel. *Environmental Science & Technology*, 45(17):7581–7588, 2011.
- [97] Markus Buchgraber, Anthony R. Kovscek, and Louis M. Castanier. A study of microscale gas trapping using etched silicon micromodels. *Transport in Porous Media*, 95(3):647–668, 2012.
- [98] Xianglei Zheng, Nariman Mahabadi, Tae Sup Yun, and Jaewon Jang. Effect of capillary and viscous force on co₂ saturation and invasion pattern in the microfluidic chip. *Journal of Geophysical Research: Solid Earth*, 122(3):1634–1647, 2017.
- [99] C. Chalbaud, M. Robin, J. M. Lombard, F. Martin, P. Egermann, and H. Bertin. Interfacial tension measurements and wettability evaluation for geological CO₂ storage. *Advances in Water Resources*, 32(1):98–109, 2009.
- [100] Sandy Morais, Na Liu, Abdou Diouf, Dominique Bernard, Carole Lecoutre, Yves Garrabos, and Samuel Marre. Monitoring CO₂ invasion processes at the pore scale using geological labs on chip. *Lab on a Chip*, 16(18):3493–3502, 2016.
- [101] Seunghye Kim and J. Carlos Santamarina. Engineered CO₂ injection: The use of surfactants for enhanced sweep efficiency. *International Journal of Greenhouse Gas Control*, 20:324–332, 2014.
- [102] Nadja Muller, Ran Qi, Elizabeth Mackie, Karsten Pruess, and Martin J. Blunt. CO₂ injection impairment due to halite precipitation. *Energy Procedia*, 1(1):3507–3514, 2009.

- [103] Rohaldin Miri and Helge Hellevang. Salt precipitation during CO₂ storage a review. *International Journal of Greenhouse Gas Control*, 51:136–147, 2016.
- [104] Arshad Raza, Reza Rezaee, Raouf Gholami, Vamegh Rasouli, Chua Han Bing, Ramasamy Nagarajan, and Mohamed Ali Hamid. Injectivity and quantification of capillary trapping for CO₂ storage: a review of influencing parameters. *Journal of Natural Gas Science and Engineering*, 26:510–517, 2015.
- [105] Myeongsub Kim, Andrew Sell, and David Sinton. Aquifer-on-a-chip: understanding pore-scale salt precipitation dynamics during CO₂ sequestration. *Lab on a Chip*, 13(13):2508–2518, 2013.
- [106] Rohaldin Miri, Reinier van Noort, Per Aagaard, and Helge Hellevang. New insights on the physics of salt precipitation during injection of CO₂ into saline aquifers. *International Journal of Greenhouse Gas Control*, 43:10–21, 2015.
- [107] Antoine Naillon, Pierre Joseph, and Marc Prat. Sodium chloride precipitation reaction coefficient from crystallization experiment in a microfluidic device. *Journal of Crystal Growth*, 463:201–210, 2017.
- [108] Mohammad Nooraiepour, Hossein Fazeli, Rohaldin Miri, and Helge Hellevang. Effect of CO₂ phase states and flow rate on salt precipitation in shale caprocks—a microfluidic study. *Environmental Science & Technology*, 52(10):6050–6060, 2018.
- [109] Ayorinde Rufai and John Crawshaw. Effect of wettability changes on evaporation rate and the permeability impairment due to salt deposition. *ACS Earth and Space Chemistry*, 2(4):320–329, 2018.
- [110] Mohammed D. Aminu, Seyed Ali Nabavi, Christopher A. Rochelle, and Vasilije Manovic. A review of developments in carbon dioxide storage. *Applied Energy*, 208:1389–1419, 2017.
- [111] GPD De Silva, Pathegama G. Ranjith, and MSA Perera. Geochemical aspects of CO₂ sequestration in deep saline aquifers: A review. *Fuel*, 155:128–143, 2015.
- [112] Gorazd Berčič and Albin Pintar. The role of gas bubbles and liquid slug lengths on mass transport in the Taylor flow through capillaries. *Chemical Engineering Science*, 52(21-22):3709–3719, 1997.
- [113] Jun Yue, Guangwen Chen, Quan Yuan, Lingai Luo, and Yves Gonthier. Hydrodynamics and mass transfer characteristics in gas-liquid flow through a rectangular microchannel. *Chemical Engineering Science*, 62(7):2096–2108, 2007.
- [114] Ruopeng Sun and Thomas Cubaud. Dissolution of carbon dioxide bubbles and microfluidic multiphase flows. *Lab on a Chip*, 11(17):2924–2928, 2011.

- [115] Ethan Tumarkin, Zhihong Nie, Jai Il Park, Milad Abolhasani, Jesse Greener, Barbara Sherwood-Lollar, Axel Günther, and Eugenia Kumacheva. Temperature-controlled 'breathing' of carbon dioxide bubbles. *Lab on a Chip*, 11(20):3545–3550, 2011.
- [116] Suin Shim, Jiandi Wan, Sascha Hilgenfeldt, Prathamesh D. Panchal, and Howard A. Stone. Dissolution without disappearing: Multicomponent gas exchange for CO₂ bubbles in a microfluidic channel. *Lab on a Chip*, 14(14):2428–2436, 2014.
- [117] N. Liu, C. Aymonier, C. Lecoutre, Y. Garrabos, and S. Marre. Microfluidic approach for studying CO₂ solubility in water and brine using confocal Raman spectroscopy. *Chemical Physics Letters*, 551:139–143, 2012.
- [118] Andrew Sell, Hossein Fadaei, Myeongsub Kim, and David Sinton. Measurement of CO₂ diffusivity for carbon sequestration: A microfluidic approach for reservoir-specific analysis. *Environmental Science & Technology*, 47(1):71–78, 2013.
- [119] Chaoqun Yao, Zhengya Dong, Yuchao Zhao, and Guangwen Chen. Gas-liquid flow and mass transfer in a microchannel under elevated pressures. *Chemical Engineering Science*, 123:137–145, 2015.
- [120] Ning Qin, John Z. Wen, Baixin Chen, and Carolyn L. Ren. On nonequilibrium shrinkage of supercritical CO₂ droplets in a water-carrier microflow. *Applied Physics Letters*, 113(3), 2018.
- [121] Samuel Marre, Yann Roig, and Cyril Aymonier. Supercritical microfluidics: Opportunities in flow-through chemistry and materials science. *The Journal of Supercritical Fluids*, 66:251–264, 2012.
- [122] Nora Assmann, Stefan Kaiser, and Philipp Rudolf von Rohr. Supercritical extraction of vanillin in a microfluidic device. *The Journal of Supercritical Fluids*, 67:149–154, 2012.
- [123] Sebastian K. Luther and Andreas Braeuer. High-pressure microfluidics for the investigation into multi-phase systems using the supercritical fluid extraction of emulsions (sfee). *The Journal of Supercritical Fluids*, 65:78–86, 2012.
- [124] Juta Kobayashi, Yuichiro Mori, and Shū Kobayashi. Hydrogenation reactions using scCO₂ as a solvent in microchannel reactors. *Chemical communications*, (20):2567–2568, 2005.
- [125] F. Trachsel, B. Tidona, S. Desportes, and P. h. Rudolf von Rohr. Solid catalyzed hydrogenation in a Si/glass microreactor using supercritical CO₂ as the reaction solvent. *The Journal of Supercritical Fluids*, 48(2):146–153, 2009.
- [126] Bruno Tidona, Clemens Koppold, Atul Bansode, Atsushi Urakawa, and Philipp Rudolf von Rohr. CO₂ hydrogenation to methanol at pressures up to 950 bar. *The Journal of Supercritical*

- Fluids*, 78:70–77, 2013.
- [127] Fernando Benito-Lopez, Roald M. Tiggelaar, Katarzyna Salbut, Jurriaan Huskens, Richard J. M. Egberink, David N. Reinhoudt, Han JGE Gardeniers, and Willem Verboom. Substantial rate enhancements of the esterification reaction of phthalic anhydride with methanol at high pressure and using supercritical CO₂ as a co-solvent in a glass microreactor. *Lab on a Chip*, 7(10):1345–1351, 2007.
- [128] Klaus Jähnisch, Volker Hessel, Holger Löwe, and Manfred Baerns. Chemistry in microstructured reactors. *Angewandte Chemie International Edition*, 43(4):406–446, 2004.
- [129] Aaron K. Goodwin and Gregory L. Rorrer. Conversion of glucose to hydrogen-rich gas by supercritical water in a microchannel reactor. *Industrial and engineering chemistry research*, 47(12):4106–4114, 2008.
- [130] Aaron K. Goodwin and Gregory L. Rorrer. Conversion of xylose and xylose-phenol mixtures to hydrogen-rich gas by supercritical water in an isothermal microtube flow reactor. *Energy and Fuels*, 23(7):3818–3825, 2009.
- [131] Tahseen Razzaq, Toma N. Glasnov, and C. Oliver Kappe. Continuous-flow microreactor chemistry under high-temperature/pressure conditions. *European Journal of Organic Chemistry*, 2009(9):1321–1325, 2009.
- [132] M. Al-Rawashdeh, F. Yu, T. A. Nijhuis, E. V. Rebrov, V. Hessel, and J. C. Schouten. Numbered-up gas-liquid micro/milli channels reactor with modular flow distributor. *Chemical engineering journal*, 207:645–655, 2012.
- [133] Mahtab NaderiNasrabadi, Yadollah Mortazavi, and Abbas Ali Khodadadi. Highly sensitive and selective Gd₂O₃-doped SnO₂ ethanol sensors synthesized by a high temperature and pressure solvothermal method in a microreactor. *Sensors and Actuators B: Chemical*, 230:130–139, 2016.
- [134] Takahisa Masuzawa. State of the art of micromachining. *Cirp Annals*, 49(2):473–488, 2000.
- [135] K. H. Ho and S. T. Newman. State of the art electrical discharge machining (edm). *International Journal of Machine Tools and Manufacture*, 43(13):1287–1300, 2003.
- [136] KM Ahmmed, Colin Grambow, and Anne-Marie Kietzig. Fabrication of micro/nano structures on metals by femtosecond laser micromachining. *Micromachines*, 5(4):1219–1253, 2014.
- [137] Ciprian Iliescu, Bangtao Chen, and Jianmin Miao. On the wet etching of pyrex glass. *Sensors and actuators A: Physical*, 143(1):154–161, 2008.
- [138] Che-Hsin Lin, Gwo-Bin Lee, Yen-Heng Lin, and Guan-Liang Chang. A fast prototyping

- process for fabrication of microfluidic systems on soda-lime glass. *Journal of Micromechanics and Microengineering*, 11(6):726, 2001.
- [139] Francis E. H. Tay, Ciprian Iliescu, Ji Jing, and Jianmin Miao. Defect-free wet etching through pyrex glass using Cr/Au mask. *Microsystem technologies*, 12(10-11):935–939, 2006.
- [140] R. Mazurczyk, G. El Khoury, V. Dugas, B. Hannes, E. Laurenceau, M. Cabrera, S. Krawczyk, E. Souteyrand, J. P. Cloarec, and Y. Chevolot. Low-cost, fast prototyping method of fabrication of the microreactor devices in soda-lime glass. *Sensors and Actuators B: Chemical*, 128(2):552–559, 2008.
- [141] Roald M. Tiggelaar, Fernando Benito-López, Dorothee C. Hermes, Helmut Rathgen, Richard J. M. Egberink, Frieder G. Mugele, David N. Reinhoudt, Albert van den Berg, Willem Verboom, and Han JGE Gardeniers. Fabrication, mechanical testing and application of high-pressure glass microreactor chips. *Chemical Engineering Journal*, 131(1-3):163–170, 2007.
- [142] Martin Andersson, Klas Hjort, and Lena Klintberg. Fracture strength of glass chips for high-pressure microfluidics. *Journal of Micromechanics and Microengineering*, 26(9):095009, 2016.
- [143] Willem Verboom. Selected examples of high-pressure reactions in glass microreactors. *Chemical Engineering & Technology: Industrial Chemistry-Plant Equipment-Process Engineering-Biotechnology*, 32(11):1695–1701, 2009.
- [144] Laszlo Szekeley and Ruth Freitag. Fabrication of a versatile microanalytical system without need for clean room conditions. *Analytica chimica acta*, 512(1):39–47, 2004.
- [145] Xinghua Li, Takashi Abe, and Masayoshi Esashi. Deep reactive ion etching of pyrex glass using SF₆ plasma. *Sensors and actuators A: Physical*, 87(3):139–145, 2001.
- [146] Xinghua Li, Takashi Abe, Yongxun Liu, and Masayoshi Esashi. Fabrication of high-density electrical feed-throughs by deep-reactive-ion etching of pyrex glass. *Journal of Microelectromechanical Systems*, 11(6):625–630, 2002.
- [147] T. Akashi and Y. Yoshimura. Deep reactive ion etching of borosilicate glass using an anodically bonded silicon wafer as an etching mask. *Journal of Micromechanics and Microengineering*, 16(5):1051, 2006.
- [148] Ciprian Iliescu, Kwong Luck Tan, Francis E. H. Tay, and Jianmin Miao. Deep wet and dry etching of pyrex glass: A review. In *Proceedings of the ICMAT (Symposium F), Singapore*, pages 75–78, 2005.
- [149] Haixin Zhu, Mark Holl, Tathagata Ray, Shivani Bhushan, and Deirdre R Meldrum. Characterization of deep wet etching of fused silica glass for single cell and optical sensor deposition.

- Journal of Micromechanics and Microengineering*, 19(6):065013, 2009.
- [150] Ciprian Iliescu, Ji Jing, Francis E. H. Tay, Jianmin Miao, and Tietun Sun. Characterization of masking layers for deep wet etching of glass in an improved HF/HCl solution. *Surface and Coatings Technology*, 198(1-3):314–318, 2005.
- [151] Y. Mourzina, A. Steffen, and A. Offenhäusser. The evaporated metal masks for chemical glass etching for biomems. *Microsystem technologies*, 11(2-3):135–140, 2005.
- [152] K. M. Knowles and ATJ Van Helvoort. Anodic bonding. *International Materials Reviews*, 51(5):273–311, 2006.
- [153] Samuel Marre, Andrea Adamo, Soubir Basak, Cyril Aymonier, and Klavs F Jensen. Design and packaging of microreactors for high pressure and high temperature applications. *Industrial and engineering chemistry research*, 49(22):11310–11320, 2010.
- [154] Xiang Cheng, Matthew D. Ooms, and David Sinton. Biomass-to-biocrude on a chip via hydrothermal liquefaction of algae. *Lab on a Chip*, 16(2):256–260, 2016.
- [155] Klavs F. Jensen. Silicon-based microchemical systems: characteristics and applications. *MRS bulletin*, 31(2):101–107, 2006.
- [156] S. C. Kelley, G. A. Deluga, and William H. Smyrl. Miniature fuel cells fabricated on silicon substrates. *AIChE Journal*, 48(5):1071–1082, 2002.
- [157] Arturo A. Ayón, R. Braff, Chuang-Chia Lin, Herb H. Sawin, and Martin A. Schmidt. Characterization of a time multiplexed inductively coupled plasma etcher. *Journal of the electrochemical Society*, 146(1):339, 1999.
- [158] Marc J. Madou. *Fundamentals of microfabrication: the science of miniaturization*. CRC press, 2018.
- [159] Fernando Benito-Lopez, Willem Verboom, Masaya Kakuta, J. Han G. E. Gardeniers, Richard J. M. Egberink, Edwin R. Oosterbroek, Albert van den Berg, and David N. Reinhoudt. Optical fiber-based on-line uv/vis spectroscopic monitoring of chemical reaction kinetics under high pressure in a capillary microreactor. *Chemical communications*, (22):2857–2859, 2005.
- [160] Samuel Marre, Jinyoung Baek, Jongnam Park, Mounji G. Bawendi, and Klavs F. Jensen. High-pressure/high-temperature microreactors for nanostructure synthesis. *JALA: Journal of the Association for Laboratory Automation*, 14(6):367–373, 2009.
- [161] Evgeniy S. Ilin, Samuel Marre, Véronique Jubera, and Cyril Aymonier. Continuous supercritical synthesis of high quality uv-emitting ZnO nanocrystals for optochemical applications. *Journal of Materials Chemistry C*, 1(33):5058–5063, 2013.

- [162] Ting-Fu Hong, Wei-Jhong Ju, Ming-Chang Wu, Chang-Hsien Tai, Chien-Hsiung Tsai, and Lung-Ming Fu. Rapid prototyping of pmma microfluidic chips utilizing a CO₂ laser. *Microfluidics and nanofluidics*, 9(6):1125–1133, 2010.
- [163] Ji-Yen Cheng, Cheng-Wey Wei, Kai-Hsiung Hsu, and Tai-Horng Young. Direct-write laser micromachining and universal surface modification of pmma for device development. *Sensors and Actuators B: Chemical*, 99(1):186–196, 2004.
- [164] Wurong Ren, Jayakumar Perumal, Jun Wang, Hao Wang, Siddharth Sharma, and Dong-Pyo Kim. Whole ceramic-like microreactors from inorganic polymers for high temperature or/and high pressure chemical syntheses. *Lab on a Chip*, 14(4):779–786, 2014.
- [165] Alexandre Martin, Sébastien Teychené, Séverine Camy, and Joëlle Aubin. Fast and inexpensive method for the fabrication of transparent pressure-resistant microfluidic chips. *Microfluidics and Nanofluidics*, 20(6):92, 2016.
- [166] Carl K. Fredrickson and Z. Hugh Fan. Macro-to-micro interfaces for microfluidic devices. *Lab on a Chip*, 4(6):526–533, 2004.
- [167] Ashish V. Pattekar and Mayuresh V. Kothare. Novel microfluidic interconnectors for high temperature and pressure applications. *Journal of Micromechanics and Microengineering*, 13(2):337, 2003.
- [168] S. Mukherjee, M. K. Hatalis, and M. V. Kothare. Water gas shift reaction in a glass microreactor. *Catalysis today*, 120(1):107–120, 2007.
- [169] Edward R. Murphy, Tomoya Inoue, Hemantkumar R. Sahoo, Nikolay Zaborenko, and Klavs F. Jensen. Solder-based chip-to-tube and chip-to-chip packaging for microfluidic devices. *Lab on a Chip*, 7(10):1309–1314, 2007.
- [170] Franz Trachsel, Cedric Hutter, and Philipp Rudolf von Rohr. Transparent silicon/glass microreactor for high-pressure and high-temperature reactions. *Chemical Engineering Journal*, 135:S309–S316, 2008.
- [171] Yoav Peles, V. T. Srikar, Todd S. Harrison, Christopher Protz, Anna Mracek, and S. Mark Spearing. Fluidic packaging of microengine and microrocket devices for high-pressure and high-temperature operation. *Journal of Microelectromechanical systems*, 13(1):31–40, 2004.
- [172] Brian K.H. Yen, Axel Günther, Martin A. Schmidt, Klavs F. Jensen, and Mounqi G. Bawendi. A microfabricated gas–liquid segmented flow reactor for high-temperature synthesis: the case of CdSe quantum dots. *Angewandte Chemie*, 117(34):5583–5587, 2005.
- [173] M. T. Blom, E. Chmela, Johannes G. E. Gardeniers, Johan W. Berenschot, M. Elwenspoek,

- R. Tijssen, and Albert van den Berg. Local anodic bonding of kovar to pyrex aimed at high-pressure, solvent-resistant microfluidic connections. *Journal of Micromechanics and Microengineering*, 11(4):382, 2001.
- [174] Samuel Marre, Jongnam Park, Jane Rempel, Juan Guan, Mounji G. Bawendi, and Klavs F. Jensen. Supercritical continuous-microflow synthesis of narrow size distribution quantum dots. *Advanced Materials*, 20(24):4830–4834, 2008.
- [175] Milad Abolhasani, Mayank Singh, Eugenia Kumacheva, and Axel Günther. Automated microfluidic platform for studies of carbon dioxide dissolution and solubility in physical solvents. *Lab on a Chip*, 12(9):1611–1618, 2012.
- [176] For more detailed O-ring specifications and groove design please see. *MARCO rubber & plastic*. <http://www.marcorubber.com/orings.htm>., 2020.
- [177] M. Leester-Schädel, T. Lorenz, F. Jürgens, and C. Richter. Fabrication of microfluidic devices. In *Microsystems for Pharmatechnology*, pages 23–57. Springer, 2016.
- [178] Frédéric Marty, Lionel Rousseau, Bassam Saadany, Bruno Mercier, Olivier Français, Yoshio Mita, and Tarik Bourouina. Advanced etching of silicon based on deep reactive ion etching for silicon high aspect ratio microstructures and three-dimensional micro- and nanostructures. *Microelectronics journal*, 36(7):673–677, 2005.
- [179] Ted L. Anderson. *Fracture mechanics: fundamentals and applications*. CRC press, 2017.
- [180] J. Rabier and J. L. Demenet. Low temperature, high stress plastic deformation of semiconductors: the silicon case. *Physica Status Solidi B Basic Solid State Physics*, 222(1):63–74, 2000.
- [181] Michael D. Abràmoff, Paulo J Magalhães, and Sunanda J. Ram. Image processing with ImageJ. *Biophotonics international*, 11(7):36–42, 2004.
- [182] S. Bachu and J. J. Adams. Sequestration of CO₂ in geological media in response to climate change: capacity of deep saline aquifers to sequester CO₂ in solution. *Energy Conversion and Management*, 44(20):3151–3175, 2003.
- [183] Jerome A. Neufeld, Marc A. Hesse, Amir Riaz, Mark A. Hallworth, Hamdi A. Tchelepi, and Herbert E Huppert. Convective dissolution of carbon dioxide in saline aquifers. *Geophysical Research Letters*, 37(22):22, 2010.
- [184] Eric J. Beckman. Supercritical and near-critical CO₂ in green chemical synthesis and processing. *Journal of Supercritical Fluids*, 28:121–191, 2004.
- [185] Y. T. Shah, B. Godbole Kelkar, S. P. Godbole, and W.-D. Deckwer. Design parameters

- estimations for bubble column reactors. *AIChE Journal*, 28(3):353–379, 1982.
- [186] Nigar Kantarci, Fahir Borak, and Kutlu O Ulgen. Bubble column reactors. *Process Biochemistry*, 40(7):2263–2283, 2005.
- [187] Klaas Van’t Riet. Review of measuring methods and results in nonviscous gas-liquid mass transfer in stirred vessels. *Industrial & Engineering Chemistry Process Design and Development*, 18(3):357–364, 1979.
- [188] Peter M Wilkinson, Herman Haringa, and Laurent L. Van Dierendonck. Mass transfer and bubble size in a bubble column under pressure. *Chemical Engineering Science*, 49(9):1417–1427, 1994.
- [189] Claus Fleischer, Stefan Becker, and Gerhart Eigenberger. Detailed modeling of the chemisorption of CO₂ into NaOH in a bubble column. *Chemical Engineering Science*, 51(10), 1996.
- [190] G. Vázquez, M. A. Cancela, R. Varela, E. Alvarez, and J. M. Navaza. Influence of surfactants on absorption of CO₂ in a stirred tank with and without bubbling. *Chemical Engineering Journal*, 67(2):131–137, 1997.
- [191] J. De Jong, Rob G. H. Lammertink, and Matthias Wessling. Membranes and microfluidics: a review. *Lab on a Chip*, 6(9):1125–1139, 2006.
- [192] Grégoire Bongrand and Peichun Amy Tsai. Manipulation of viscous fingering in a radially tapered cell geometry. *Physical Review E*, 97(6):061101, 2018.
- [193] Marzieh Saadat, Peichun A Tsai, Tsai-Hsing Ho, Gisle Øye, and Marcin Dudek. Development of a microfluidic method to study enhanced oil recovery by low salinity water flooding. *ACS omega*, 5(28):17521–17530, 2020.
- [194] Jun Yue, Lingai Luo, Yves Gonthier, Guangwen Chen, and Quan Yuan. An experimental study of air–water Taylor flow and mass transfer inside square microchannels. *Chemical Engineering Science*, 64(16):3697–3708, 2009.
- [195] Jian Ren, Songbo He, Chunbo Ye, Guangwen Chen, and Chenglin Sun. The ozone mass transfer characteristics and ozonation of pentachlorophenol in a novel microchannel reactor. *Chemical Engineering Journal*, 210:374–384, 2012.
- [196] Stephanie G. R. Lefortier, Peter J. Hamersma, Andre Bardow, and Michiel T. Kreutzer. Rapid microfluidic screening of CO₂ solubility and diffusion in pure and mixed solvents. *Lab on a Chip*, 12(18):3387–3391, 2012.
- [197] Karsten Michael, Alexandra Golab, Valeriya Shulakova, Jonathan Ennis-King, Guy Allinson, Sandeep Sharma, and Toby Aiken. Geological storage of CO₂ in saline aquifers—a review

- of the experience from existing storage operations. *International Journal of Greenhouse Gas Control*, 4(4):659–667, 2010.
- [198] Phong Nguyen, Danyal Mohaddes, Jason Riordon, Hossein Fadaei, Pushan Lele, and David Sinton. Fast fluorescence-based microfluidic method for measuring minimum miscibility pressure of CO₂ in crude oils. *Analytical chemistry*, 87(6):3160–3164, 2015.
- [199] Atena Sharbatian, Ali Abedini, ZhenBang Qi, and David Sinton. Full characterization of CO₂–oil properties on-chip: solubility, diffusivity, extraction pressure, miscibility, and contact angle. *Analytical Chemistry*, 90(4):2461–2467, 2018.
- [200] Bruno Pinho, Stéphane Girardon, Frédéric Bazer-Bachi, Ghislain Bergeot, Samuel Marre, and Cyril Aymonier. Simultaneous measurement of fluids density and viscosity using HP/HT capillary devices. *Journal of Supercritical Fluids*, 105:186–192, 2015.
- [201] Bruno Pinho, Stéphane Girardon, Frédéric Bazer-Bachi, Ghislain Bergeot, Samuel Marre, and Cyril Aymonier. A microfluidic approach for investigating multicomponent system thermodynamics at high pressures and temperatures. *Lab on a Chip*, 14(19):3843–3849, 2014.
- [202] Bo Bao, Jason Riordon, Yi Xu, Huawei Li, and David Sinton. Direct measurement of the fluid phase diagram. *Analytical chemistry*, 88(14):6986–6989, 2016.
- [203] Chaoqun Yao, Kai Zhu, Yanyan Liu, Hongchen Liu, Fengjun Jiao, and Guangwen Chen. Intensified CO₂ absorption in a microchannel reactor under elevated pressures. *Chemical Engineering Journal*, 319:179–190, 2017.
- [204] Ning Qin, John Z. Wen, and Carolyn L. Ren. Highly pressurized partially miscible liquid-liquid flow in a micro-t-junction. i. experimental observations. *Physical Review E*, 95(4):043110, 2017.
- [205] Sami Franssila. *Introduction to microfabrication*. John Wiley & Sons, 2010.
- [206] Tsai-Hsing Martin Ho and Peichun Amy Tsai. Microfluidic salt precipitation: implications for geological CO₂ storage. *Lab on a Chip*, 20(20):3806–3814, 2020.
- [207] National Institute of Standards and U.S. Department of Commerce Technology. *NIST Standard Reference Database Number 69*. <https://webbook.nist.gov/chemistry/>, 2020.
- [208] Alain Valtz, Antonin Chapoy, Christophe Coquelet, Patrice Paricaud, and Dominique Richon. Vapour–liquid equilibria in the carbon dioxide–water system, measurement and modelling from 278.2 to 318.2 K. *Fluid Phase Equilibria*, 226:333–344, 2004.
- [209] Takashi Nakayama, Hiroshi Sagara, Kunio Arai, and Shozaburo Saito. High pressure liquid/liquid equilibria for the system of water, ethanol and 1, 1-difluoroethane at 323.2 K. *Fluid Phase Equilibria*, 38(1-2):109–127, 1987.

- [210] A. Tamimi, Edward B. Rinker, and Orville C Sandall. Diffusion coefficients for hydrogen sulfide, carbon dioxide, and nitrous oxide in water over the temperature range 293-368 K. *Journal of Chemical and Engineering Data*, 39(2):330–332, 1994.
- [211] Bernd Jähne, Gerhard Heinz, and Wolfgang Dietrich. Measurement of the diffusion coefficients of sparingly soluble gases in water. *Journal of Geophysical Research: Oceans.*, 92(C10):10767–10776, 1987.
- [212] Shane P. Cadogan, Geoffrey C. Maitland, and J. P. Martin Trusler. Diffusion coefficients of CO₂ and N₂ in water at temperatures between 298.15 K and 423.15 K at pressures up to 45 MPa. *Journal of Chemical and Engineering Data*, 59(2):519–525, 2014.
- [213] J Wambui Mutoru, Alana Leahy-Dios, and Abbas Firoozabadi. Modeling infinite dilution and fickian diffusion coefficients of carbon dioxide in water. *AlChE Journal*, 57(6):1617–1627, 2011.
- [214] Franklin M Orr et al. Carbon capture, utilization, and storage: an update. *SPE Journal*, 23(06):2–444, 2018.
- [215] Zhien Zhang, Shu-Yuan Pan, Hao Li, Jianchao Cai, Abdul Ghani Olabi, Edward John Anthony, and Vasilije Manovic. Recent advances in carbon dioxide utilization. *Renewable and Sustainable Energy Reviews*, 125:109799, 2020.
- [216] Tabbi Wilberforce, Ahmad Baroutaji, Bassel Soudan, Abdul Hai Al-Alami, and Abdul Ghani Olabi. Outlook of carbon capture technology and challenges. *Science of the Total Environment*, 657:56–72, 2019.
- [217] Ahmad Al Adasani and Baojun Bai. Analysis of EOR projects and updated screening criteria. *Journal of Petroleum Science and Engineering*, 79(1-2):10–24, 2011.
- [218] V Prabu and Nirmal Mallick. Coalbed methane with CO₂ sequestration: An emerging clean coal technology in india. *Renewable Sustainable Energy Review*, 50:229–244, 2015.
- [219] Manab Mukherjee and Santanu Misra. A review of experimental research on enhanced coal bed methane (ECBM) recovery via CO₂ sequestration. *Earth-Science Reviews*, 179:392–410, 2018.
- [220] Nicolas Meunier, Remi Chauvy, Seloua Mouhoubi, Diane Thomas, and Guy De Weireld. Alternative production of methanol from industrial CO₂. *Renewable energy*, 146:1192–1203, 2020.
- [221] Joaquim B Branco, Pedro E Brito, and Ana C Ferreira. Methanation of CO₂ over nickel-lanthanide bimetallic oxides supported on silica. *Chemical Engineering Journal*, 380:122465, 2020.

- [222] A. G. Carroll, R. Przeslawski, L. C. Radke, J. R. Black, K. Picard, J. W. Moreau, R. R. Haese, and S. Nichol. Environmental considerations for subseabed geological storage of CO₂: A review. *Continental Shelf Research*, 83:116–128, 2014.
- [223] Yihua Teng and Dongxiao Zhang. Long-term viability of carbon sequestration in deep-sea sediments. *Science Advances*, 4(7):eaao6588, 2018.
- [224] Stefan Bachu. Review of CO₂ storage efficiency in deep saline aquifers. *International Journal of Greenhouse Gas Control*, 40:188–202, 2015.
- [225] Herbert E. Huppert and Jerome A. Neufeld. The fluid mechanics of carbon dioxide sequestration. *Annual Review of Fluid Mechanics*, 46:255–272, 2014.
- [226] Harpreet Singh. Impact of four different CO₂ injection schemes on extent of reservoir pressure and saturation. *Advanced Geo-Energy Research*, 2(3):305–318, 2018.
- [227] Jerry Blackford, Henrik Stahl, Jonathan M Bull, Benoît JP Bergès, Melis Cevatoglu, Anna Lichtschlag, Douglas Connelly, Rachael H James, Jun Kita, Dave Long, et al. Detection and impacts of leakage from sub-seafloor deep geological carbon dioxide storage. *Nature Climate Change*, 4(11):1011–1016, 2014.
- [228] Peter G. Brewer, Gernot Friederich, Edward T. Peltzer, and Franklin M. Orr. Direct experiments on the ocean disposal of fossil fuel CO₂. *Science*, 284(5416):943–945, 1999.
- [229] Peter G. Brewer, Edward T. Peltzer, Gernot Friederich, and Gregor Rehder. Experimental determination of the fate of rising CO₂ droplets in seawater. *Environmental Science & Technology*, 36(24):5441–5446, 2002.
- [230] Nazmi Sellami, Marius Dewar, Henrik Stahl, and Baixin Chen. Dynamics of rising CO₂ bubble plumes in the qics field experiment: Part 1—the experiment. *International Journal of Greenhouse Gas Control*, 38:44–51, 2015.
- [231] H. Teng and A. Yamasaki. Dissolution of buoyant CO₂ drops in a counterflow water tunnel simulating the deep ocean waters. *Energy Conversion and Management*, 41(9):929–937, 2000.
- [232] Keiichi Ogasawara, Akihiro Yamasaki, and Ho Teng. Mass transfer from CO₂ drops traveling in high-pressure and low-temperature water. *Energy Fuels*, 15(1):147–150, 2001.
- [233] Samah Maalej, Belkacem Benadda, and Michel Otterbein. Influence of pressure on the hydrodynamics and mass transfer parameters of an agitated bubble reactor. *Chemical Engineering and Technology*, 24(1):77–84, 2001.
- [234] Shelley Lynn Anna. Droplets and bubbles in microfluidic devices. *Annual Review of Fluid Mechanics*, 48:285–309, 2016.

- [235] Esther Amstad, Xiaoming Chen, Max Eggersdorfer, Noa Cohen, Thomas E Kodger, Carolyn L Ren, and David A Weitz. Parallelization of microfluidic flow-focusing devices. *Physical Review E*, 95(4):043105, 2017.
- [236] Pingan Zhu, Tiantian Kong, Leyan Lei, Xiaowei Tian, Zhanxiao Kang, and Liqui Wang. Droplet breakup in expansion-contraction microchannels. *Scientific Reports*, 6(1):1–11, 2016.
- [237] Benoit Laborie, Florence Rouyer, DE Angelescu, and Elise Lorenceau. On the stability of the production of bubbles in yield-stress fluid using flow-focusing and t-junction devices. *Physics of Fluids*, 28(6):063103, 2016.
- [238] Maximilian L Eggersdorfer, Hansjörg Seybold, Alessandro Ofner, David A Weitz, and André R Studart. Wetting controls of droplet formation in step emulsification. *Proceedings of the National Academy of Sciences of the United States of America*, 115(38):9479–9484, 2018.
- [239] I Chakraborty, J Ricouvier, P Yazhgur, P Tabeling, and AM Leshansky. Droplet generation at hele-shaw microfluidic t-junction. *Physics of Fluids*, 31(2):022010, 2019.
- [240] Alinaghi Salari, Jiang Xu, Michael C Kolios, and Scott SH Tsai. Expansion-mediated breakup of bubbles and droplets in microfluidics. *Physical Review Fluids*, 5(1):013602, 2020.
- [241] Wen Yuan Fan, Shuai Chao Li, Li Xiang Li, Xi Zhang, Meng Qi Du, and Xiao Hong Yin. Hydrodynamics of gas/shear-thinning liquid two-phase flow in a co-flow mini-channel: Flow pattern and bubble length. *Physics of Fluids*, 32(9):092004, 2020.
- [242] H. Y. Wu and P. Cheng. Condensation flow patterns in silicon microchannels. *International Journal of Heat and Mass Transfer*, 48(11):2186–2197, 2005.
- [243] Yongping Chen, Chaoqun Shen, Mingheng Shi, and George P. Peterson. Visualization study of flow condensation in hydrophobic microchannels. *AIChE Journal*, 60(3):1182–1192, 2014.
- [244] John W. Coleman and Srinivas Garimella. Two-phase flow regimes in round, square and rectangular tubes during condensation of refrigerant R134a. *International Journal of Refrigeration*, 26(1):117–128, 2003.
- [245] Ali H. Al-Zaidi, Mohamed M. Mahmoud, and Tassos G. Karayiannis. Condensation flow patterns and heat transfer in horizontal microchannels. *Experimental Thermal and Fluid Science*, 90:153–173, 2018.
- [246] Luís MC Pereira, Antonin Chapoy, Rod Burgass, Mariana B Oliveira, João AP Coutinho, and Bahman Tohidi. Study of the impact of high temperatures and pressures on the equilibrium densities and interfacial tension of the carbon dioxide/water system. *Journal of Chemical Thermodynamics*, 93:404–415, 2016.

- [247] Larry W. Diamond and Nikolay N. Akinfiev. Solubility of CO₂ in water from -1.5 to 100 °C and from 0.1 to 100 MPa: evaluation of literature data and thermodynamic modelling. *Fluid Phase Equilibria*, 208(1-2):265–290, 2003.
- [248] Thomas Cubaud and Thomas G. Mason. Capillary threads and viscous droplets in square microchannels. *Physics of Fluids*, 20(5):053302, 2008.
- [249] Andrew S. Utada, Alberto Fernandez-Nieves, Jose M. Gordillo, and David A. Weitz. Absolute instability of a liquid jet in a coflowing stream. *Physical Review Letters*, 100(1):014502, 2008.
- [250] Pijush K. Kundu, Ira M. Cohen, and David R. Dowling. *Fluid Mechanics, 5th ed.* London: Academic, 2011.
- [251] Adrian Bejan. *Advanced Engineering Thermodynamics*. John Wiley & Sons, 2016.
- [252] William Kloek, Ton Van Vliet, and Marcel Meinders. Effect of bulk and interfacial rheological properties on bubble dissolution. *J. Colloid Interface Sci.*, 237(2):158–166, 2001.
- [253] P Brent Duncan and David Needham. Test of the epstein- plesset model for gas microparticle dissolution in aqueous media: effect of surface tension and gas undersaturation in solution. *Langmuir*, 20(7):2567–2578, 2004.
- [254] Peng Zhang, Chaoqun Yao, Haiyun Ma, Nan Jin, Xunli Zhang, Hongying Lü, and Yuchao Zhao. Dynamic changes in gas-liquid mass transfer during taylor flow in long serpentine square microchannels. *Chemical Engineering Science*, 182:17–27, 2018.
- [255] Chaoqun Yao, Yuchao Zhao, Jia Zheng, Qi Zhang, and Guangwen Chen. The effect of liquid viscosity and modeling of mass transfer in gas-liquid slug flow in a rectangular microchannel. *AIChE Journal*, 66(5):e16934, 2020.
- [256] Soren Anderson and Richard Newell. Prospects for carbon capture and storage technologies. *Annual Review of Environment and Resources*, 29:109–142, 2004.
- [257] Dennis Y. C. Leung, Giorgio Caramanna, and M. Mercedes Maroto-Valer. An overview of current status of carbon dioxide capture and storage technologies. *Renewable Sustainable Energy Reviews*, 39:426–443, 2014.
- [258] S. Grude, M. Landrø, and J. Dvorkin. Pressure effects caused by CO₂ injection in the tubåen fm., the snøhvit field. *International Journal of Greenhouse Gas Control*, 27:178–187, 2014.
- [259] G. Baumann, J. Henniges, and M. De Lucia. Monitoring of saturation changes and salt precipitation during CO₂ injection using pulsed neutron-gamma logging at the ketzin pilot site. *International Journal of Greenhouse Gas Control*, 28:134–146, 2014.
- [260] Karsten Pruess and Nadja Müller. Formation dry-out from CO₂ injection into saline aquifers:

1. effects of solids precipitation and their mitigation. *Water Resources Research*, 45:3, 2009.
- [261] Kue-Young Kim, Weon Shik Han, Junho Oh, Taehee Kim, and Jeong-Chan Kim. Characteristics of salt-precipitation and the associated pressure build-up during CO₂ storage in saline aquifers. *Transport in Porous Media*, 92(2):397–418, 2012.
- [262] H. Ott, J. Snippe, K. De Kloe, H. Husain, and A. Abri. Salt precipitation due to sc-gas injection: single versus multi-porosity rocks. *Energy Procedia*, 37:3319–3330, 2013.
- [263] Laurent André, Yannick Peysson, and Mohamed Azaroual. Well injectivity during CO₂ storage operations in deep saline aquifers—part 2: Numerical simulations of drying, salt deposit mechanisms and role of capillary forces. *International Journal of Greenhouse Gas Control*, 22:301–312, 2014.
- [264] Ethan Guyant, Weon Shik Han, Kue-Young Kim, Myong-Ho Park, and Byoung-Yeop Kim. Salt precipitation and CO₂/brine flow distribution under different injection well completions. *International Journal of Greenhouse Gas Control*, 37:299–310, 2015.
- [265] Junho Oh, Kue-Young Kim, Weon Shik Han, Taehee Kim, Jeong-Chan Kim, and Eungyu Park. Experimental and numerical study on supercritical CO₂/brine transport in a fractured rock: Implications of mass transfer, capillary pressure and storage capacity. *Advances in Water Resources*, 62:442–453, 2013.
- [266] Yannick Peysson, Laurent André, and Mohamed Azaroual. Well injectivity during CO₂ storage operations in deep saline aquifers—part 1: Experimental investigation of drying effects, salt precipitation and capillary forces. *International Journal of Greenhouse Gas Control*, 22:291–300, 2014.
- [267] H. Ott, S. M. Roels, and K. De Kloe. Salt precipitation due to supercritical gas injection: I. capillary-driven flow in unimodal sandstone. *International Journal of Greenhouse Gas Control*, 43:247–255, 2015.
- [268] Javad Jeddizahed and Behzad Rostami. Experimental investigation of injectivity alteration due to salt precipitation during CO₂ sequestration in saline aquifers. *Advances in Water Resources*, 96:23–33, 2016.
- [269] Ruirui Zhao and Jianmei Cheng. Effects of temperature on salt precipitation due to formation dry-out during CO₂ injection in saline aquifers. *Greenhouse Gases: Science and Technology*, 7(4):624–636, 2017.
- [270] Changyong Zhang, Karl Dehoff, Nancy Hess, Mart Oostrom, Thomas W. Wietsma, Albert J. Valocchi, Bruce W. Fouke, and Charles J. Werth. Pore-scale study of transverse mixing induced

- CaCO₃ precipitation and permeability reduction in a model subsurface sedimentary system. *Environmental Science & Technology*, 44(20):7833–7838, 2010.
- [271] Peichun Tsai, Rob GH Lammertink, Matthias Wessling, and Detlef Lohse. Evaporation-triggered wetting transition for water droplets upon hydrophobic microstructures. *Physical Review Letters*, 104(11):116102, 2010.
- [272] Tiago Ferreira and Wayne Rasband. Imagej user guide. *ImageJ/Fiji*, 1:155–161, 2012.
- [273] Ekwere J. Peters. *Advanced Petrophysics: Volume 1: Geology, Porosity, Absolute Permeability, Heterogeneity and Geostatistics*. Live Oak Book Co, Austin, Texas, 2012.
- [274] David D. Weis and George E. Ewing. Water content and morphology of sodium chloride aerosol particles. *Journal of Geophysical Research: Atmospheres*, 104(D17):21275–21285, 1999.
- [275] Sara Sarig and Fania Tartakovsky. Crystal habit modifiers: Ii. the effect of supersaturation on dendritic growth. *Journal of Crystal Growth*, 28(3):300–305, 1975.
- [276] George V. Chilingar. Relationship between porosity, permeability, and grain-size distribution of sands and sandstones. In *Developments in Sedimentology*, volume 1, pages 71–75. Elsevier, 1964.
- [277] Roland Lenormand. Liquids in porous media. *Journal of Physics: Condensed Matter*, 2(S):SA79, 1990.
- [278] Pascale Aussillous and David Quéré. Quick deposition of a fluid on the wall of a tube. *Physics of Fluids*, 1. 2.(10):2367–2371, 2000.
- [279] Lu Yang, Maria Jose Nieves-Remacha, and Klavs F. Jensen. Simulations and analysis of multiphase transport and reaction in segmented flow microreactors. *Chemical Engineering Science*, 169:106–116, 2017.
- [280] R. Sh. Abiev, Colin Butler, Emmanuel Cid, Benjamin Lalande, and A-M Billet. Mass transfer characteristics and concentration field evolution for gas-liquid Taylor flow in milli channels. *Chemical Engineering Science*, 207:1331–1340, 2019.
- [281] Xiaoyan Ji, Sugata P. Tan, Hertanto Adidharma, and Maciej Radosz. Saft1-rpm approximation extended to phase equilibria and densities of CO₂-H₂O and CO₂-H₂O-NaCl systems. *Industrial & engineering chemistry research*, 44(22):8419–8427, 2005.
- [282] Thomas Giorgis, Michele Carpita, and Alfredo Battistelli. 2d modeling of salt precipitation during the injection of dry CO₂ in a depleted gas reservoir. *Energy Conversion and Management*, 48(6):1816–1826, 2007.
- [283] Suzanne Hurter, Johan Gerhard Berge, Diane Labregere, et al. Simulations for CO₂ injection

- projects with compositional simulator. In *SPE Offshore Europe Oil and Gas Conference and Exhibition*. Society of Petroleum Engineers, 2007.
- [284] Mehdi Zeidouni, Mehran Pooladi-Darvish, and David Keith. Analytical solution to evaluate salt precipitation during CO₂ injection in saline aquifers. *International Journal of Greenhouse Gas Control*, 3(5):600–611, 2009.
- [285] Stefan Bachu and D Brant Bennion. Interfacial tension between CO₂, freshwater, and brine in the range of pressure from (2 to 27) MPa, temperature from (20 to 125) °C, and water salinity from (0 to 334 000) mg·l⁻¹. *Journal of Chemical and Engineering Data*, 54(3):765–775, 2009.
- [286] Apostolos Georgiadis, Geoffrey Maitland, J. P. Martin Trusler, and Alexander Bismarck. Interfacial tension measurements of the (H₂O+CO₂) system at elevated pressures and temperatures. *Journal of Chemical and Engineering Data*, 55(10):4168–4175, 2010.
- [287] Mohammad Sarmadivaleh, Ahmed Z Al-Yaseri, and Stefan Iglauer. Influence of temperature and pressure on quartz–water–CO₂ contact angle and CO₂–water interfacial tension. *Journal of Colloid and Interface Science*, 441:59–64, 2015.
- [288] Sarmad Al-Anssari, Ahmed Barifcani, Alireza Keshavarz, and Stefan Iglauer. Impact of nanoparticles on the CO₂-brine interfacial tension at high pressure and temperature. *Journal of Colloid and Interface Science*, 532:136–142, 2018.
- [289] Simon Weides, Inga Moeck, Jacek Majorowicz, and Matthias Grobe. The cambrian basal sandstone unit in central alberta—an investigation of temperature distribution, petrography, and hydraulic and geomechanical properties of a deep saline aquifer. *Canadian Journal of Earth Sciences*, 51(8):783–796, 2014.
- [290] Dong Qin, Younan Xia, and George M Whitesides. Soft lithography for micro-and nanoscale patterning. *Nature Protocols*, 5(3):491, 2010.
- [291] Abhay Sharma. *Understanding color management*. John Wiley & Sons, 2018.

Appendix A

Additional data and analysis for "Microfluidic Mass Transfer of CO₂ at Different Phases"

A.1 EXPERIMENTAL DATA

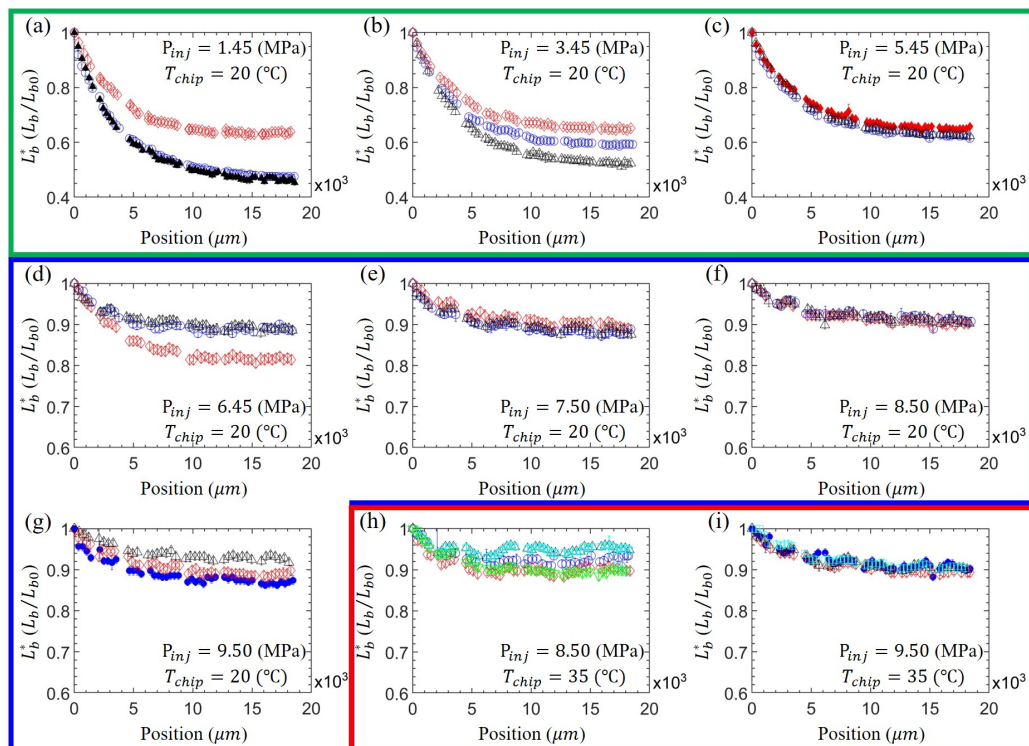


Figure A.1. The data demonstrate the dimensionless length change of CO₂ bubbles/droplets against the traveling distance for all of the experimental sets. Experiments for gas CO₂ are presented in (a)–(c), highlighted in the green rectangle. Size change in the liquid state is shown by (d)–(g), highlighted in the blue polygon. (h) and (i) are the cases working in the super-critical state, highlighted in the red rectangle. For CO₂ in gas and liquid states, three different sets of experiments were repeated (depicted by \circ , \diamond , and \triangle). For the super-critical CO₂, we ran five independent sets of experiments to confirm the reproducibility further (depicted by \circ , \diamond , \triangle , \square , and ∇). Solid symbols are the representative data shown in the paper.

A.2 MAXIMUM SIZE CHANGE

We correlated the dimensionless maximum size change of CO₂ (dL_{max}^*) with the CO₂ density, bubble velocity, and liquid volume measured from the experiments. The dL_{max}^* was determined using the mean value of the dL^* as a CO₂ bubble reaches its steady state. The results showed that the size change of CO₂ is primarily correlated with the CO₂ density. As the injection pressure, P_{inj} , is higher than 6.29 MPa, CO₂ phase changed to liquid and supercritical states. The CO₂ droplets become so condensed that mass transport during this short period does not significantly change the droplet size.

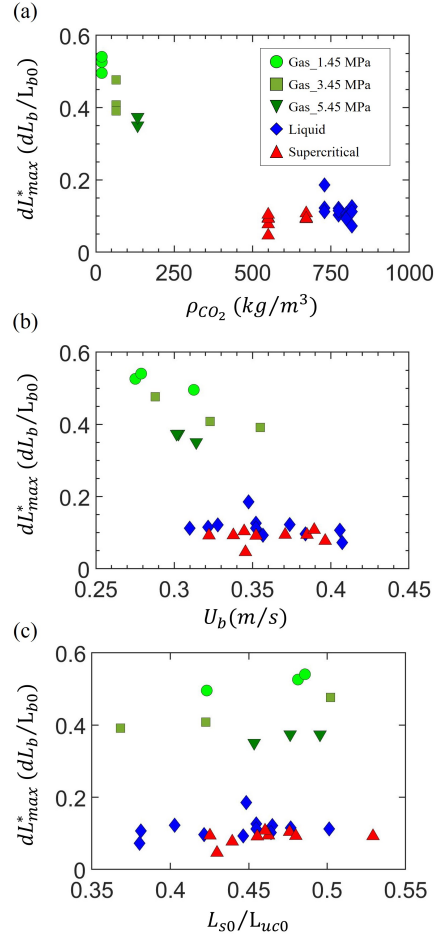


Figure A.2. (a) The dimensionless maximum bubble size change (dL_{max}^*) vs. CO₂ density; (b) dL_{max}^* vs. the mean bubble velocity (u_b); (c) dL_{max}^* versus the fraction of injection water. L_{s0} and L_{uc0} represent the initial length of the water slug and the unit cell, respectively. Here, the greater L_{s0}/L_{uc0} , the larger water volume is.

A.3 THERMODYNAMIC PROPERTIES

Table A.1

Thermodynamic properties of CO₂ used in the calculations

Injection Pressure	Temperature	CO ₂ Density	CO ₂ Viscosity	CO ₂ Phase State
P_{inj}	T_{chip}	$\rho_{CO_2}^*$	$\mu_{CO_2}^*$	n/a
(MPa)	(K)	(kg/m ³)	($\mu Pa \cdot s$)	n/a
0.25	297	4.68	14.89	Gas
1.45	297	28.19	15.04	Gas
3.45	297	77.22	15.61	Gas
5.45	297	156.48	17.27	Gas
6.45	297	737.48	60.76	Liquid
7.5	297	776.98	66.81	Liquid
8.5	297	800.81	70.83	Liquid
9.5	297	819.16	74.14	Liquid
8.5	308	617.59	46.45	Super Critical
9.5	308	693.95	55.23	Super Critical

* Data sourced from the NIST Chemistry Webbook [207].

Table A.2

Thermodynamic properties of water used in the calculations

Injection Pressure	Temperature	Water Density	Water Viscosity	Interfacial Tension (H ₂ O-CO ₂)
P_{inj}	T	$\rho_{H_2O}^*$	$\mu_{H_2O}^*$	σ^\dagger
(MPa)	(K)	(kg/m ³)	($\mu Pa \cdot s$)	(mN/m)
0.25	297	997.40	913.85	73.44
1.45	297	997.95	913.53	65.73
3.45	297	998.85	913.00	52.42
5.45	297	999.74	912.50	41.29
6.45	297	1000.2	912.26	36.00
7.5	297	1000.7	912.01	30.12
8.5	297	1001.1	911.78	30.28
9.5	297	1001.5	911.56	25.11
8.5	308	997.76	721.60	30.28
9.5	308	998.21	721.63	25.11

† Data averaged from previous measurements [285, 286, 287, 246, 288].

* Data sourced from the NIST Chemistry Webbook [207]

Table A.3

The resultant dimensionless parameters for calculating the film thickness

P	$Re_{\text{H}_2\text{O}}$	$Ca_{\text{H}_2\text{O}}$	We	CO ₂ Phase State
(MPa)	$\frac{\rho u_b d_c}{\mu}$	$\frac{\mu u_b}{\sigma}$	$\frac{\rho u_b^2 d_c}{\sigma}$	n/a
0.25	16.33	1.86×10^{-3}	0.01	Gas
1.45	33.14	4.22×10^{-3}	0.06	Gas
3.45	36.91	5.88×10^{-3}	0.10	Gas
5.45	34.79	7.02×10^{-3}	0.11	Gas
6.45	38.82	8.97×10^{-3}	0.16	Liquid
7.5	37.85	1.04×10^{-2}	0.18	Liquid
8.5	43.51	1.19×10^{-2}	0.24	Liquid
9.5	41.37	1.37×10^{-2}	0.26	Liquid
8.5	51.47	8.87×10^{-3}	0.21	Super Critical
9.5	51.46	1.07×10^{-2}	0.25	Super Critical

Appendix B

Detail analysis of phase change for
"Multiphase CO₂ Emulsions in
Microfluidics: Formation, Phases, and
Mass Transfer"

Detailed calculations of mass change of each phase due to phase change and dissolution

This appendix shows the case bubbly flow's detailed mass change calculations for supporting the discussions regarding Fig. 4.5. Each representative case demonstrated in Fig. 4.5 has gone through this type of analysis for determining the phase state of a CO₂ emulsion. For a CO₂ emulsion flowing in the microchannel, the total volume and mass is the sum of the inner (dyed) and outer phase, as seen in Fig. B.1a–c. Fig. B.1b and B.1c demonstrate the mass of a CO₂ emulsion varying with time based on the two different phase combinations, using presumption 1 and 2.

The total CO₂ volume and mass can be estimated from the contributions of the inner (dyed) and outer phases:

$$V_T(t) = V_{in}(t) + V_{out}(t), \quad (\text{B.1})$$

$$M_T(t) = \rho_{\text{CO}_2} V_{in}(t) + \rho_{\text{CO}_2} V_{out}(t). \quad (\text{B.2})$$

The mass change of each phase comes from two primary parts: due to the phase change and the dissolution in water (denoted by the subscript P and D , respectively):

$$M_{out}(t) - M_{out}(t_0) = m_{out}^D + m_{out}^P, \quad (\text{B.3})$$

$$M_{in}(t) - M_{in}(t_0) = m_{in}^D + m_{in}^P, \quad (\text{B.4})$$

where M_{out} (M_{in}) denotes the mass of the outer (dyed inner) phase. m^P represents the mass change due to the phase transition between the outer and inner phases; m^D is the mass loss due to its dissolution in water.

We consider the mass conservation during a phase change process and assume $m_{in}^P = -m_{out}^P$. The mass change of a CO₂ emulsion can be obtained by adding Eqn. (B.3) and Eqn. (B.4):

$$\Delta M_T(t) = M_T(t) - M_T(t_0) = m_{out}^D + m_{in}^D. \quad (\text{B.5})$$

Fig. B.1e–f present the results of $\Delta M_T(t)$ according to the two presumptions. Eqn. (B.5) implies that the mass of a CO₂ emulsion is always decreasing because CO₂ dissolves in water. Fig. B.1d shows the estimated CO₂ concentration in the adjacent water slug, $C(t)$, compared with the theoretical CO₂ solubility in the water (black dashed-line). $C(t)$ was calculated by dividing the absolute value of ΔM_T in (e) and (f) by the volume of adjacent water slug, V_{slug} .

We can further estimate m_{in}^P by subtracting Eqn. (B.4) from Eqn. (B.3):

$$m_{out}^D - m_{in}^D + 2m_{in}^P = \Delta M_{in}(t) - \Delta M_{out}(t). \quad (\text{B.6})$$

Here, we assume the dissolved CO_2 from both phases is comparable. Thus, the term $m_{out}^D - m_{in}^D$ is negligible compared to the $2m_{in}^P$ term. m_{in}^P can be expressed as half of the difference of $\Delta M_{in}(t)$ and $\Delta M_{out}(t)$:

$$m_{in}^P = \frac{1}{2} [\Delta M_{in}(t) - \Delta M_{out}(t)]. \quad (\text{B.7})$$

The results calculated from Eqn. (B.7) are shown in Fig. B.1g.

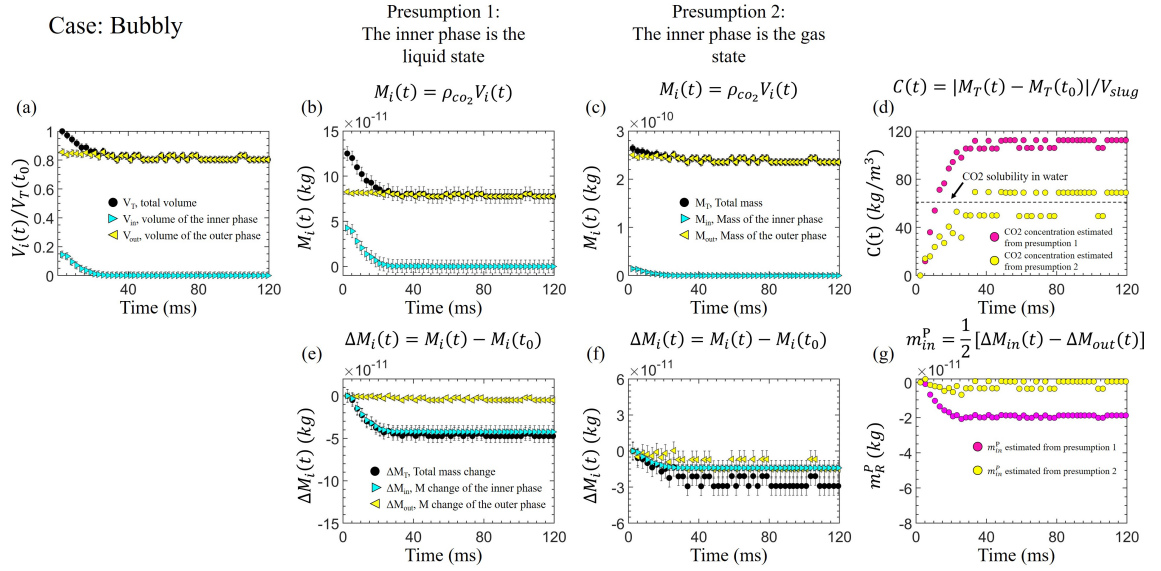


Figure B.1. The detailed calculations of a CO_2 emulsion based on the mean value from five emulsions in the case of the bubbly flow. (a) The volume fractions, $V_i(t)$, of the outer phase (V_{out}), the (dyed) inner phase (V_{in}), and the total volume ($V_T = V_{out} + V_{in}$) changing with time (t). (b) The mass of the outer phase, $M_{out} = \rho_{\text{CO}_2} V_{out}$, and the dyed, inner phase, $M_{in} = \rho_{\text{CO}_2} V_{in}$, changing with time based on Presumption 1 (assuming the inner phase is the liquid CO_2). The total mass of a CO_2 emulsion, $M_T = M_{out} + M_{in}$. (c) Results of M_{out} , M_{in} , and M_T calculated from Presumption 2 (assuming the outer phase is the liquid CO_2). (e) and (f) present the net mass change of an emulsion varying with time calculated according to presumption 1 and 2, respectively. ΔM represents the variation of mass from its initial value, $M(t_0)$. The data for the outer phase is denoted by \blacktriangleleft , while the dyed inner phase by \blacktriangleright ; \bullet represents the sum properties. (d) The estimated CO_2 concentration, $C(t)$, changes with time according to presumption 1 (\bullet) and 2 (\circ). The black dashed line denotes the theoretical CO_2 solubility in the water. (g) The estimated mass change of the dyed, inner phase resulted from the phase transition.

Appendix C

Reproducibility data and image analysis for "Microfluidic Salt Precipitation: Implications for Geological CO₂ Storage"

C.1 PATTERNS of MICROFLUIDIC POROUS MEDIA

Shown in Fig. C.1 are the two microfluidic network patterns used, primarily consisting of regular micro-pillars of a constant height arranged in a 2D ordered lattice. For the case of $\phi = 0.52$ in (a), cylindrical micro-pillars align in a body-centered packing of a pillar diameter of $d_1 (= 550 \mu\text{m})$. The closest distance between two pillars, $L_{p1} (= 500\sqrt{2} \mu\text{m})$. The right image in (a) shows the unit pore area used here, corresponding to the purple area of $A_{p1} = L_{p1}^2 - \pi d_1^2/4 = 2.62 \times 10^5 \mu\text{m}^2$. In (b), for $\phi = 0.23$ micro-pillars align in the form of a hexagonal packing, where the pillar diameter $d_2 = 460 \mu\text{m}$. The closest distance between the two pillars is $L_{p2} (= 500 \mu\text{m})$. The length scales of the pillar diameter and pore throat chosen align with those of Alberta Cambrian Basal Sandstone [289] (medium sand [82]). The unit pore area used for $\phi = 0.23$ is shown in the right image of (b), where is $A_{p2} = (\sqrt{3}L_{p2}^2/4 - \pi d_2^2/8) = 2.51 \times 10^4 \mu\text{m}^2$.

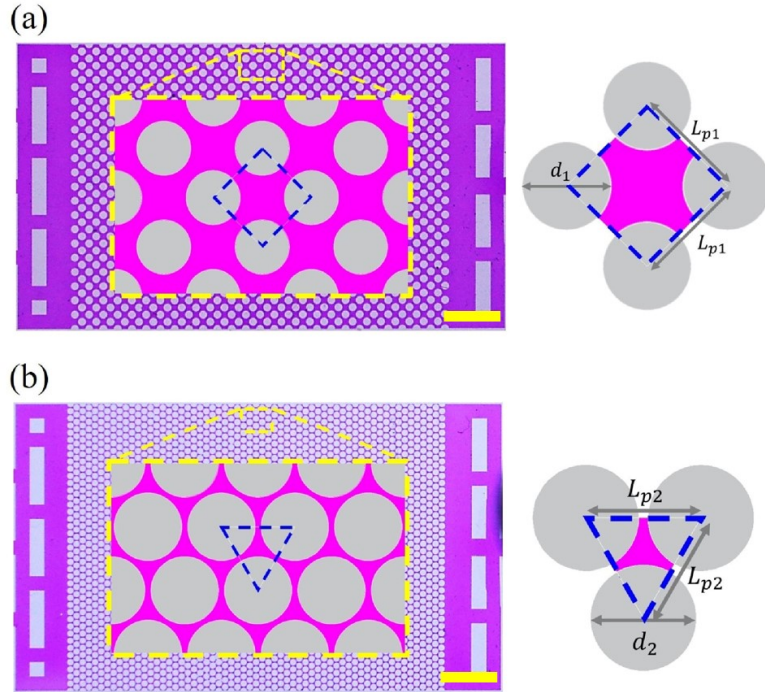


Figure C.1. The patterns of microfluidic porous structures and the schematic of the unit pore area used, for two different porosity (ϕ) values: (a) $\phi = 0.52$; (b) $\phi = 0.23$. The scale bar here presents 4 mm.

C.2 MICRO-FABRICATION PROCEDURES

C.2.1 PROCEDURE OF REPLICA MOLDING

Fig. C.2(b) shows the steps followed for replica molding. The silicon mold template (shown in Fig. C.2(c)) is first cleaned by DI water and ethanol. After applying the well-mixed PDMS (SYLGARD 184, Dow Corning, 10:1 ratio of silicone elastomer to a curing agent) onto the micro-structured wafers, the entire mold including un-cured PDMS is degassed in a vacuum chamber (for 45 minutes) to remove the bubbles in the PDMS. Subsequently, they were baked in an oven at 60°C for an hour to cure the PDMS [290]. After carefully de-molding the cured elastomer from the template, the micro-structured PDMS is bonded to a microscope glass slide by using a high-frequency plasma generator (Electro-Technic Inc., BD-20). The whole assembly is baked in an oven again at 60°C for an hour to bind the PDMS and the glass slide firmly. The final PDMS microfluidics is shown in Fig. C.2(d).

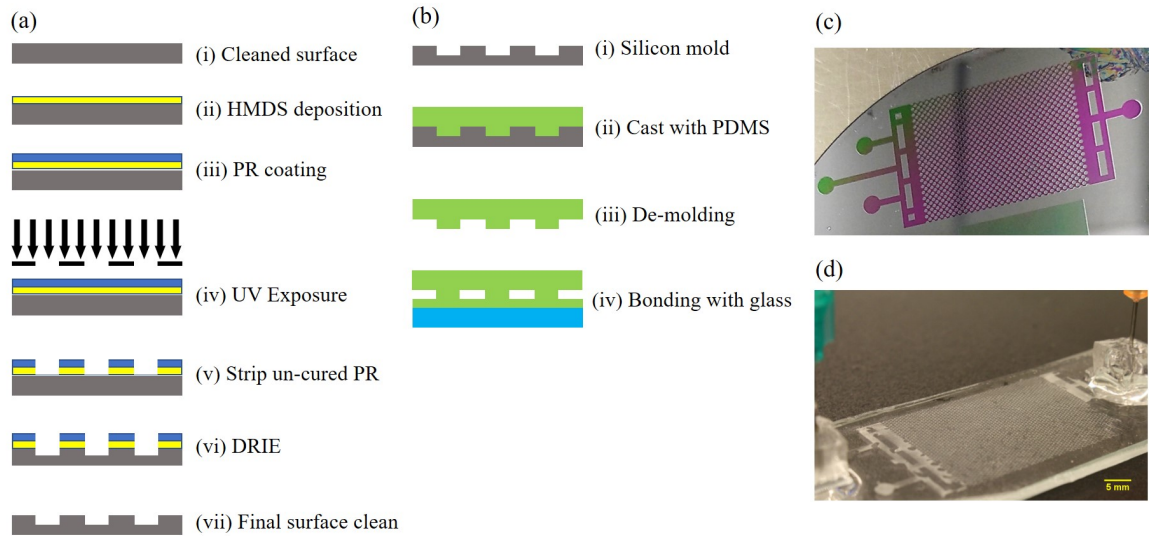


Figure C.2. (a) Process steps used for the micro-fabrication; (b) Replica molding steps using PDMS; (c) Photo of silicon template for the replica-molding method (before final cleaning); (d) A snapshot of the 2D porous PDMS microfluidics.

C.3 DETAILS OF IMAGE ANALYSIS

C.3.1 POST-IMAGE PROCESSES

Fig. C.3 is an example of isolating salt nucleation and the residual brine from the raw images to the binary images by thresholding in the CIELAB space. The CIELAB color space measures the brightness change of image from completely dark ($L^* = 0$) to white ($L^* = 100$) (The ImageJ-Fiji linearly expresses the maximum value of L^* to 255 for a RGB image [272]). The color channel a^* represents the components from green ($a^* = 0$) to color red ($a^* = 255$), and the b^* represents from color blue ($b^* = 0$) to yellow ($b^* = 255$) [291]. After several tests, we found that the color space range of $100 < L^* < 104$, $140 < a^* < 150$, and $b^* = 255$ can isolate the salt nucleation from the raw images, as shown in (a). To extract the signal of residual brine, the range of color space is tested to be $100 < L^* < 104$, $140 < a^* < 255$, and $b^* = 255$, as (b) represents. The color channel a^* represents the components from green ($a^* = 0$) to color red ($a^* = 255$), and the b^* represents from color blue ($b^* = 0$) to yellow ($b^* = 255$).

C.3.2 CALIBRATION

We checked and calibrated the processed images with the original raw images against the design parameters. As shown in Fig C.3 (c), the diameter of a pillar on the top image, D_r , is measured manually from the raw images. In each case, we manually measured the diameter of ten pillars from the raw images. The average value of D_r has about 2% of the relative error to the design value. The pillar diameter measured from the processed images (D_b) has an additional 1% of relative error on average. Consequently, the maximum accumulative error, resulting from the fabrication and post-image processes, is about 3% in our experiments. We further examine the measurement results of salt nucleation by overlapping the raw data with the binary images. Some salt deposits are not detected by the threshold steps, as shown in Fig. C.4. We manually crop these regions and measure the cover area of undetected salt. It is estimated to take about 1.53 % of total salt nucleation on average for the experiments with $\phi = 0.52$ porous patterns, while $\approx 3.12\%$ error of undetected salt on average for the $\phi = 0.23$ structure.

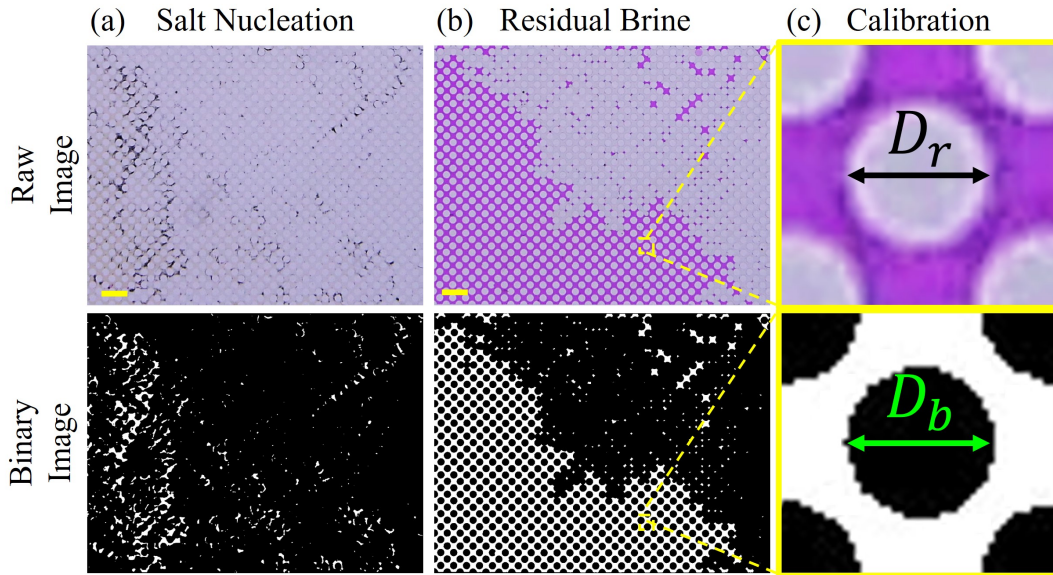


Figure C.3. Post image process for extracting the signals of salt crystals and residual brine from the raw images (represented by the first row of the images) for (a) Salt nucleation and (b) Residual brine. (c) shows a calibration of the raw and the binary images.

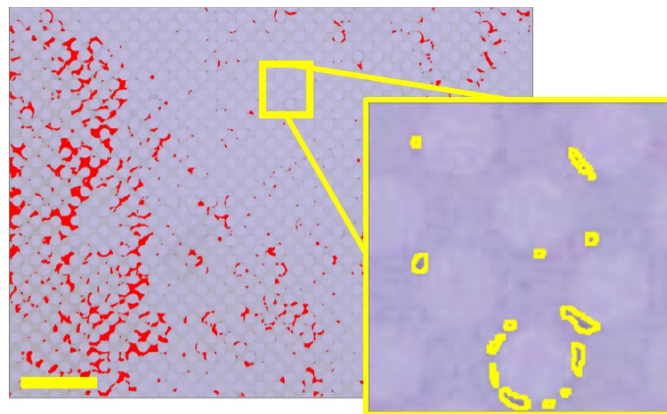


Figure C.4. The isolated salt nucleation (red area) and the undetected salt (spots cropped by yellow lines) after the threshold steps. The scale bar presents 4 mm.

C.4 EXPERIMENTAL DATA

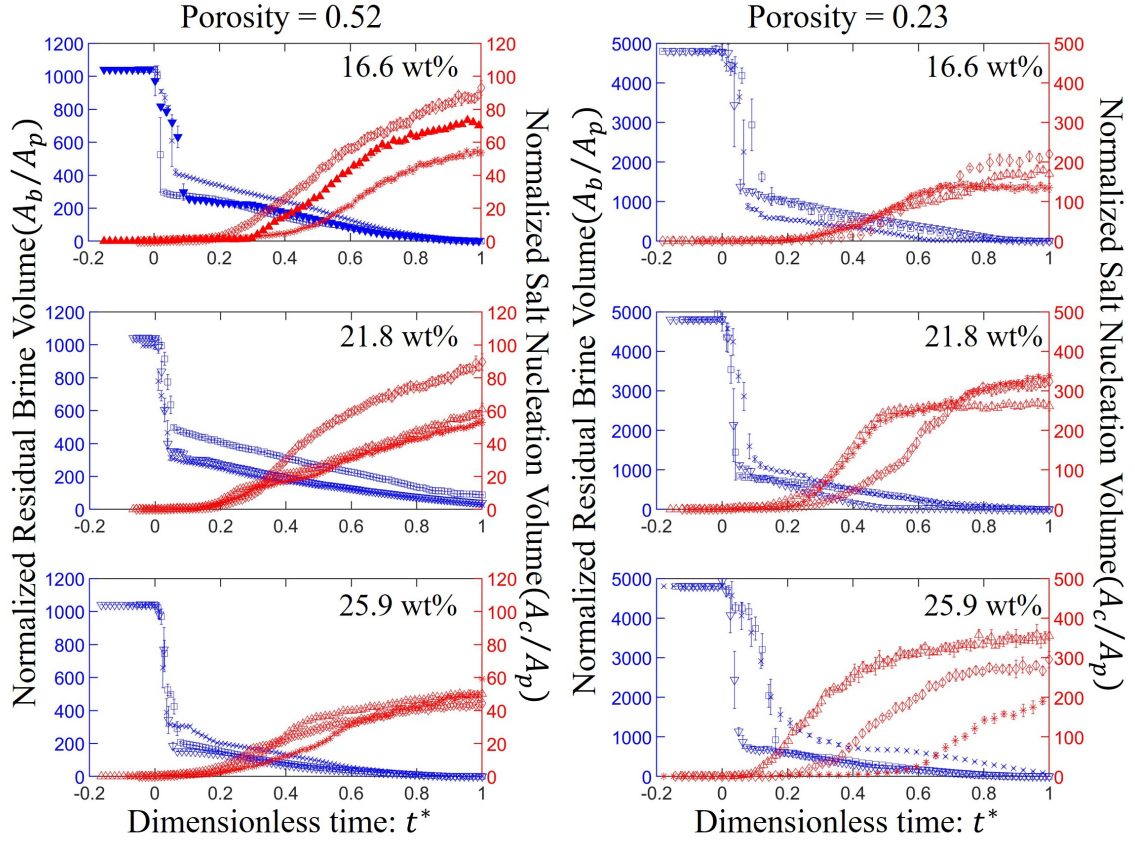


Figure C.5. The data summary of brine evaporation (shown by \square , ∇ , and \times) and salt growing (indicated by \diamond , \triangle , and \star) rates varying with dimensionless time in this experimental study. The two columns show the two different porosity cases, and the initial salt concentration increases from the first row (16.6 wt%) to the third row (25.9 wt%). The representative data for Fig. 2 (b) in the paper is highlighted by the solid triangles (\blacktriangledown and \blacktriangle) for $\phi = 0.52$ and 16.6 wt% salt-concentration.